Design and Analysis of Dual Rotor Motor for Electric Vehicle Application

Ankit Dalal

Design and Analysis of Dual Rotor Motor for Electric Vehicle Application

A

Thesis submitted

for the award of the degree of

Doctor of Philosophy

By

Ankit Dalal

Department of Electronics and Electrical Engineering

Indian Institute of Technology Guwahati

Guwahati - 781 039, Assam, India

November 2017

Dedicated to

My Beloved Parents

Certificate

This is to certify that the thesis entitled "**Design and Analysis of Dual Rotor Motor for Electric Vehicle Application**", submitted by **Ankit Dalal** (11610205), a research scholar in the *Department of Electronics and Electrical Engineering, Indian Institute of Technology Guwahati*, for the award of the degree of **Doctor of Philosophy**, is a record of an original research work carried out by him under my supervision and guidance. The thesis has fulfilled all requirements as per the regulations of the institute and in my opinion has reached the standard needed for submission. The results embodied in this thesis have not been submitted to any other University or Institute for the award of any degree or diploma.

Date:

Place: Guwahati.

Dr. Praveen Kumar
Associate Professor
Dept. of Electronics and Electrical Engg
Indian Institute of Technology Guwahati
Guwahati - 781 039, Assam, India.

Acknowledgements

First of all, I would like to thank my parents for all the love, support and belief they have given me over the course of my life. No words are enough to express their selfless love, affection and support. I feel it as a great privilege in expressing my deepest and most sincere gratitude to my supervisor Dr. Praveen Kumar, for his excellent guidance throughout my study. His kindness, dedication, hard work and attention to detail have been a great inspiration to me. My heartfelt thanks to you sir for the unlimited support and patience shown to me. I have no doubts that finishing my degree in a proper and timely manner was impossible without his helps, suggestions and advices.

I am also very thankful to my doctoral committee members Prof. Somanath Majhi, Dr. Praveen Tripathy and Dr. Sisir Kumar Nayak for sparing their precious time to evaluate the progress of my work and providing constructive criticism. I would also like to extend my gratitude to staff members of the department for providing all the necessary facility to carrying out this research work. I am thankful to Electrical Machines Lab, EEE Department, IIT Guwahati for providing all the necessary resources to complete my work specifically the dSPACE system for testing the DRM. I would like to extend my sincere thanks to all my beloved friends, past and present - too big to list here. You guys have been excellent and it would be difficult to find a working group as good as you. I would like to acknowledge the help extended by NFTDC, Hyderabad. I specially thank the director of NFTDC Dr. K. Bala Subramanian, Mr. Deepak Kulkarni sir and Mr. Ramaswamy sir for their support at every stage of DRM development. I thank DST, Govt. of India for funding the project on DRM.

I truly acknowledge the efforts made by co-author Sameer Nekkalapu during the implementation of the sub domain model of DRM presented in the third chapter of the thesis. I also acknowledge the help and guidance provided by co-author Mohammed Nasir Ansari to realize the work on electrical equivalent circuit of DRM, presented in the fourth chapter of the thesis.

Finally, I would like to thank all my beloved friends Saroj, Abhishek, Brajesh, Rakesh, Kashyap, Upendra, Gautam, Brijesh, Rajendra, Karam, Santosh, Sikandar, Umesh and Sushanta for their help, love, and support during my stay at IITG. I would like to specially acknowledge all the help extended by Ranjeet during my stay in Hyderabad. During the course of time, many people have supported

morally, financially, emotionally at different stages. It is difficult to remember and include name of all and therefore if I have missed anyone of you please forgive me as a true friend.

Ankit Dalal

Abstract

Increasing global warming and limited reserves of fossil fuels have created the need for alternatives to conventional internal combustion engines (ICE) based vehicles as primary mode of transport. In present time, Electric Vehicles (EV) are being seen as the solution for these problems. EVs integrated with renewable energy sources, completely eliminate dependence on fossil fuel as well as can drastically reduce emission of greenhouse gases. Therefore, a lot of attention is being given to the development of efficient, reliable and cost effective EVs by automobile industry as well as academic institutions.

Electric powertrain consisting of electric motor, drive system and battery as the main source of energy, is the most important part of an EV. Among all these parts, electric motor is responsible for driving the vehicle. Therefore, its rating, efficiency, control, cost etc. are very important factors from EV application viewpoint. Therefore, design and analysis of a motor suitable for EV application have been chosen as the aims for this thesis. Different types of motors can be used for EVs. EVs operating with induction motor, permanent magnet brushless DC motor and brushed DC motors have been manufactured by vehicle manufacturers. The thesis begins with a review of various type of motors used for EVs. A qualitative comparison of different motors has been presented. Subsequently, a need for a Dual Rotor Motor (DRM) having advantages of these motors and improving on their shortcomings is highlighted.

The second part of the thesis focuses on various possible configurations of DRM and describes the approach that has been adopted to finalize a configuration for further design and analysis.

The third part of the thesis deals with the analysis models developed for understanding of working principle and performance calculation of DRM. A 2-D analytical model using

subdomain model approach has been developed to calculate air-gap magnetic field as well as electromagnetic torque in the motor. For quick performance calculation of DRM steady state model comprising of electrical equivalent circuit and torque equation has been developed.

The final part of the thesis describes the design, prototyping and testing of DRM. Detailed electrical and mechanical design of DRM is presented. Pictures of different motor parts at different stages of manufacturing are given for practical visualization. The analysis models developed in the third part of the thesis have been validated with the experimental results in the testing of DRM section.

The prototype of DRM presented in the thesis is not an optimized one and power density and efficiency of the motor were not focused on. The presented motor is first prototype in the ongoing research work and thus considering the mechanical complexities and availability of resources, the scope of the practical work was limited to proof of concept of DRM and understanding of challenges involved. The lessons learnt during the process will be implemented during manufacturing of subsequent prototypes of DRM.

Contents

List of Figures

List of Tables

List of Acronyms

BEMF	Back Electromotive Force
DC	Direct Current
DRM	Dual Rotor Motor
EM	Electric Motor
EEC	Electrical Equivalent Circuit
EMI	Electromagnetic Interference
EP	Electrical Port
EV	Electric Vehicle
FEA	Finite Element Analysis
HEV	Hybrid Electric Vehicle
ICEV	Internal Combustion Engine Vehicle
IPM	Interior Permanent Magnet
IR	Inner Rotor
MP	Mechanical Port
OR	Outer Rotor
PM	Permanent Magnet
PMBLDC	Permanent Magnet Brushless DC
PMSM	Permanent Magnet Synchronous Motor
SPWM	Sine Pulse Width Modulation
SC	Squirrel Cage
SEV	Steam Engine Vehicle

SRM Switched Reluctance Motor

SSM Steady State Model

List of Symbols

M_{xs_yr}	Mutual inductance between *x*-phase of stator and *y*-phase of rotor.
M_{xr_ys}	Mutual inductance between *x*-phase of rotor and *y*-phase of stator.
M_{xs_ys}	Mutual inductance between *x*-phase of stator and *y*-phase of stator.
M_{xr_yr}	Mutual inductance between *x*-phase of rotor and *y*-phase of rotor.
M_{max_sr}	Maximum value of mutual inductance between a stator phase and an inner rotor phase in a three-phase system.
$M_{max\_sr\_ph}$	Maximum value of mutual inductance between a stator phase and an inner rotor phase in a single-phase system.
θ_{st_im}	Inner rotor position w.r.t stator in electrical radians.
θ_{st_pm}	Outer rotor position w.r.t. stator in electrical radians.
θ_{pm_im}	Inner rotor position w.r.t. outer rotor in Electrical radians.
ω_r	Rotational speed of inner rotor in rad/sec.
ω_{st}	Angular frequency of stator supply in electrical rad/sec and rotational speed of the outer rotor w.r.t stator in electrical rad/sec.
ω_{st}/p	Rotational speed of the outer rotor w.r.t stator in mechanical rad/sec.
t	Time
δ_{st_im}	Initial angle of inner rotor axis w.r.t. stator axis.
δ_{pm_im}	Initial angle of inner rotor axis w.r.t outer rotor axis.
δ_{st_pm}	Initial angle of outer rotor axis w.r.t. stator axis.
i_{xs}	Per-phase current of *x*-phase of stator.
i_{xr}	Per-phase current of *x*-phase of inner rotor.
α	Phase angle between stator voltage and current.

I_{max_s}	Maximum value of per-phase stator current.
φ_s	Stator field.
φ_{pm}	Outer rotor field.
φ_{im}	Inner rotor field.
E_r	Induced emf in inner rotor.
L_{rr}	Per-phase leakage inductance of inner rotor.
L_r	Per-phase self-inductance of inner rotor.
L_{ss}	Per-phase leakage inductance of stator.
L_s	Per-phase self-inductance of stator.
β	Inner rotor power factor angle.
v_{xs}	Per-phase voltage of x-phase of stator.
v_{xr}	Per-phase voltage of x-phase of rotor.
R_r	Inner rotor per-phase resistance.
R_s	Stator per-phase resistance.
λ_{xs}	Flux linkage of x-phase of stator.
λ_{xr}	Flux linkage of x-phase of inner rotor.
V_s	Stator phase voltage in phasor form.
I_s	Stator phase current in phasor form.
s	Slip of inner rotor.
W_{fld}	Magnetic field energy stored in the motor.
W_{co_fld}	Co-energy in motor.
T	Electromagnetic torque developed by motor.
P	Number of poles.
ϕ_{max_s}	Maximum value of permanent magnet flux linked by a phase of stator.
ϕ_{max_r}	Maximum value of permanent magnet flux linked by a phase of inner rotor.
θ_s	Angular displacement on the stator.
p	Number of pole pairs.

N_{ph} Number of series turns per phase.

$\Omega_{st\nu}$ Mechanical angular speed of rotating magnetic field for ν^{th} harmonic.

μ_0 Permeability of free space.

B_r Remanent magnetization of permanent magnet.

N_{OR} Speed of the outer rotor in rpm.

N_{IR} Speed of the inner rotor in rpm.

α_m Magnet fraction for permanent magnets.

T_{em}^{ir} Electromagnetic torque produced by inner rotor.

T_{em}^{or} Electromagnetic torque produced by outer rotor.

T_{em}^{T} Sum of electromagnetic torques produced by inner and outer rotors.

η Angular width of inner rotor bar

θ_q Initial angle of each rotor bar w.r.t reference axis.

δ Initial angle of the outer rotor in mechanical radians.

L_m Length of the motor in axial direction.

1

Introduction

Contents

1.1 Introduction

In recent times, a lot of attention is being given towards development of Electric Vehicles (EVs), however, commercialized EVs were introduced more than a century ago in the automobile market. In fact the EVs were the preferred mode of commuting in the late 19^{th} and early 20^{th} century [2,3]. Other alternatives available at that time were the steam engine vehicles (SEVs) and internal combustion engine vehicles (ICEVs) [4]. EVs were preferred over the competitors due to the following reasons:

- EVs were cleaner compared to the SEVs and ICEVs.
- SEVs and ICEVs used to produce a lot of noise and vibration, whereas, EVs' operation was almost vibrationless and very silent.
- SEVs and ICEVs required manual start using crankshaft and also gear shifts to drive, which made the drive cumbersome and undesirable.
- At that time, travel was mostly local in nature as roads were not well developed and with their limited range of operation, EVs were the perfect choice.

In the early 20^{th} century factors such as easy availability of gasoline, invention of electric starter by Charles Kettering and mass production of ICEVs by Henry Ford made ICEVs affordable and easy to drive. Moreover, the expansion in the road network improved connectivity among different cities and fueled the need of long range vehicles. EVs could not fulfil these demands of time and hence their popularity declined and gave rise to the era of ICEVs.

In recent years, EVs and Hybrid electric vehicles (HEVs) have regained the attention in the automobile sector [5–7]. This is mainly due to rising concerns of increasing air pollution, depleting fossil fuel reserves and increased greenhouse gas emissions. Road transport accounts for nearly 75% of the total transport greenhouse gas emission [8]. These factors are forcing the current transportation system to be more efficient and less dependent on conventional sources of energy. With the advancements in power electronics, battery technologies, high speed programmable devices; EVs and HEVs offer promising solution to these challenges [7].

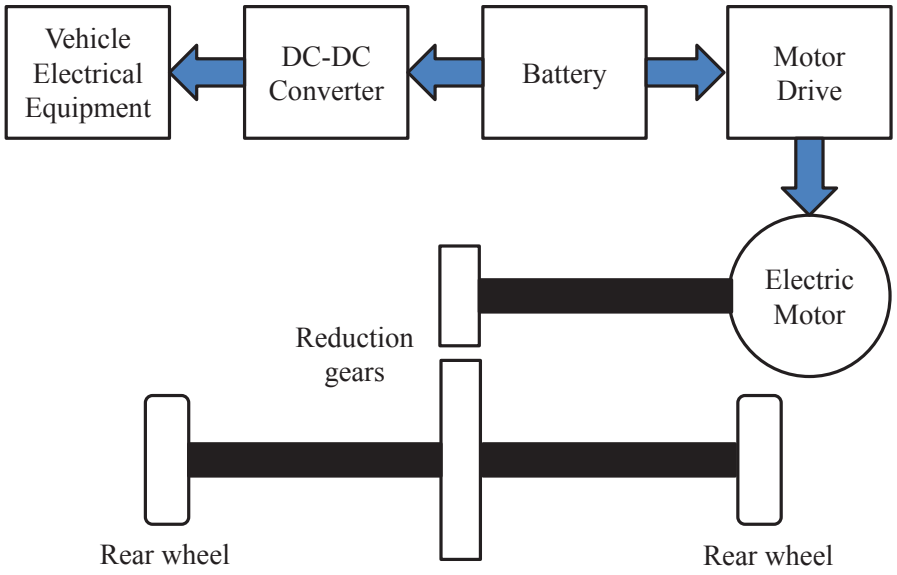

Figure 1.1: Typical system schematic of EVs.

Fig. 1.1 shows a typical system schematic for an EV [9]. It consists primarily of power source (battery), power converters, motor and peripheral devices. One of the most important part of an EV is its motor used for propulsion. An electric motor (EM) can be operated in a wide speed range. Advanced use of power electronics has enabled the use of conventional motors over wide range while maintaining its performance. An EM when properly controlled over its operating range can maintain efficiency of more than 90%, whereas ICE operates in an efficiency range of 30% – 45%. Thus, in comparison of ICE, EM has very high efficiency and therefore is suitable to be used for vehicle propulsion. Thus, aim of this thesis is to investigate the different types of motor being used in EVs presently and attempt to solve the challenges in their further development. In this regard, required characteristics of an EM for EV application need to be discussed.

1.2 Expected characteristics of motor drives for EVs

In an EV, EM is the only source of traction power. Therefore, it is desired that the operating characteristic of EM used for EV application must be similar to that of a vehicle. The Fig. 1.2 shows the desired torque and power characteristic for EM in EV application [10]. From the figure, it can be seen that the motor used in EV should have a small constant torque region and a large constant power region. The constant torque region is necessary to meet the starting and acceleration demands whereas the constant power region is important for high speed operation.

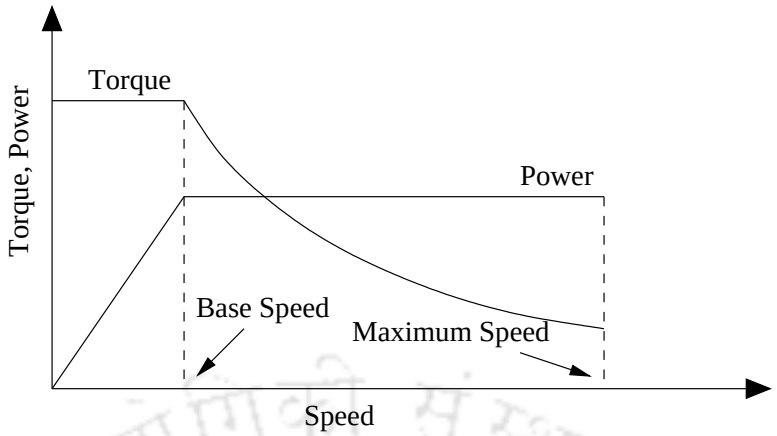

Figure 1.2: Desired output characteristics of electric motor drives in EVs.

Besides the characteristics shown in Fig. 1.2, the EMs for EVs must meet the following requirements:

- High power density.
- High torque at low speed and high power at high speed.
- Very wide speed range with constant power.
- Fast torque response.
- High efficiency over wide speed range.
- High efficiency in regenerative mode.
- High reliability and robustness for vehicle operating conditions.
- Reasonable cost.
- Fault tolerant.

There is no single motor that can meet all the above requirements. EV manufacturers have used different types of motors and it is necessary to do a comparative analysis of different types of motors. Following section presents a comparative study of different motors used for EV application.

1.3 Motors used in EVs

Different vehicle manufacturers have employed different types of motor for their EVs and HEVs. This section presents a comparative study of different motors used for EV application.

1.3.1 Brushed DC motor

The first EVs, used in 19^{th} century, were propelled by DC motors. Hence, these are the first motors to be used in EVs and still some low end EVs use DC motors. The biggest advantage of DC motors is that their torque-speed characteristic is very similar to that of an EV [11]. The other advantage being very simple control. However, DC motors suffer from many disadvantages such as bulky construction, low reliability and need of maintenance mainly due use of brushes for commutation action. The use of carbon brushes and commutators restrict the maximum speed at which DC motors can operate.

1.3.2 Permanent magnet brushless DC (PMBLDC) motor

PMBLDC motors are most preferred for EV application. This is primarily due to its high power density and efficiency in comparison to its competitors, which are very important factors from EV application viewpoint [12]. Due to the use of powerful permanent magnets, volume of PMBLDC is greatly reduced in comparison to the other motors in the same power range [13]. However, these motors have relatively small constant power range and in the constant power region magnets may get demagnetized also [14]. Cost and availability of permanent magnets is also one of the major concern for wide acceptance of these motors [15, 16].

1.3.3 Induction motor (IM)

In recent times, induction motors have emerged as favorable choice for EV application. IMs are preferred as they are reliable, rugged, require low maintenance and have low cost of manufacturing [17]. Since they were developed more than a century ago, the technology has matured very much over the period of time. Moreover, recent developments in power electronics and control techniques like vector control have enabled the decoupling of torque and field control resulting in precise control of motor torque and speed over a wide range [18]. Relative low power density and complex control are some of the disadvantages of IMs in comparison to other motors [19].

1.3.4 Switched reluctance motor (SRM)

SRMs are gaining much attention and are also being looked upon as a potential candidate for EV applications. These motors have the inherent advantages of simple and rugged construction, fault-tolerant operation, simple control, and outstanding torque-speed characteristics [20]. Torque-speed characteristic of SRM has very long constant power range which is a desirable feature for EV application. However, there are several disadvantages also, which for many applications outweigh the advantages. These disadvantages are acoustic noise, torque ripple, special converter topology, excessive bus current ripple and electromagnetic interference (EMI) [21, 22]. All of the above advantages as well as the disadvantages are quite critical for EV application.

A qualitative comparison of these motors based on indices which are very important to EV application is presented in Table 1.1 [10, 23]. For each index, motors are marked out of 5. From the table, it can be observed that PMBLDCM is most suitable for EV application. This is the reason, PMBLDCM are used generally in EVs.

Table 1.1: Motor comparison for EV application

	DC	PMBLDC	IM	SRM
Power density	2.5	5	3.5	3.5
Efficiency	2.5	5	3.5	3.5
Controllability	5	5	3	4
Cost	4	3	5	4
Total	**14**	**18**	**15**	**15**

1.4 Motivation

Electric vehicle (EV) application requires motor used in its drivetrain to be highly efficient, compact in size, of high power density and economic [24]. Different conventional motor types suffer from various disadvantages as discussed in the previous section. Thus, researchers are trying to develop a hybrid motor which is a combination of different conventional types and can overcome their shortcomings. An EV powertrain can also have multiple motors to meet better driving requirements [25], [26]. However, with multiple motors the powertrain requires multiple power converters, leading to complex powertrain architecture. In order to overcome this drawback and at the same time exploit the advantages of multiple motors, dual rotor motor (DRM) can be used [27]. Using DRM, a

given power output can be achieved with smaller size motor, reduced weight of winding and magnet materials [25]. DRM thus results in increased power density, reduced losses, high efficiency resulting in increased mileage per charge for an EV. Having two rotating parts, DRM is relatively complex machine. However, the potential and possibilities of DRM presents are motivating researchers to explore and understand different configurations and practical implementation of DRM.

1.5 Aim of the thesis

DRM has been a topic of research interest for last few years. In [28–30], it is shown that a DRM can be effectively used in hybrid electric vehicle to enhance its performance as a continuously variable transmission, and to achieve varied operational modes. In [29], multiple operational modes and control strategies for a dual rotor motor having PM and wound rotor has been presented. Having wound rotor as inner rotor, this machine requires two electrical connections with converters. In [31], electromagnetic design, construction and the experimental validation of double rotor permanent magnet synchronous machine mainly focusing on different slot-pole-slot combinations are presented. Authors in [25] have investigated the electromagnetic performance of double rotor permanent-magnet motor. In [32], authors have presented dual rotor machine with both the rotors with PMs mounted on them. The machine has single control. The two shafts of the motor have been connected to two separate loads. Electromagnetic analysis of DRM with two rotors with outer PM rotor and inner squirrel cage rotor is reported in [33]. Simplified equivalent circuit of the motor is also presented in the paper. However, justification of the equivalent circuit and verification of results is not presented adequately. It is seen from the literature that the configurations of the DRM investigated by authors are mainly have both PM rotors or one PM rotor and inner wound rotor. Also, most of the works on this fast emerging new type of motor, are only confined to applications and electromagnetic performances of the motor. The analysis of DRM from equivalent circuit and analytical viewpoint could not be found in the literature. In most of the reported works, the mechanical assembly of the motor is also not presented which makes practical realization of the concept difficult.

Keeping in view the contributions made in the literature, the aim of this thesis is to thoroughly investigate different configuration of DRM and then model, analyze and prototype the most suitable configuration of DRM.

1.6 Thesis contribution and organization

The major contributions of this thesis are:

(i) **Analytical and Finite Element Analysis (FEA) modeling of DRM:** Detailed 2-D magnetic model and equivalent circuit model of the motor are developed. Besides this, the FEA model of the motor is also developed and the results of the analytical and FEA models are compared. The analytical model is suitable for understanding the operation of the motor whereas the equivalent circuit model is suitable of analysis of the motor's behavior.

(ii) **Design:** The detailed lamination design of the DRM was done. The initial design was done using the analytical and equivalent circuit model and the final design was done using FEA.

(iii) **Prototyping:** A prototype of the motor was made based on the lamination designs obtained in step 2.

(iv) **Testing of the prototype:** The prototype of the motor was tested for various load conditions and its performance was recorded.

The prototype of DRM presented in the thesis is not an optimized one and power density and efficiency of the motor were not focused on. The presented motor is first prototype in the ongoing research work and thus considering the mechanical complexities and availability of resources, the scope of the practical work was limited to proof of concept of DRM and understanding of challenges involved. The lessons learnt during the process will be implemented during manufacturing of subsequent prototypes of DRM. The organization of the thesis is as follows:

Chapter 1:

This chapter consists of introduction of the thesis along with the detailed literature survey. Finally the motivation for the thesis work and aim of the thesis has been presented.

Chapter 2: This chapter aims to present an introduction to DRM and its various possible configurations. On the basis of the comparison presented in the chapter, a final configuration for further study has been presented.

Various configurations are possible for DRM based on different stator and rotor type and positions of movable and stationary parts. This chapter discussed these possibilities in detail. Finally based on the operating principle, feasibility, controllability, economy and ease of manufacturing, a final configuration has been selected for further analysis.

Chapter 3:

Design phase of any electrical machine mostly involves many iterations for various motor parameters. Therefore, analytical models are preferred over FEA, due to high computational time required by the latter [34]. The implementation of the analytical model is also economical and gives us a basic platform to improve the model further in terms of design and performance [35]. In literature, researchers have analyzed various configurations of DRM from different view points viz. application, operational modes, slot-pole-slot combinations [25, 28, 29, 31]. Along with the viewpoints presented by the authors, analysis of the motor from electromagnetic viewpoint is also important [36–38]. Therefore, development of analytical model to understand the DRM from electromagnetic viewpoint has been chosen as the objective of this chapter.

Chapter 4:

In this chapter, development of steady state model (SSM) comprising of electrical equivalent circuit (EEC) and torque equation is presented.

A SSM of any motor drive helps in understanding its operation, steady state performance characteristics, and an electrical representation for the magnetic field interaction between the motor parts [39]. During the design stage of a motor which is an iterative process [40], the motor performance can be checked from SSM which gives a much faster results as compared to precise but time consuming FEA.

Chapter 5:

In this chapter, design and prototyping of DRM have been discussed. Electrical and mechanical challenges faced during the manufacturing of the motor are presented. Various processes involved in the manufacturing of the motor are presented in detail. Pictures of various motor parts along with their mechanical designs and the various stages of assembly are also presented for better understanding.

Chapter 6:

This chapter presents testing of the manufactured DRM. Various tests have been performed on DRM to thoroughly understand its performance. The experimental results are also compared with FEA model and SSM results.

Chapter 7:

In this chapter conclusions and possible directions for future work are presented.

2

Dual rotor motor: Operating principle and possible configurations

Contents

2.1 Introduction

An electrical motor is an electromechanical device which converts electrical energy into mechanical energy. Electrical energy to the motor is supplied through windings on stator and rotor of the motor and mechanical energy is extracted through the rotor of the motor using mechanical coupling with the load. The parts of the motor, where electrical connections are provided are called electrical ports (EP) and parts where mechanical coupling are done are called as mechanical ports (MP) of the motor. Most of the conventional motors have at most 2 electrical ports (stator and rotor) and 1 mechanical port (rotor).

DRM has three parts, out of which two parts are movable and one is stationary. Each part of DRM can be an electrical port. As shown in Fig. 2.1, DRM can thus have at the most two MPs (two movable parts) [29] and three EPs (one stationary and two movable parts). When the mechanical ports of an electric machine increase, a lot of new possibilities for different motor configurations emerge.

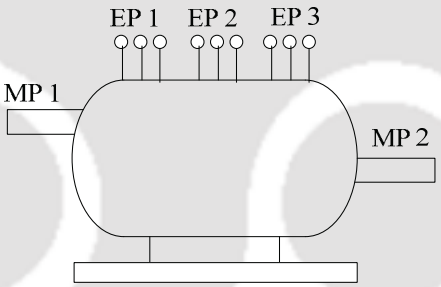

Figure 2.1: Schematic of 3 EP, 2 MP motor.

Various configurations are possible for DRM based on different stator and rotor type and positions of movable and stationary parts. Following sections describe the various possible configurations. Finally based on the operating principle, feasibility, controllability, economy and ease of manufacturing, a final configuration has been selected for further analysis.

2.2 Possible Configurations of DRM based on conventional motor types

The torque produced by a motor can be broadly classified as interaction torque and reluctance torque. In Fig. 2.2 classification of machines, based on the type of torque, is shown. Machines in the category of interaction torque can have same type of electrical winding whereas, for machines operating with reluctance torque, special winding arrangement is required. Fig. 2.2 shows a broad

classification of motors and almost all the motors fall in this classification table. Any other motor available in the literature are either variant of these basic types or hybrid combination of them. Therefore, DRM is also essentially made of these basic motor types. Considering all motor types, a lot of combinations are possible for a hybrid motor like DRM. Since any motor can have only one stationary part and generally it is preferred to have electrical winding on the stationary part. Thus, for DRM, type of machines which can operate with same type of winding have been chosen. These machines are shown with highlighted area in Fig. 2.2. Using these motor types as different parts (one stationary and two movable) of DRM, possible configurations are given in Table 2.1.

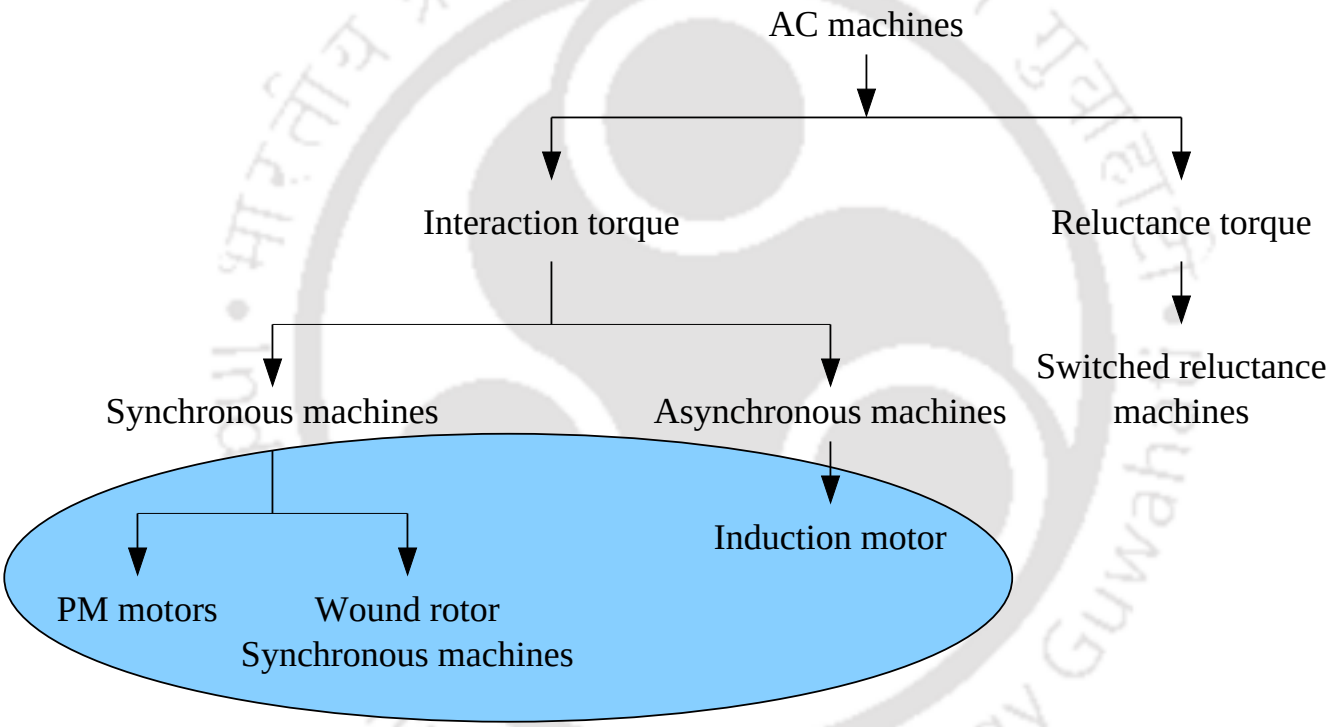

Figure 2.2: Classification of AC electrical machines based on torque production.

Table 2.1: Motor configurations on basis of basic motor types.

Type	Stator	Outer Rotor	Inner Rotor
Type I	3-phase winding	Squirrel cage	Squirrel cage
Type II	3-phase winding	Squirrel cage	Wound rotor
Type III	3-phase winding	Wound rotor	Squirrel cage
Type IV	3-phase winding	Wound rotor	Wound rotor
Type V	3-phase winding	PM	PM
Type VI	3-phase winding	PM	Squirrel cage
Type VII	3-phase winding	Squirrel cage	PM
Type VIII	3-phase winding	Wound rotor	PM
Type IX	3-phase winding	PM	Wound rotor

Table 2.1 shows nine configurations. In each configuration, the stator remains same and the configuration and location of rotors differ. For example in type VI, the cage rotor is located inside the PM motor and in Type VII the PM rotor is placed inside the cage rotor. In order to chose the final configuration for further analysis, following important points have been considered:

- 3-phase winding has been put on stator because if any moving part is made an EP then brushes are required for connections causing possibility of sparks and need regular maintenance for the motor. Therefore, configurations with 3-phase winding on the stator have only been considered as feasible options.

- As the objective with DRM is to make a motor with high power density, two stators will occupy more space and will also make the motor heavy. Thus, only configurations with one stators are considered.

- A three phase stator with distributed winding is chosen because such stators are common for PM and IM motors.

- With IM rotor, two type of rotors are possible i.e. wound rotor and squirrel cage rotor. In this work squirrel cage rotor has been preferred due to their well known advantages such as ruggedness, ease of manufacturing and no maintenance compared to wound rotor motor [17].

- Since the objective of DRM is to develop a motor with high torque and power density in comparison to the motor available for electric vehicles (mainly PM motors), one of the rotors has

been chosen as PM rotor. In the initial design of DRM, rare earth permanent magnets have been used. However, in future, ferrite magnets will be used such that DRM can be more economic in comparison to PM motors.

- The other rotor can be again PM rotor or squirrel cage rotor. One more PM rotor may have huge impact on the cost of the motor as rare earth PMs have very high cost, therefore, the other rotor has been chosen as squirrel cage rotor. To improve the power density, a copper cast cage rotor is used.

- The configuration with two squirrel cage rotor will not have sufficiently high power density as out of three parts of DRM only stator will serve as excitation. Also, as the cage rotor does not have own excitation and is dependent on stator, one more cage rotor will need stator to have more reactive power for exciting both the rotors

Thus, from this discussion, out of the IX configurations presented in Table 2.1, only the configurations with PM and cage rotor are chosen. The detailed analysis of these configurations is given in the following section.

2.3 Possible Configurations of DRM based on positions of motor parts

This section describes the feasible configurations of DRM with different positions for the parts selected in previous section. DRM has three independent parts as shown in Fig. 2.3. Any of these parts can be stator or rotor. Thus using the type of motor parts selected in previous section, feasible combinations are presented in Table 2.2.

It can be seen in Fig. 2.3, part III is the innermost part in the motor and thus will have very less space in comparison to the other parts. Therefore, it will not be practically feasible to place 3-phase winding in the innermost part as it requires more space for conductor placement as well as better cooling of the winding, thus configurations **M5** and **M6** are ruled out. Figs. 2.4-2.7 show motor models for remaining four combinations **M1-M4**. In model **M3** and **M4**, middle part (part II) acts as stator and excitation for inner and outer rotors thus, it must have two set of windings both the rotors as shown in Figs. 2.6 and 2.7. For the purpose of easy representation, the PM rotor is presented as ring of magnets.

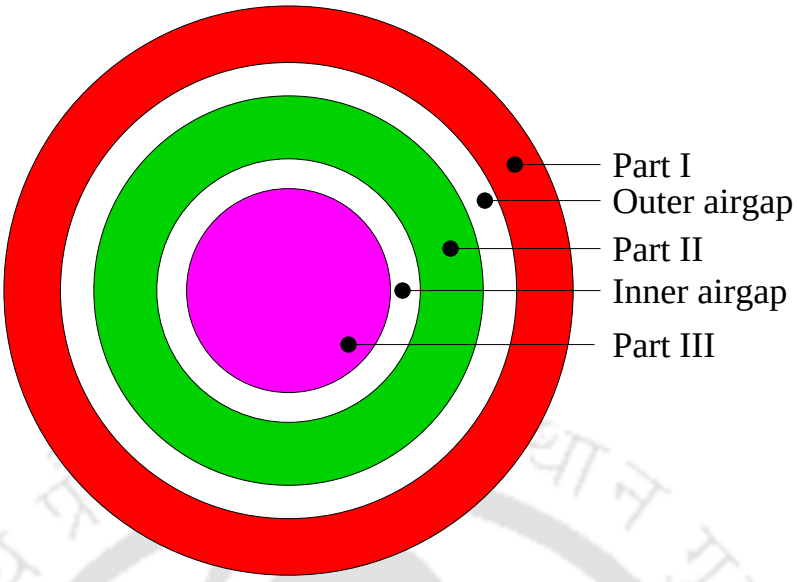

Figure 2.3: Hybrid IM-PM DRM schematic.

Table 2.2: Motor classification on basis of motor part type.

	Part I	**Part II**	**Part III**
M1	3-phase winding	Squirrel cage	PM
M2	3-phase winding	PM	Squirrel cage
M3	Squirrel cage	3-phase winding	PM
M4	PM	3-phase winding	Squirrel cage
M5	PM	Squirrel cage	3-phase winding
M6	Squirrel cage	PM	3-phase winding

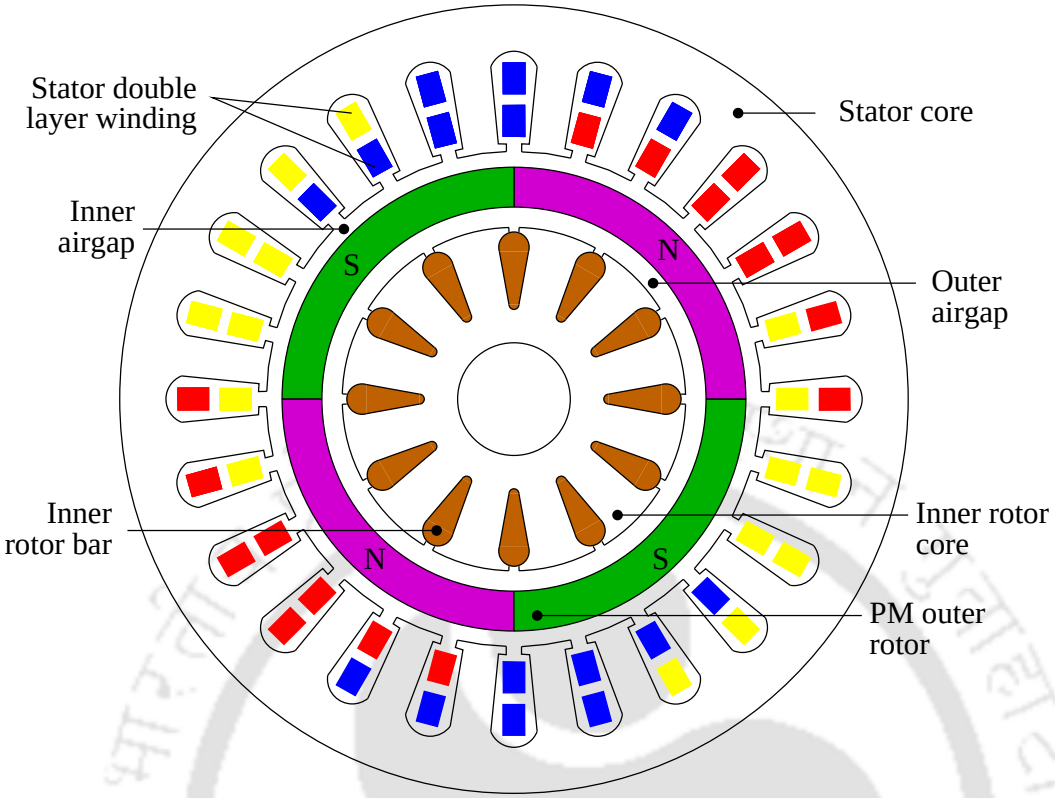

Figure 2.4: DRM model for configuration **M1**.

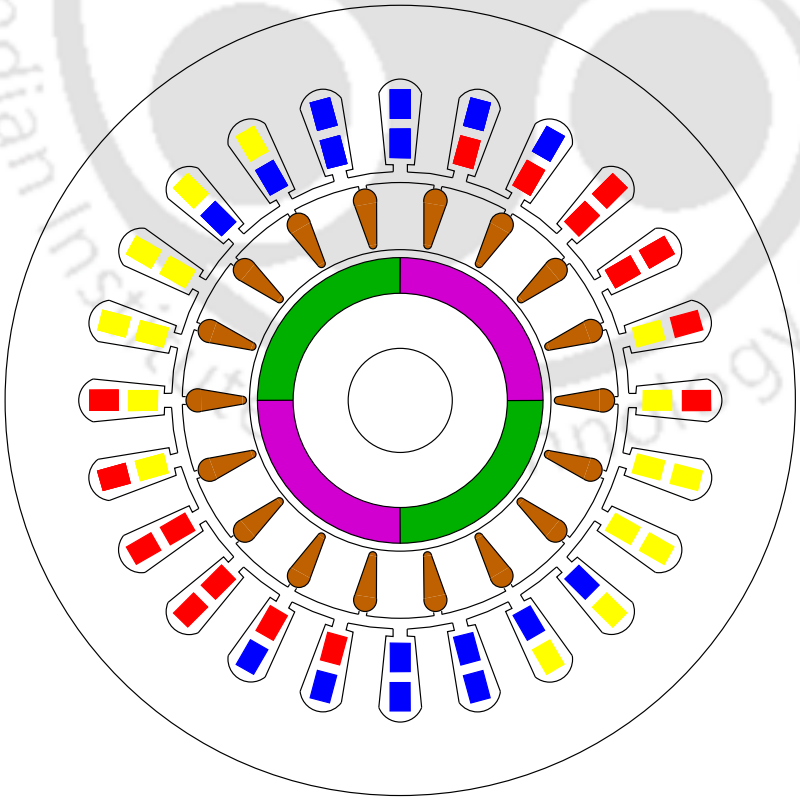

Figure 2.5: DRM model for configuration **M2**.

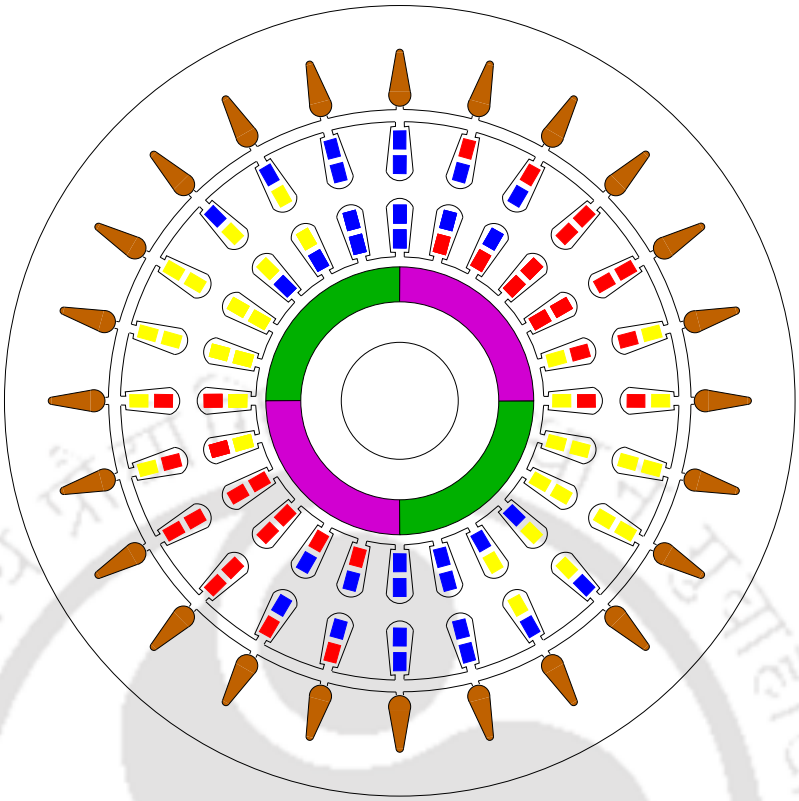

Figure 2.6: DRM model for configuration **M3**.

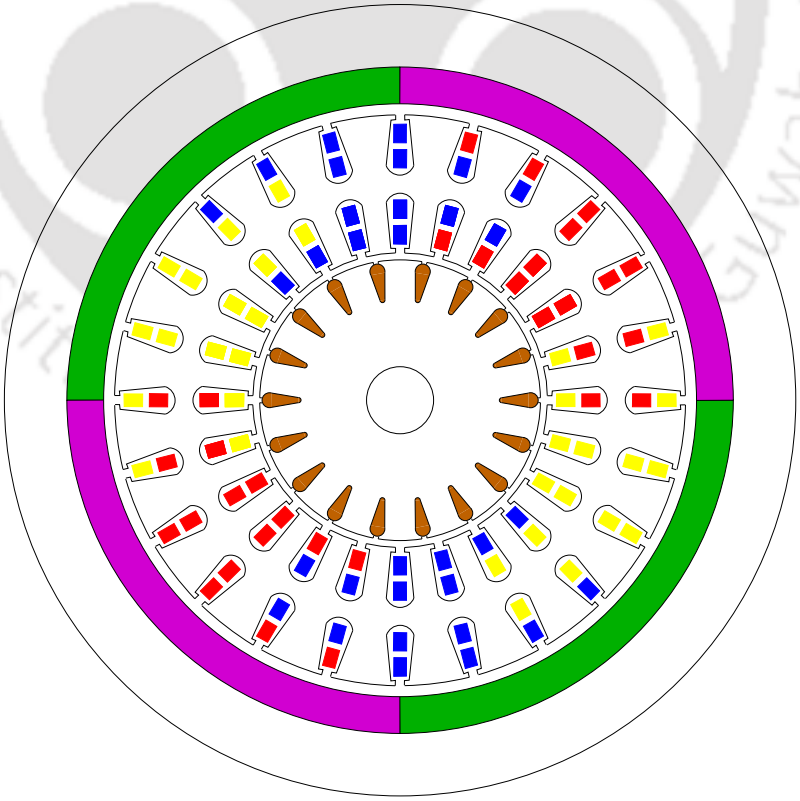

Figure 2.7: DRM model for configuration **M4**.

Out of the four models, the final model is selected based on feasibility and qualitative analysis of each model. The next section describes the working principle of DRM and quantitative analysis for the configurations **M1-M4**.

2.4 Working principle of DRM

The DRM analyzed in this work can be conceptualized to comprise two concentric motors. First motor is formed with the stator and the permanent magnet rotor, operating as a PMSM. The second motor is formed with the stator and squirrel cage rotor, operating as an induction motor. With the stator energized from a three-phase supply, the PM rotor rotates at synchronous speed. The cage rotor rotates at a speed less than the synchronous speed depending upon the slip at which it is operating. The DRM has two air-gaps and thus two torque producing ports which can be coupled using a planetary gear to drive an electric vehicle (EV) [29, 30, 41]. Fig. 2.8 shows the schematic representation of the analyzed DRM. Possible combinations of the mutually coupled coils in the DRM and the energy conversion caused by the coupling fields across the two air-gaps are shown in this figure. The stator and inner rotor copper losses have also been shown in the figure. Core losses in stator, outer rotor and inner rotor caused due to the rotation of coupling field has been represented as coupling field losses in the figure. It can also be observed that the electric power supply is given only to the stator and the mechanical power is extracted from the two rotors.

2.5 FEA analysis of models M1-M4

Figs. 2.9-2.12 present the flux distribution for configurations **M1-M4** using FEA. The FEA analysis of these and all the models presented in this thesis have been performed with Ansoft Maxwell software with version 14.0.0. The analysis have been performed with Maxwell 2D, transient solution. For the FEA analysis triangular elements have been used and the maximum size of the elements was set to 2 mm. For the computation backward Euler solution method has been used.

All the models presented in this section are voltage excited models with rms phase voltage 415 V. The PMs in the models have remanent flux density of 1.2 T. It can be observed from these figures that the working flux in the analyzed DRM links all the three cores, i.e. continuous flux lines pass through both the air-gaps. These continuous flux lines are responsible for producing interdependent torques in both the air-gaps. Relative speed between the stator flux and synchronously rotating outer

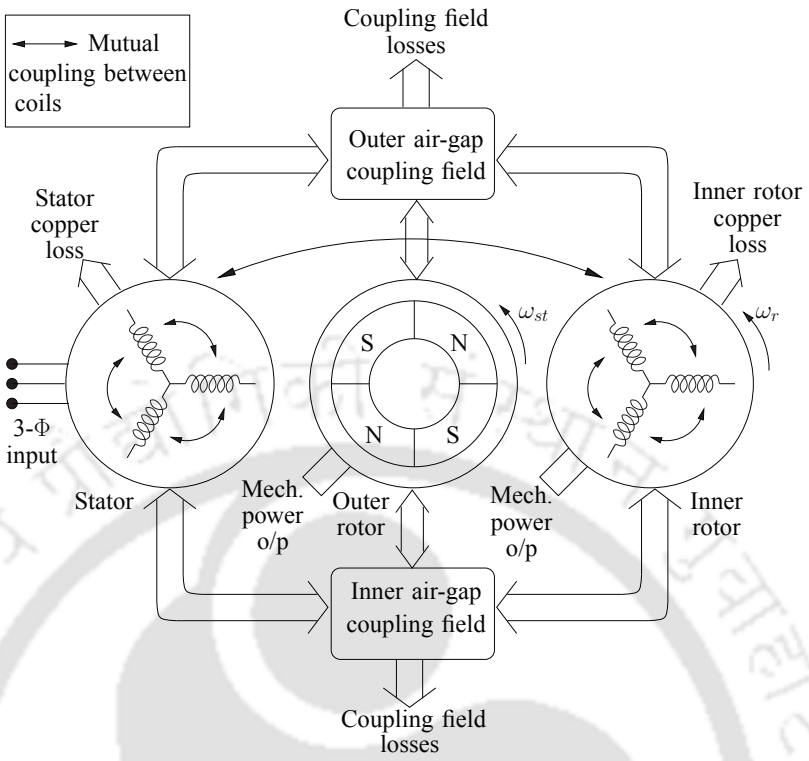

Figure 2.8: Schematic representation of analyzed DRM showing mutually coupled coils and electromechanical energy conversion.

rotor flux is zero, and similarly the relative speed between outer rotor flux and inner rotor flux is also zero. It can be observed from this discussion that the motor satisfies the condition for average power conversion, i.e. all the magnetic fields in the motor are stationary w.r.t. each other.

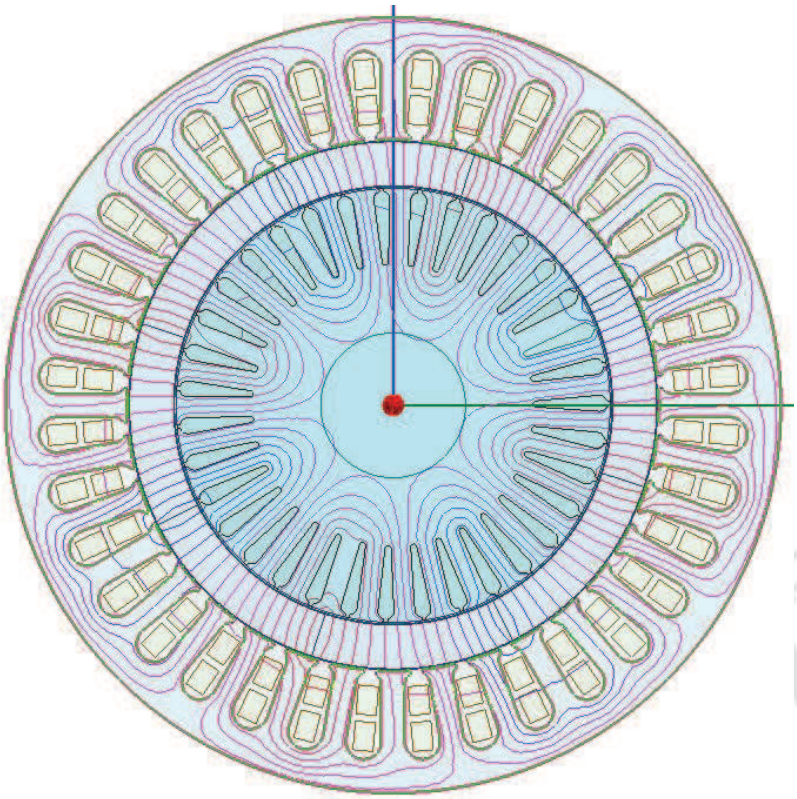

Figure 2.9: Flux distribution for configuration **M1**.

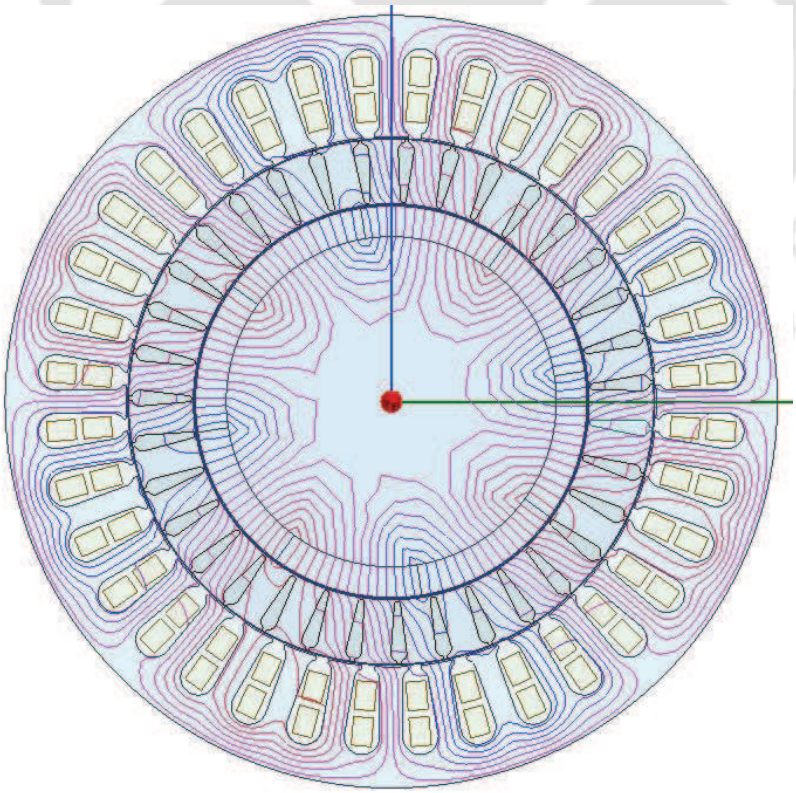

Figure 2.10: Flux distribution for configuration **M2**.

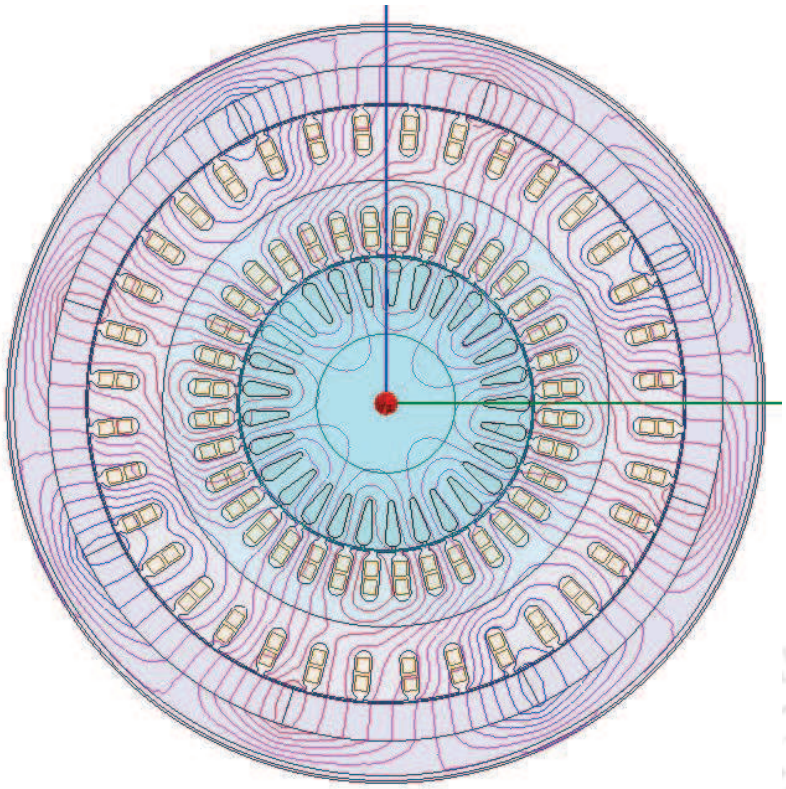

Figure 2.11: Flux distribution for configuration **M3**.

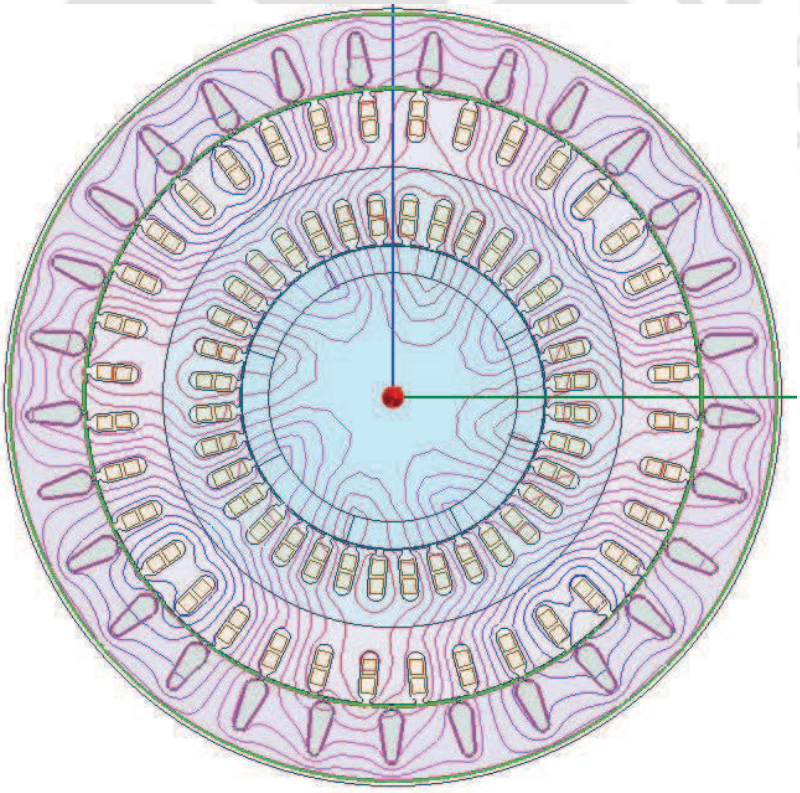

Figure 2.12: Flux distribution for configuration **M4**.

In order to select one configuration out of **M1-M4** following important points are considered:

- Among all the configurations, **M1** and **M2** have a very uniform flux distribution in comparison to **M3** and **M4**. It can be observed from the figures that, in **M3** and **M4**, all the flux lines does not link all the three parts of motor and the cage rotor in both **M3** and **M4** configurations link very few flux lines. Also the distribution of flux lines is also non-uniform along the periphery of the motor. Thus, in **M3** and **M4** configurations may result in local saturation in some parts of the motor and **M1** and **M2** configurations will result in better utilization of the core.

- Configurations **M3** and **M4** requires two sets of 3-phase windings to be placed on the stator. Practically, it will require large space to place conductors for both the windings.

- It is observed that in **M2**, some of the flux lines link only stator and cage rotor without linking the inner PM rotor and thus is not efficient utilization of flux. Whereas, in **M1**, all the flux lines links the outer as well as the inner rotor and the flux is also uniformly distributed along the periphery of the motor. Also, in **M2**, cage rotor is the outer rotor and does not have sufficient core width for die cast of the cage rotor. Whereas, **M1** has a cage type of rotor which is used in an IM and thus can be manufactured easily.

Thus, from this discussion it is concluded that **M1** has a good flux distribution and is also relatively easy to manufacture. Thus, the configuration **M1** will be thoroughly analyzed in the rest of the thesis. However, all methodologies presented for analysis in the thesis are applicable to any other configuration of DRM.

2.6 Summary and Conclusion

In this chapter, an introduction to DRM and various possible configurations have been presented. Using different types of conventional motors and their relative positions, many combinations are possible for DRM. Considering working principle, feasibility, economy and ease of manufacturing, one configuration has been selected for further analysis. The selected configuration has PMs on outer rotor and inner rotor is squirrel cage type. Flux distribution in the selected configuration is also analyzed. This selected configuration will be analyzed in the rest of thesis. Next chapter presents analytical model to analyze magnetic field in both the air-gap and torque production in the air-gaps.

3

2-D Analytical Subdomain Model for DRM

Contents

3.1 Introduction

The DRM configuration considered for analytical model is the one finalized in the previous chapter with squirrel cage (SC) and PM rotors. The PM rotor rotates at synchronous speed and the SC rotor rotates at some speed less than the synchronous speed.

Subdomain modeling is a analytical method that involves division of the problem into physical regions named subdomains in which Maxwell governing equations can be solved analytically [42]. The main goal of this work is to understand the phenomenon of torque production in DRM using the analytical model. Torque in the motor is calculated from the air-gap magnetic field in both the air-gaps in the motor. To avoid deviation from the main goals of the work and to keep the mathematical model simpler, the assumptions made are given in the next section. Governing equations, boundary condition in the analytical model are presented in Section 3.3. Results from analytical model and their comparison with FEA are given in Section 3.4.

3.2 Motor Geometry and Assumptions

The basic configuration of DRM considered for this work is same as presented in previous chapter. The outer rotor has PM on it and the inner rotor has squirrel cage like structure as in case of a squirrel cage type IM. However, the geometry has been modified to reduce complexity for analytical modeling. Fig. 3.1 shows the configuration of the DRM motor considered in this work. The outer rotor is made of ring shaped PM and inner rotor has slots with conducting rotor bars having electrical conductivity σ. The bars in SC rotor have radial sides and are short circuited by end rings at both ends. η denotes the angular width of the inner rotor bar. Due to the presence of two rotors, DRM has two air-gaps namely inner and outer air-gap. To represent the stator current, current sheet distributed over inner stator surface ($r = R_s$) has been used. Important parameters defining the geometry and their symbols are given in Table 3.1. Following assumptions have been made to facilitate the problem formulation:

- End effects are neglected.
- Stator and rotor core are taken to be of infinite permeability.
- All the magnetic vector potentials of various regions have only z-direction component.

- Permanent magnets have constant permeability and constant remanent flux density.
- The stator windings have been represented with a current sheet.
- The PM region and air-space between magnets (in case $\alpha_m \neq 1$) have relative permeability μ_m.

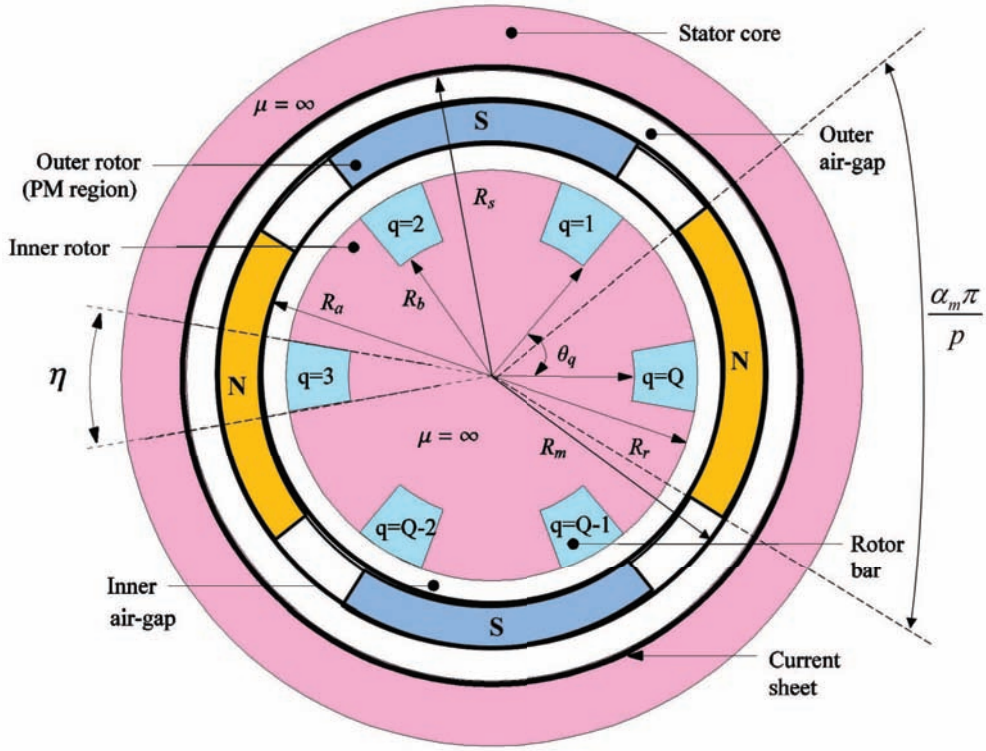

Figure 3.1: Configuration of the hybrid IM-PM DRM motor [1].

Table 3.1: Parameters Defining Motor Geometry and their Symbols

Parameter	Symbol	Parameter	Symbol
Stator inner radius	R_s	Inner radius of cage rotor bar	R_b
PM rotor outer radius	R_m	Cage rotor outer radius	R_r
PM rotor inner radius	R_a	Angular width of inner rotor bar	η
Number of cage rotor slots	Q	Magnet fraction	α_m

Development of analytical model, based on the motor geometry and assumptions discussed here, is described in the next section.

3.3 Analytical model

In the present analysis, field calculation is done using magnetic vector potential. The complete geometry is divided into the following four regions:

(i) Outer air-gap region (*oa*).

(ii) PM region (*m*).

(iii) Inner air-gap region (*ia*).

(iv) Rotor bar region (*b*).

The alphabets in the bracket represent the notation used for that region. The DRM has two types of excitation i.e. PM excitation and stator current excitation. These are modeled with the help of their Fourier series representation as explained in subsequent subsections.

3.3.1 Equivalent current sheet distribution

In an electrical machine, excitation windings are placed in the slots on stator or rotor core. Analytically it is very difficult to model the exact winding region and hence current sheet is used very often to represent the stator current. In this work, the stator windings are considered as an equivalent current sheet distributed over the stator inner radius for simpler analysis. The formulation of [43] is followed in this subsection. The sinusoidal current density over R_s with respect to time for ν^{th} space harmonic component is given as:

$$J_\nu(\theta_s, t) = J_{max}\cos(\nu p\theta_s - \omega_{st}t) \tag{3.1}$$

where, θ_s is the angular displacement on the stator, J_{max} is the maximum value of harmonic component, p is the number of pole pairs, ω_{st} is the angular frequency of stator supply and t represents time.

In case of 3-phase stator winding with integer slots per pole per phase, harmonics present in the current sheet are given by (3.2).

$$\nu = 1 \pm 6l \qquad \text{where} \qquad l = 0, 1, 2, 3... \tag{3.2}$$

The maximum value J_ν for ν^{th} harmonic is given by (3.3).

$$J_\nu = \frac{3N_{ph}I\sqrt{2}}{\pi R_s}K_{w\nu} \tag{3.3}$$

where, N_{ph} is the number of series turns per phase and I is the stator rms current. The winding factor $K_{w\nu}$ depends on the arrangement of coils in the stator slots and is given by (3.4).

$$K_{w\nu} = \sin\left(\frac{|\nu|\pi}{2}\right)\sin\left(\frac{|\nu|\lambda}{2}\right) \times \frac{\sin\left(\frac{|\nu|\pi}{6}\right)}{q\sin\left(\frac{|\nu|\pi}{6q}\right)} \frac{\sin\left(\frac{|\nu|\varepsilon}{2}\right)}{\left(\frac{|\nu|\varepsilon}{2}\right)} \tag{3.4}$$

where, q is the number of slots per pole per phase, λ is the coil pitch and ε is the width of the slot opening in radians. Absolute values of ν is considered in 3.4 as winding factor can only be a positive value.

Each harmonic produces rotating magnetic field in the machine. The magnetic field will have forward or backward motion based on the harmonic number and the mechanical angular speed of the rotating magnetic field is given by (3.5).

$$\Omega_{st\nu} = \frac{\omega_{st}}{\nu p} \qquad \begin{cases} \text{Forward} & \nu = 1, 7, 13... \\ \text{Backward} & \nu = -5, -11, -17... \end{cases} \tag{3.5}$$

3.3.2 Magnetization of Permanent Magnet

Permanent magnets in analytical models are represented with Fourier series expression of their magnetization. Expressions for different types of magnetization such as radial, parallel, radial sinusoidal amplitude and constant amplitude sinusoidal can be found in the literature [1, 44, 45]. In the present work, radially magnetized magnets have been considered. The magnetization vector is represented by the expression given in (3.6).

$$\vec{M} = \frac{\vec{B_r}}{\mu_0} \tag{3.6}$$

where, μ_0 is the permeability of free space and B_r is the remanent magnetization of permanent magnet. In polar coordinates, $\vec{M}$ is expressed by (3.7).

$$\vec{M} = M_r \cdot \vec{r} + M_\theta \cdot \vec{\theta} \tag{3.7}$$

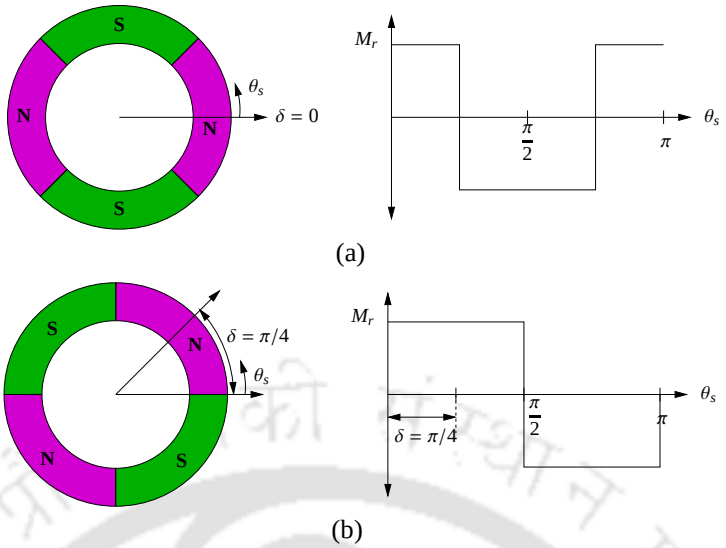

Figure 3.2: Rotor position for different initial angle of outer rotor (a) $\delta = 0$ (b) $\delta = \pi/4$.

where, $\overrightarrow{r}$ and $\overrightarrow{\theta}$ denote the direction vectors in radial and tangential direction. M_r and M_θ are the magnitudes of radial and tangential components of $\overrightarrow{M}$ respectively. The Fourier series expressions for these components are

$$M_r = \sum_{\nu=1,3,5...}^{\infty} M_{r\nu} \cdot \cos(\nu p\,(\theta_s - \delta) - \omega_{st\nu} t) \quad \forall \nu \tag{3.8a}$$

$$M_\theta = \sum_{\nu=1,3,5...}^{\infty} M_{\theta\nu} \cdot \sin(\nu p\,(\theta_s - \delta) - \omega_{st\nu} t) \quad \forall \nu \tag{3.8b}$$

where, $M_{r\nu}$ and $M_{\theta\nu}$ denote the ν^{th} harmonic element of the radial and tangential component, δ is the initial angle of the outer rotor in mechanical radians w.r.t. stator and $\omega_{st\nu}$ is the electrical angular rotational speed of magnetization for respective harmonic and is given as, $\omega_{st\nu} = \frac{2\pi N_{OR}\nu}{60}$. Where, N_{OR} represents the rotational speed of outer PM rotor in rpm. The physical significance of δ is presented in Fig. 3.2.

Different types of magnetization affect the field distribution in the motor. However, it does not change the procedure for magnetic field calculation. For radially magnetized magnets $M_{r\nu}$ and $M_{\theta\nu}$ are mathematically expressed as given by (3.9a) and (3.9b).

$$M_{r\nu} = 2\frac{B_r \alpha_m}{\mu_0} sinc\left\{\frac{\nu \alpha_m \pi}{2}\right\} \tag{3.9a}$$

$$M_{\theta\nu} = 0 \tag{3.9b}$$

Where, α_m is magnet fraction and $sinc(x) = \frac{\sin(x)}{x}$

Fig. 3.3 represents the pattern of magnetization of radially magnetized magnet showing its radial and tangential component with respect to spatial angle θ.

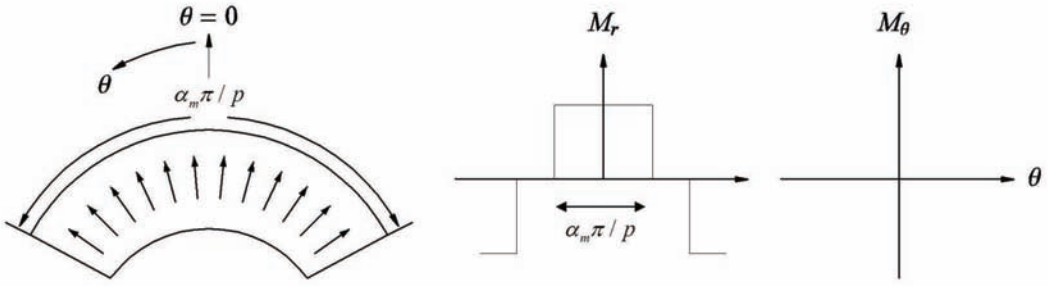

Figure 3.3: Radial magnetization of permanent magnet [1].

3.3.3 Inner rotor reference frame

The reference frame is changed from stator to inner rotor in this model. As mentioned earlier, there are two excitations (current excitation and PM excitation) in the machine. These are considered separately in the following subsections.

3.3.3.1 Current Excitation in inner rotor reference frame

If the inner rotor rotates with a constant angular velocity N_{IR}, the current sheet expression in stator reference frame (3.1) can be transformed to the rotor reference frame using (3.10) and is given by (3.11) [43].

$$\theta = \theta_s - N_{IR}t \tag{3.10}$$

$$J_\nu(\theta, t) = J_{max} \cos(\nu p\theta - \omega_{r\nu}t) \tag{3.11}$$

where, $\omega_{r\nu}$ is the frequency of the current induced in the cage rotor and is given as:

$$\omega_{r\nu} = (1 - \nu(1 - s))\omega_{st} \tag{3.12}$$

where, $s = \frac{\Omega_{st1} - N_{IR}}{\Omega_{st1}}$ and Ω_{st1} is the mechanical speed of fundamental magnetic field produced by stator and is given by (3.5).

3.3.3.2 PM Excitation in cage rotor reference frame

PM excitation given in (3.7) is also transformed in cage rotor reference form in the same way as current excitation and is expressed as:

$$\overrightarrow{M}_{\nu}(r,\theta,t) = M_{r\nu}\cos\left(\nu p\left(\theta-\delta\right)-\omega_{r\nu}t\right)\cdot\overrightarrow{r}$$

$$+\, M_{\theta\nu}\sin\left(\nu p\left(\theta-\delta\right)-\omega_{r\nu}t\right)\cdot\overrightarrow{\theta} \tag{3.13}$$

The primary difference between PM excitation and current excitation is that the synchronous speed of the rotating magnetic field produced by PM excitation changes with respect to ν in the PM excitation but doesn't vary with ν during current excitation. Therefore the following expressions changes in comparison to the current excitation.

$$\omega_{r\nu} = (1-\nu(1-s))\omega_{st\nu} \tag{3.14}$$

and $\omega_{st\nu} = \frac{2\pi N_{OR}\nu}{60}$. Where, N_{OR} represents the rotational speed of outer PM rotor in rpm.

While representing current excitation and PM excitation in cage rotor reference frame, the frequency $\omega_{r\nu}$ must be taken carefully as given in (3.12) and (3.14) respectively. The only factor varying between current excitation and PM excitation, in $\omega_{r\nu}$, is the electrical synchronous speed. In the case of current excitation the electrical synchronous speed of the field always remains $\omega_{st} = 2\pi f$, whereas in PM excitation the effective synchronous speed becomes $\omega_{st\nu} = \frac{2\pi N_{OR}\nu}{60}$ for a particular space harmonic (ν). This is because, in the former case the synchronous speed depends on frequency of excitation and thus changes with time harmonics. Whereas, in case of PM excitation it changes with space harmonics (ν). Figs. 3.4 and 3.5 present the change of poles in one electrical cycle for two harmonics $\nu = 1$ and $\nu = 2$.

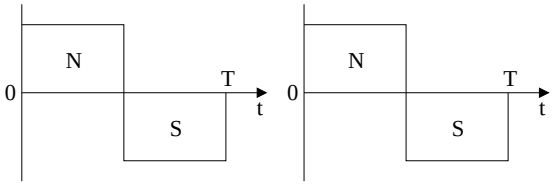

(a) (b)

Figure 3.4: One electrical cycle with Current excitation (a) $\nu = 1$ (b) $\nu = 2$

As discussed earlier synchronous speed due to current excitation depends on time harmonic and

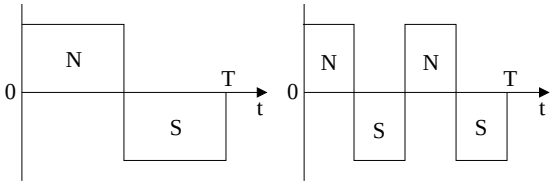

Figure 3.5: One electrical cycle with PM excitation (a) $\nu = 1$ (b) $\nu = 2$

therefore number of poles in Fig. 3.4(a) and 3.4(b) are same. Whereas, in case of PM excitation, the synchronous speed varies with space harmonic ν and therefore number of poles in one electrical cycle becomes double for $\nu = 2$ in Fig. 3.5(b).

3.3.4 Magnetic Field Calculation

3.3.4.1 Governing Equations

Vector potential in each region is governed by the governing equation in that particular region. In rotor bar region, induced current will be developed due to current sheet and PM rotor and thus Helmholtz equation is employed and is given as:

$$\frac{\partial^2 A_b^q}{\partial r^2} + \frac{1}{r}\frac{\partial A_b^q}{\partial r} + \frac{1}{r^2}\frac{\partial^2 A_b^q}{\partial \theta^2} = j\omega_{r\nu}\sigma\mu_o A_b^q \tag{3.15}$$

Where, A_b^q is the complex vector potential for q^{th} rotor bar region. The outer and inner air-gap regions are source free and hence are governed by Laplace's equation, given as:

$$\frac{\partial^2 A_{oa,ia}}{\partial r^2} + \frac{1}{r}\frac{\partial A_{oa,ia}}{\partial r} + \frac{1}{r^2}\frac{\partial^2 A_{oa,ia}}{\partial \theta^2} = 0 \tag{3.16}$$

Where, A_{oa} and A_{ia} are complex vector potential for outer and inner air-gaps respectively. The region with PM is governed by Poisson's equation and is given as:

$$\frac{\partial^2 A_m}{\partial r^2} + \frac{1}{r}\frac{\partial A_m}{\partial r} + \frac{1}{r^2}\frac{\partial^2 A_m}{\partial \theta^2} = -\mu_0 \nabla \times \vec{M} \tag{3.17}$$

Where, A_m is the complex vector potential for magnet region and $\vec{M}$ is the magnetization of the PM.

3.3.4.2 Potential Functions

In this section, potential functions satisfying the governing equations in different regions are defined. In order to find magnetic field in any region either scalar or vector magnetic potentials may be defined. If the scalar magnetic potential (ϕ) is considered in region then the magnetic field intensity

in that region is given by (3.19).

$$H = -\nabla\phi \tag{3.18}$$

This definition must satisfy the Ampere's circuital law i.e.

$$\nabla \times H = J = \nabla \times (-\nabla\phi) \tag{3.19}$$

However, the curl of the gradient of any scalar is identically zero. Therefore, if scalar magnetic potential is to be selected for a region, then current density must be zero throughout the region in which the scalar magnetic potential is defined, given as

$$H = -\nabla\phi \qquad (J = 0) \tag{3.20}$$

However, if vector magnetic potential (A) is selected for a region, the flux density is given by (3.21).

$$B = \nabla \times A \tag{3.21}$$

This automatically satisfies the condition that the magnetic flux density shall have zero divergence (Gauss's law) and the curl of vector field is also non zero with vector magnetic potential as shown in (3.22) and (3.23).

$$\nabla \cdot B = \nabla \cdot (\nabla \times A) = 0 \tag{3.22}$$

$$\nabla \times H = J = \frac{1}{\mu_0 \mu_r} \nabla \times \nabla \times A \tag{3.23}$$

Thus, magnetic vector potential can be used for all regions whereas, scalar magnetic potential can be used only in the regions which are free from electric current. Since, for the considered geometry of DRM, current will be induced in the inner rotor bars, magnetic vector potentials are used for all the regions. As explained in the Section 3.2, magnetic vector potentials for various regions will have only z component. The vector potential in rotor reference frame for all the regions vary sinusoidally with a frequency $\omega_{r\nu}$. Therefore, all the potentials can be represented with complex notations, given as:

$$\overline{A_b^q}(r, \theta, t) = \mathrm{Re}\left\{A_b^q(r, \theta)\, e^{j\omega_{r\nu} t}\right\} \tag{3.24}$$

$$\overline{A_{ia}}(r, \theta, t) = \mathrm{Re}\left\{A_{ia}(r, \theta)\, e^{j\omega_{r\nu} t}\right\} \tag{3.25}$$

$$\overline{A_m}(r,\theta,t) = \mathrm{Re}\left\{A_m(r,\theta)\, e^{j\omega_{r\nu}t}\right\} \tag{3.26}$$

$$\overline{A_{oa}}(r,\theta,t) = \mathrm{Re}\left\{A_{oa}(r,\theta)\, e^{j\omega_{r\nu}t}\right\} \tag{3.27}$$

where, Re represents real part of complex function and $j = \sqrt{-1}$. It is to be noted that all the potential functions are evaluated for each harmonic ν individually and will have different set of Fourier coefficients for each harmonic. However, ν has not been used for neatness in all above expressions. Similarly, current and magnet excitation are also represented with complex notations as given in (3.28) and (3.29) respectively. The real quantities are differentiated from their corresponding complex quantities with a bar over them.

$$\overline{J_\nu}(\theta,t) = \mathrm{Re}\left\{J_\nu(\theta)e^{j\omega_{r\nu}t}\right\}, \quad J_\nu(\theta) = J_{max}e^{-j\nu p\theta} \tag{3.28}$$

$$\overline{\vec{M}_\nu}(r,\theta,t) = \mathrm{Re}\left\{\vec{M}_\nu(r,\theta)e^{j\omega_{r\nu}t}\right\},$$

$$\vec{M}_\nu(r,\theta) = M_{r\nu}e^{-j\nu p(\theta-\delta)}\cdot\vec{r} + M_{\theta\nu}e^{-j(\nu p(\theta-\delta)-\pi/2)}\cdot\vec{\theta} \tag{3.29}$$

Potential function for a particular region is chosen based on its governing equation as well as geometrical constraints for that particular region. Development of potential functions for different regions are discussed below.

The various boundary conditions for q^{th} inner rotor bar are shown in Fig. 3.6. Since the iron core

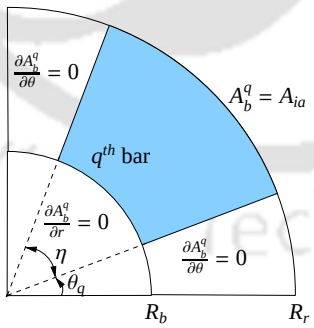

Figure 3.6: q^{th} inner rotor bar with boundary conditions.

surrounding the rotor bar is assumed to be infinitely permeable, the tangential component of magnetic field at all the iron boundaries is zero. The formulation of [43] is followed in this subsection. In terms of A_b^q, these are given as:

$$\left.\frac{\partial A_b^q}{\partial \theta}\right|_{\theta=\theta_q} = 0 \qquad \text{and} \qquad \left.\frac{\partial A_b^q}{\partial \theta}\right|_{\theta=\theta_q+\eta} = 0 \tag{3.30}$$

$$\left.\frac{\partial A_b^q}{\partial r}\right|_{r=R_b} = 0 \tag{3.31}$$

The continuity condition between q^{th} bar and inner airgap results in:

$$A_b^q(R_r, \theta) = A_{ia}(R_r, \theta) \tag{3.32}$$

General solution for (3.15) is obtained by using variable separation method. A_b^q is expressed as product of two functions of one variable θ and r each.

$$A_b^q(r, \theta) = \rho^q(r) \cdot \Theta^q(\theta) \tag{3.33}$$

Substituting (3.33) in (3.15), following two ordinary differential equations are obtained, where Λ is called as separation constant [46].

$$\Theta^{q''} + \Lambda\Theta^q = 0 \tag{3.34}$$

$$r^2\rho^{q''} + r\rho^{q'} + \left(\alpha^2 r^2 - \Lambda\right)\rho^q = 0 \tag{3.35}$$

where $\alpha^2 = -j\omega_{r\nu}\sigma\mu_0$, (3.35) is Bessel differential equation. Using (3.33), the boundary condition (3.30) become

$$\Theta^{q'}(\theta^q) = 0 \qquad \text{and} \qquad \Theta^{q'}(\theta^q + \eta) = 0 \tag{3.36}$$

Now, values of Λ needs to be obtained which should give nontrivial solutions of (3.34) and also satisfies the boundary conditions in (3.36). This is standard Sturm-Liouville problem [46]. The eigenvalues for this problem are:

$$\Lambda_0 = 0 \qquad \text{and} \qquad \Lambda_h = \left(\frac{h\pi}{\eta}\right)^2 \quad \text{where} \quad \{h = 1, 2, 3...\} \tag{3.37}$$

The eigenfunctions corresponding to these eigenvalues are

$$\Theta_0^q(\theta) = 1 \qquad \text{and} \qquad \Theta_h^q(\theta) = \cos\left(\frac{h\pi}{\eta}\left(\theta - \theta_q\right)\right) \tag{3.38}$$

The general solutions of (3.35) for Λ_0 and Λ_h are:

$$\rho_0^q(r) = A_0^q J_0(\alpha r) + B_0^q Y_0(\alpha r) \tag{3.39}$$

$$\rho_h^q(r) = A_h^q J_{h\pi/\eta}(\alpha r) + B_h^q Y_{h\pi/\eta}(\alpha r) \tag{3.40}$$

where, A_0^q, B_0^q, A_h^q, and B_h^q are complex integration constants. $J_{h\pi/\eta}$ and $Y_{h\pi/\eta}$ are Bessel function of the first and second kind of order $h\pi/\eta$ respectively. The general solution as the combination of these individual solutions is given by:

$$A_b^q(r,\theta) = A_0^q J_0(\alpha r) + B_0^q Y_0(\alpha r) + \sum_{h=1}^{\infty}\left(A_h^q J_{h\pi/\eta}(\alpha r) + B_h^q Y_{h\pi/\eta}(\alpha r)\right)\cdot\cos\left(\frac{h\pi}{\eta}\left(\theta - \theta_q\right)\right) \tag{3.41}$$

The general solution is further simplified using boundary conditions (3.31) and (3.32) and the final expression is given as:

$$A_b^q(r,\theta) = C_0^q\left(\frac{J_0(\alpha r) - G_1 Y_0(\alpha r)}{J_0(\alpha R_r) - G_1 Y_0(\alpha R_r)}\right) + \sum_{h=1}^{\infty} C_h^q \frac{J_{h\pi/\eta}(\alpha r) - G_h Y_{h\pi/\eta}(\alpha r)}{J_{h\pi/\eta}(\alpha R_r) - G_h Y_{h\pi/\eta}(\alpha R_r)}\cdot\cos\left(\frac{h\pi}{\eta}\left(\theta - \theta_q\right)\right) \tag{3.42}$$

Where, C_0^q, C_h^q are new constants with following expressions:

$$G_1 = \frac{J_1(\alpha R_b)}{Y_1(\alpha R_b)} \tag{3.43}$$

$$G_h = \frac{-\alpha J_{1+h\pi/\eta}(\alpha R_b) + \frac{h\pi}{\eta R_b} J_{h\pi/\eta}(\alpha R_b)}{-\alpha Y_{1+h\pi/\eta}(\alpha R_b) + \frac{h\pi}{\eta R_b} Y_{h\pi/\eta}(\alpha R_b)} \tag{3.44}$$

As the potential for inner rotor bars are obtained, similarly potential functions for other regions of DRM are obtained using separation of variable method. The magnetic vector potential for inner and outer air-gap are given by (3.45) and (3.46) respectively.

$$A^{ia}(r,\theta) = A_0^{ia} + \sum_{n=1}^{\infty}\left(A_n^{ia}r^n + B_n^{ia}r^{-n}\right)\cos(n\theta) + \sum_{n=1}^{\infty}\left(C_n^{ia}r^n + D_n^{ia}r^{-n}\right)\sin(n\theta) \quad (3.45)$$

$$A^{oa}(r,\theta) = \sum_{n=1}^{\infty}(A_n^{oa}r^n + B_n^{oa}r^{-n})\cos(n\theta) + \sum_{n=1}^{\infty}(C_n^{oa}r^n + D_n^{oa}r^{-n})\sin(n\theta) \quad (3.46)$$

where, A_0^{ia}, A_n^{ia}, B_n^{ia}, C_n^{ia}, D_n^{ia}, A_n^{oa}, B_n^{oa}, C_n^{oa} and D_n^{oa} are the constants. Magnetic vector potential for PM region, considering the magnetization of PM is given as [47]:

$$A_m(r,\theta) = \sum_{n=1}^{\infty}(A_n^m r^n + B_n^m r^{-n})\cos(n\theta) + \sum_{n=1}^{\infty}(C_n^m r^n + D_n^m r^{-n})\sin(n\theta) + \sum_{n=1}^{\infty}\gamma_n(r)(cos(n(\theta-\delta)) - jsin(n(\theta-\delta))) \quad (3.47)$$

where, A_n^m, B_n^m, C_n^m, D_n^m are constants and

$$\gamma_n(r) = \begin{cases} \frac{\mu_0 n M_{r\nu} r}{(1-n^2)} & \text{if} \quad n = \nu p, \quad n \neq 1 \quad \text{with} \quad \nu = 1,3,5... \\ \frac{\mu_0 M_r r \ln r}{2} & \text{if} \quad n = p = 1 \\ 0 & \text{else} \end{cases}$$

3.3.4.3 Boundary Conditions

In order to determine all the constants in the potential functions for various regions in the previous section, boundary conditions are defined. Each rotor bar on its sides and at its bottom is covered with iron core of infinitely permeability as shown in Fig. 3.1. Thus, the tangential component of the magnetic field at these boundaries is zero and are mathematically given in (3.30) and (3.31). The continuity conditions between the q^{th} rotor bar and inner air-gap result in the following boundary conditions:

$$\left.\frac{\partial A_b^q}{\partial r}\right|_{r=R_r} = \left.\frac{\partial A_{ia}}{\partial r}\right|_{r=R_r} \quad (3.48)$$

$$A_b^q(R_r,\theta) = A_{ia}(R_r,\theta) \quad (3.49)$$

Continuity of tangential component of field intensity and radial component of magnetic field between inner air-gap and magnet region are mathematically expressed as:

$$\left.\frac{\partial A_{ia}}{\partial r}\right|_{r=R_a} = \frac{1}{\mu_m}\left.\frac{\partial A_m}{\partial r}\right|_{r=R_a} \tag{3.50}$$

$$\left.\frac{\partial A_{ia}}{\partial \theta}\right|_{r=R_a} = \left.\frac{\partial A_m}{\partial \theta}\right|_{r=R_a} \tag{3.51}$$

Similarly, the continuity of tangential component of field intensity and radial component of magnetic field between magnet region and outer air-gap region results in the following boundary conditions:

$$\frac{1}{\mu_m}\left.\frac{\partial A_m}{\partial r}\right|_{r=R_m} = \left.\frac{\partial A_{oa}}{\partial r}\right|_{r=R_m} \tag{3.52}$$

$$\left.\frac{\partial A_m}{\partial \theta}\right|_{r=R_m} = \left.\frac{\partial A_{oa}}{\partial \theta}\right|_{r=R_m} \tag{3.53}$$

In the presence of infinitely permeable stator iron, the boundary condition between outer air-gap and current sheet is given as:

$$\left.\frac{\partial A_{oa}}{\partial r}\right|_{r=R_s} = \mu_0 J_m|_{r=R_s} \tag{3.54}$$

In the air-gap regions, the total flux crossing the air-gap must be zero [43]. In case of inner and outer air-gap, this condition leads to the following equations:

$$\int_0^{2\pi} \left.\frac{\partial A_{ia}}{\partial r}\right|_{r=R_r} R_r d\theta = \int_0^{2\pi} \left.\frac{\partial A_{ia}}{\partial r}\right|_{r=R_a} R_a d\theta \tag{3.55}$$

$$\int_0^{2\pi} \left.\frac{\partial A_{oa}}{\partial r}\right|_{r=R_m} R_m d\theta = \int_0^{2\pi} \left.\frac{\partial A_{oa}}{\partial r}\right|_{r=R_s} R_s d\theta \tag{3.56}$$

Further development of these boundary conditions result in set of simultaneous equations, which are solved to obtain the constants of the potential functions. Development of boundary conditions and final equations are presented in the Appendix 8. The final equation in the matrix form is presented in (8.28) in Appendix 8. The number of harmonics considered for truncation are H=5 and N=70. Thus the dimension of the complete matrix A becomes 949x949. The inverse of the matrix was found using Matlab. The radial and tangential components of magnetic field from potential function in any region

of the motor can be obtained using (3.57).

$$B_r^i = \frac{1}{r}\frac{\partial A_i}{\partial \theta}, \quad B_\theta^i = -\frac{\partial A_i}{\partial r} \quad \{i = oa, m, ia, b\} \tag{3.57}$$

3.3.4.4 Inner rotor bar current calculation

The resultant rotating magnetic field due to stator and PM excitation causes induced current in the conducting bars of inner rotor. The magnitude of the induced current depends on the resultant air-gap field as well as rotational speed of the inner rotor (N_{IR}). The induced current density in the q^{th} rotor bar is given by [43]:

$$J_b^q(r,\theta) = -j\omega_{r\nu}\sigma A_b^q(r,\theta) \tag{3.58}$$

Where, A_b^q is the potential for the respective rotor bar. The current can be obtained by integrating the current density over the surface of the bar and is expressed as:

$$I_b^q = \int_{R_b}^{R_r}\int_{\theta_q}^{\theta_q+\eta} J^q(r,\theta)\, r dr d\theta \tag{3.59}$$

Using the expression of potential the expression is simplified to:

$$I_b^q = \frac{-jC_0^q\sigma\omega_{r\nu}\eta}{J_0(\alpha R_r) - G_1 Y_0(\alpha R_r)} \int_{R_b}^{R_r} r\left(J_0(\alpha r) - G_1 Y_0(\alpha r)\right) dr \tag{3.60}$$

Upon further simplification the mathematical relation to compute q^{th} bar current is given by:

$$I_b^q = \frac{jC_0^q\sigma\omega_{r\nu}\eta R_r}{\alpha}\left(\frac{J_1(\alpha R_b)\,Y_1(\alpha R_r) - J_1(\alpha R_r)\,Y_1(\alpha R_b)}{J_0(\alpha R_r)\,Y_1(\alpha R_b) - J_1(\alpha R_b)\,Y_0(\alpha R_r)}\right) \tag{3.61}$$

3.3.4.5 Electromagnetic torque calculation

Radial and tangential components of air-gap magnetic fields are employed to find the electromagnetic torque using Maxwell stress tensor method. In order to calculate torque with Maxwell stress tensor for 2-D cylindrical geometries, a circle enclosing the moving objects in the air-gap is taken as the integration path. The electromagnetic torque calculation using stress tensor is given as:

$$T_{em} = \frac{L_m r^2}{2\mu_0}\int_0^{2\pi} \mathrm{Re}\left\{B_r(r,\theta)\cdot B_\theta^*(r,\theta)\right\} d\theta \tag{3.62}$$

Where, r is the radius of the circle taken as integration path in the air-gap and $*$ is the complex conjugate notation. Torque presented in (3.62) is applicable for one one harmonic at a time. In case the magnetic field B_r and B_θ have many harmonic component then all must be computed individually and then added together to find total torque.

Considering the geometry of the DRM, there are two air-gaps and hence torque needs to be calculated in both the air-gaps. In (3.62), general expression for calculating electromagnetic torque using maxwell stress tensor method is presented and is represented by T_{em}. As in case of DRM two torques will be produced by both the rotors, in order to differentiate them superscripts have been used. Thus, T_{em}^{ir} and T_{em}^{or} represents torques produced by inner and outer rotors respectively. It is to be noted that Maxwell stress tensor calculates total torque produced by the moving object inside its integration path. Thus, the torque calculated in outer air-gap using (3.62) also includes the torque produced by inner rotor and thus it has been represented by total torque T_{em}^{T} (total torque i.e. sum of both inner and outer rotor). Now to separately find the torque of outer rotor (T_{em}^{or}), the inner rotor torque (T_{em}^{ir}) is subtracted from the total torque (T_{em}^{T}) as given in (3.63). The inner and total torque radii have been mentioned to indicate where the torques have been calculated. Since the inner rotor torque has been calculated at $r = R_{ir}$, it has been represented as $T_{em}^{ir}\big|_{r=R_{ir}}$. Similarly, the total torque T_{em}^{T} is calculated at $r = R_{or}$, its has been represented as $T_{em}^{T}\big|_{r=R_{or}}$.

$$T_{em}^{or} = T_{em}^{T}\big|_{r=R_{or}} - T_{em}^{ir}\big|_{r=R_{ir}} \tag{3.63}$$

3.4 Results and Discussion

Validation of the analytical model proposed in Section 3.3 is presented here. Results obtained from analytical model are compared with those from the FEA. FEA is performed using Ansys Maxwell 14.0.0. The remaining setting for the FEA analysis are same as explained in Section 2.5. Internal algorithms of Maxwell has been used for meshing and torque calculation. Fig. 3.7 shows the FEA model for the DRM considered for analysis. Important parameters required for FEA and analytical model are given in Table 3.2.

In order to use the analytical model for radial magnetization, computation is done for each harmonic (ν) of magnetization separately and the final result is obtained with addition of results due to

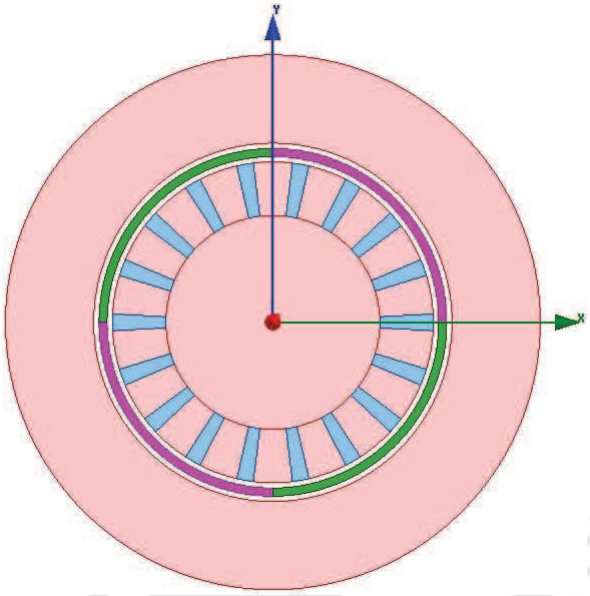

Figure 3.7: FEA model of analyzed DRM.

each respective harmonic. Thus, computation of any performance parameter (magnetic field, rotor bar current, electromagnetic torque) involves evaluation of analytical model for all current density and PM magnetization harmonics. For example, the calculation of torque in inner air-gap due to both current and magnet is done with following expression:

$$\underbrace{T_{em}^{ir}}_{\text{Total torque}} = \underbrace{T_{em}^{ir}\big|_{\nu=1}}_{\text{From Current}} + \underbrace{\sum_{\nu=1,3,5...} T_{em}^{ir}}_{\text{From PM}} \tag{3.64}$$

For current excitation one harmonic and for PM excitation 31 harmonics have been considered.

The operation of the DRM depends on both initial angle of outer rotor (δ) and inner rotor speed (N_{IR}). In order to validate the developed analytical model, results at different δ and N_{IR} values have been presented in comparison with those from FEA. Fig. 3.8 and 3.10 shows the radial and tangential components of magnetic fields in inner and outer air-gap respectively for $\delta = 15°$ and $N_{IR} = 500$ rpm. Fig. 3.9 presents the induced bar currents in inner rotor. It can be easily observed that all the analytical results closely match with the results from FEA, validating the developed analytical model. However, a slight mismatch in the tangential component of outer air-gap magnetic field (Fig. 3.10(b)) is observed. This is due to the flux concentration near the pole ends which is difficult to model analytically. The same set of results for $\delta = 45°$ and $N_{IR} = 0$ rpm are presented in Fig. 3.11 - 3.13.

Table 3.2: Specification of the DRM motor

Parameter	Value	Unit
Stator inner radius (R_s)	67.00	mm
PM rotor outer radius (R_m)	65.00	mm
PM rotor inner radius (R_a)	62.00	mm
Cage rotor outer radius (R_r)	60.00	mm
Inner radius of cage rotor bar (R_b)	40.00	mm
Motor length (L_m)	1	m
Cage rotor bar number (Q)	18	
Pole pairs (p)	2	
Supply frequency (f)	50	Hz
PM remanent flux density (B_r)	1.20	T
Rotational speed of PM rotor (N_{OR})	1500	rpm
Inner rotor slot opening (η)	6	degrees
Relative permeability of PM (μ_m)	1.05	
Electrical conductivity of inner rotor bar (σ)	$35{\cdot}10^6$	S/m
Peak value of the ν^{th} harmonic component of current sheet (J_{max})	$8{\cdot}10^4$	A/m
Total number of harmonics for inner, outer air-gap and PM region (N)	70	
Total number of harmonics for bar region in cage rotor (H)	5	
Radius of integration path in inner air-gap (R_{ir})	61	mm
Radius of integration path in outer air-gap (R_{or})	66	mm
Magnet fraction (α_m)	1	

As discussed in Section 3.3.4.5, presence of inner and outer rotor leads to production of T_{em}^{ir} and T_{em}^{or}. Analytically, the torques are calculated using Maxwell stress tensor as given in (3.62) and (3.63). T_{em}^{ir} and T_{em}^{or} depends on δ and N_{IR}. Therefore, the torques are analyzed for varying δ and N_{IR}, where if one parameter is varying then the other is kept constant. Fig. 3.14 shows the variation of inner and

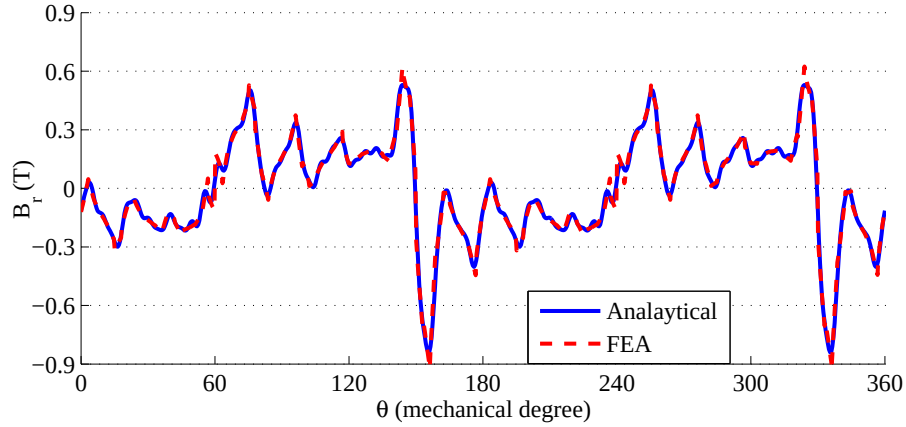

(a)

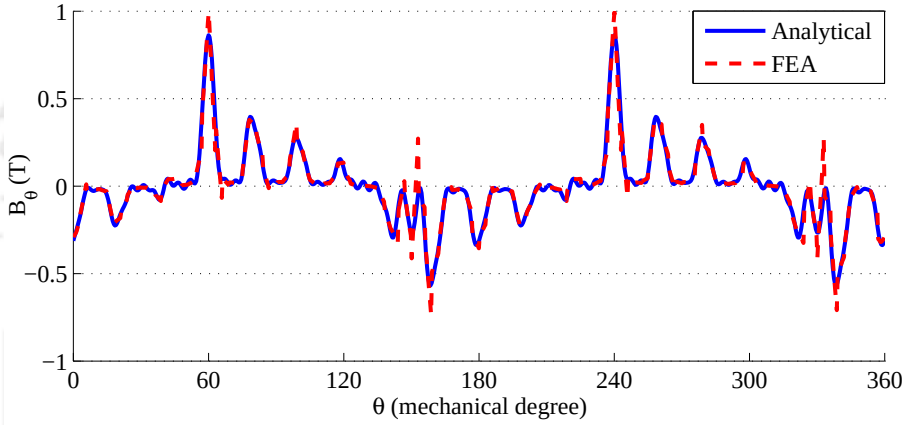

(b)

Figure 3.8: Inner air-gap magnetic field distribution at $r = R_{ir}$ with $\delta = 15^\circ$ and $N_{IR} = 500$ rpm (a) radial component (b) tangential component.

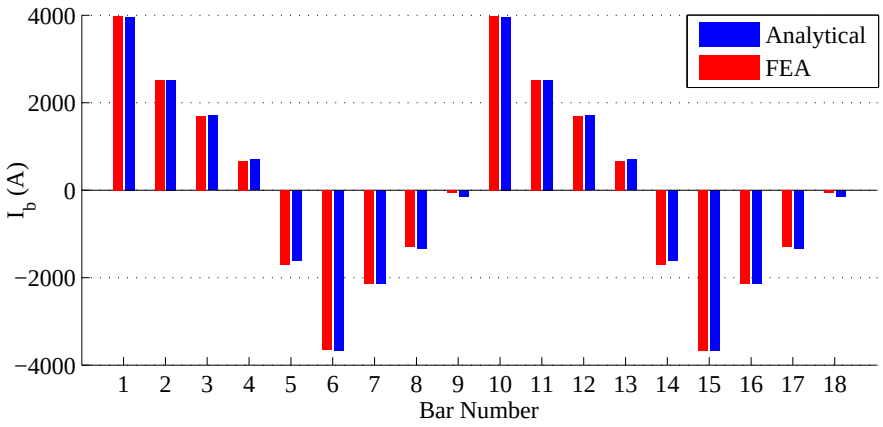

Figure 3.9: Currents in rotor bars at $\delta = 15^\circ$ and $N_{IR} = 500$ rpm.

outer rotor torque with respect to δ at $N_{IR} = 750$ rpm. It can be observed that the variation of torque is similar to PM motor. Variation of torques with respect to N_{IR} at $\delta = 30^\circ$ is presented in Fig. 3.15. It is

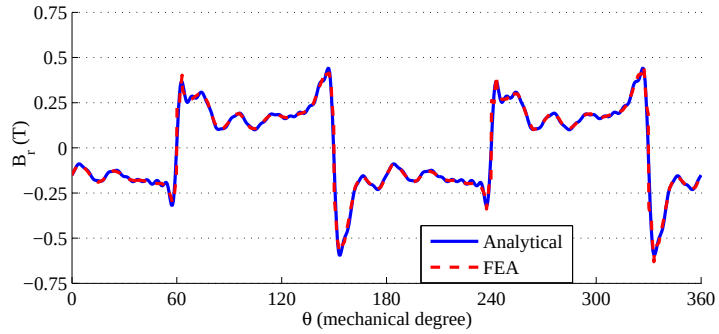

(a)

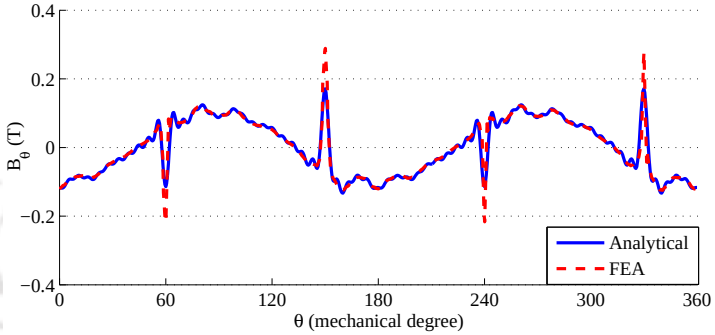

(b)

Figure 3.10: Outer air-gap magnetic field distribution at $r = R_{or}$ with $\delta = 15°$ and $N_{IR} = 500$ rpm (a) radial component (b) tangential component.

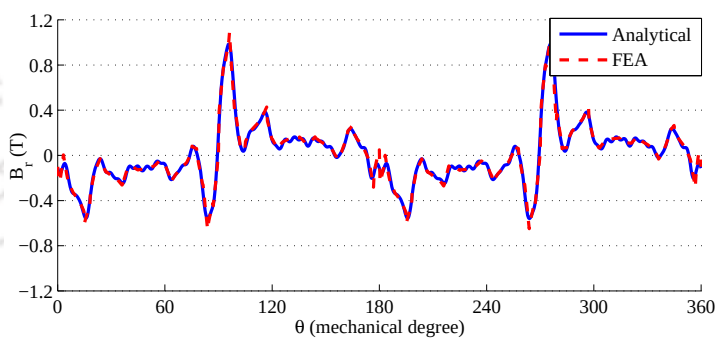

(a)

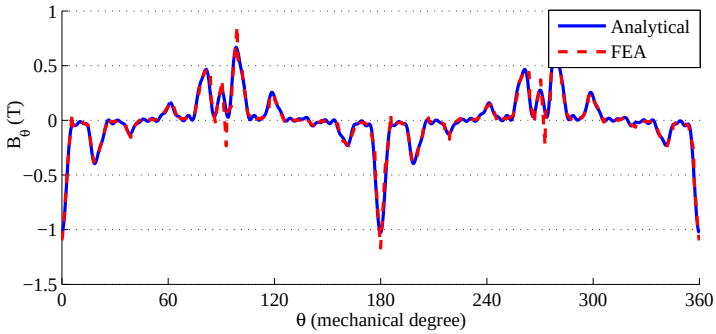

(b)

Figure 3.11: Inner air-gap magnetic field distribution at $r = R_{ir}$ with $\delta = 45°$ and $N_{IR} = 0$ rpm (a) radial component (b) tangential component.

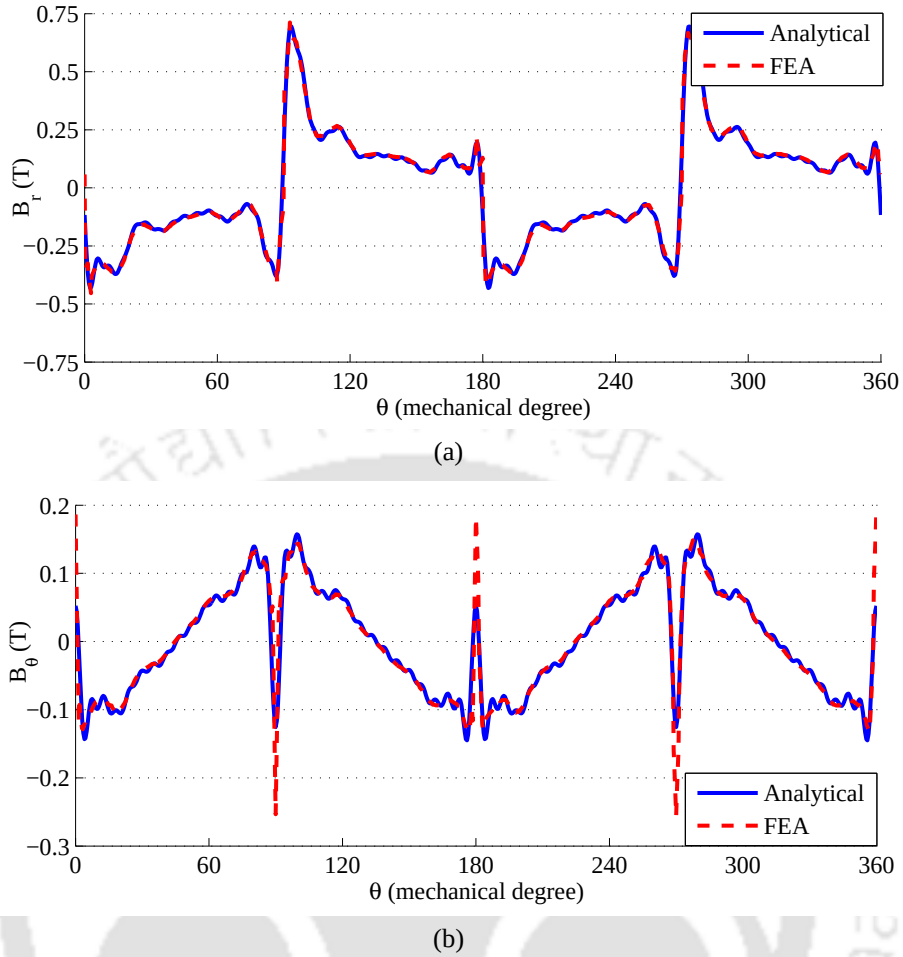

Figure 3.12: Outer air-gap magnetic field distribution at $r = R_{or}$ with $\delta = 45°$ and $N_{IR} = 0$ rpm (a) radial component (b) tangential component.

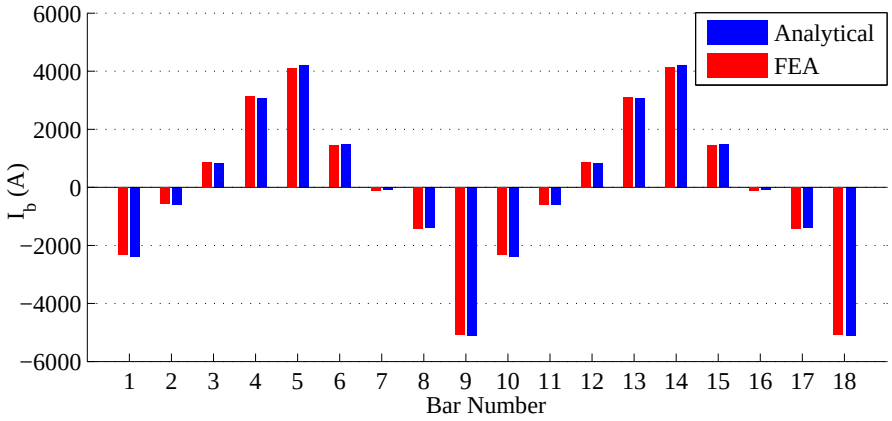

Figure 3.13: Currents in rotor bars at $\delta = 45°$ and $N_{IR} = 0$ rpm.

noted that unlike an IM and synchronous motor, DRM is able to produce torque at both synchronous and non-synchronous speed.

Fig. 3.16 presents output powers for inner rotor (P^{ir}), outer rotor (P^{or}) and total output power (P^T)

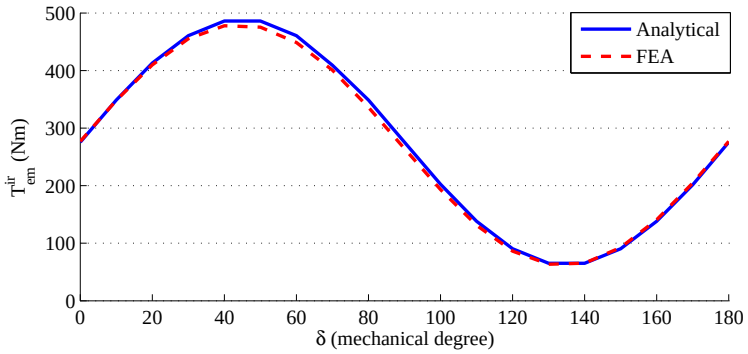

(a)

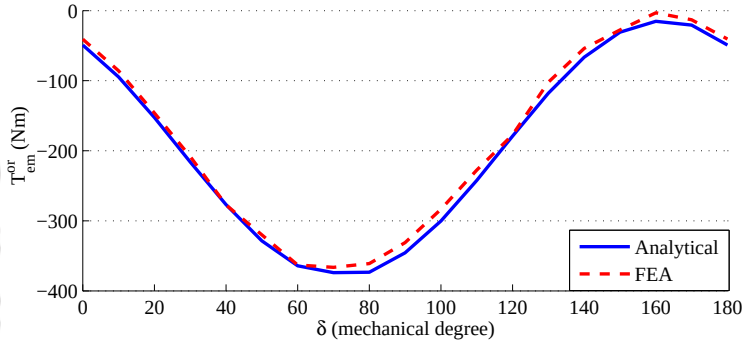

(b)

Figure 3.14: Variation of torques with respect to δ at N_{IR} = 750 rpm (a) inner rotor (b) outer rotor.

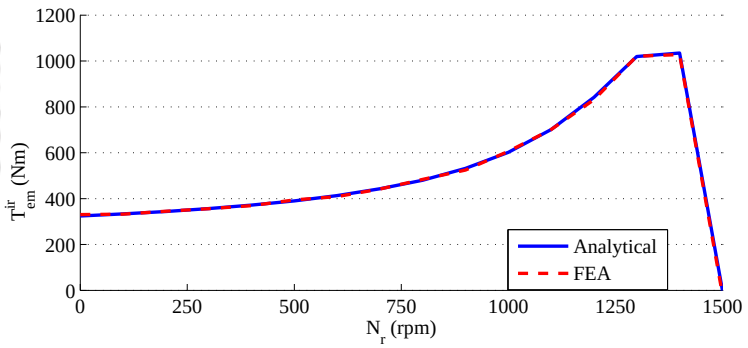

(a)

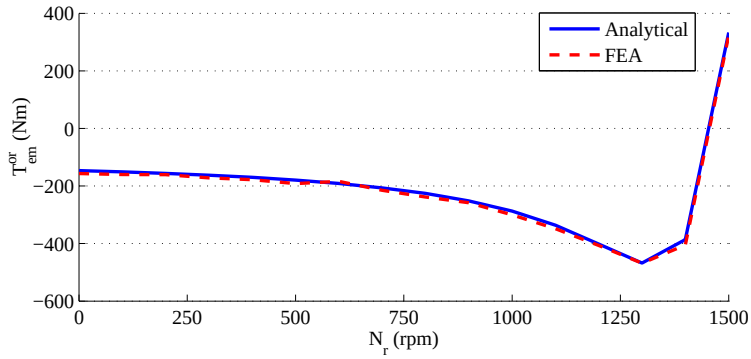

(b)

Figure 3.15: Variation of torques with respect to N_{IR} at $\delta = 30°$ (a) inner rotor (b) outer rotor.

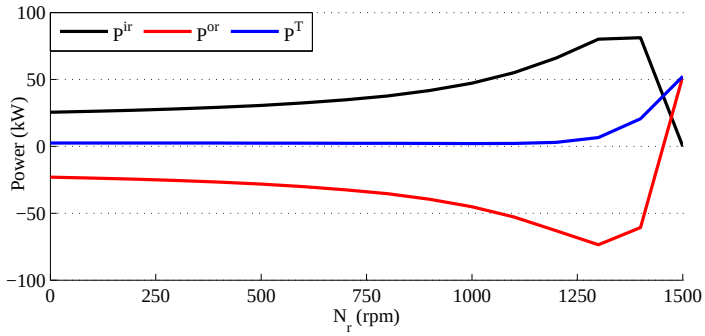

Figure 3.16: Variation of output powers with respect to Nr at $\delta = 30°$.

w.r.t N_r at $\delta = 30°$. It can be observed that in very small region P^T is positive. Thus, from the figure, it can be observed that operating point for DRM must be chosen such that output power of both the rotors are positive.

3.5 Summary and Conclusion

In this chapter, an analytical model for hybrid IM-PM DRM is presented. The model is useful for quick analysis of the complex motor. Analytical model can be used to compute air-gap magnetic field in both the air-gaps. Electromagnetic torques produced by both the rotors can also be calculated accurately using the analytical model. Results for radial and tangential magnetic fields, inner rotor bar induced currents and torques due to both the rotors have been presented for various operating conditions of the motor. All the results match closely with the results obtained from FEA.

4

Steady State Model for DRM

Contents

4.1 Introduction

A steady state model (SSM) of any motor helps in understanding its operation, steady state performance characteristics, and an electrical representation for the magnetic field interaction between the motor parts [39]. During the design stage of a motor which is an iterative process [40], the motor performance can be checked from SSM which gives a much faster results as compared to precise but time consuming FEA. The novelty of this work lies in the development of a steady state model for a DRM that comprises an electrical equivalent circuit (EEC) and performance equations. EEC is developed by deriving the voltage equation and performance of the motor is evaluated from the torque equation derived. The SSM is obtained starting with definition of motor inductances, winding flux linkages and lastly applying the electromechanical energy conversion principles in DRM. For validating the results of the DRM model developed, comparison is made with those obtained from the FEA.

4.2 Development of Steady State Model of DRM

The steady state model of analyzed hybrid IM-PM DRM comprising the EEC and the torque equation is developed in this section. The voltage equation is used to develop the EEC. The voltage equation is derived using the flux linkage equations for each of the motor windings. Further, the torque equation is developed using the energy conversion principles and co-energy. With the motor model developed, the operation of the motor can be understood and important steady state characteristics can be quickly obtained.

All rotating electrical motors have a common feature that they use magnetic field for energy conversion, where a coupling field interacts between the electrical and mechanical systems for the energy conversion [48]. The geometrical and electrical symmetries in DRM are exploited in developing the model. To further facilitate the development of the SSM, the following assumptions are made in this work:

- Magnetization curve of stator and inner rotor core is assumed to be linear.
- The supply voltage is considered free from harmonics.
- The motor has smooth air-gaps.

- Motor cores are considered to be loss free.

4.2.1 Development of Electrical Equivalent Circuit for DRM

The per-phase EEC of any electrical motor is basically the circuit representation of its per-phase voltage and current equations. EEC can be easily drawn from the careful observation of terms present in these equations. Hence, the objective is to find the per-phase voltage equation in terms of known motor parameters. However, it is to be noted that EEC is only applicable for fundamental components of excitation and thus current, torque obtained from EEC also corresponds to fundamental components. In case the practical excitation is not sinusoidal in nature, equivalent fundamental components may be used for analysis.

The stator of DRM is considered to be voltage excited from a three-phase source. The stator per-phase voltage equation in the general form is given by (4.1), the steady state form of the same is given by (4.2). While deriving the stator phase-*a* voltage equation, the stator phase-*a* flux linkage is required. In DRM, each phase winding of stator and inner rotor is linked by fluxes of other windings in the motor as well as flux due to permanent magnet. Thus, the stator phase-*a* flux linkage is given as (4.3).

$$v_{as} = i_{as}R_s + \frac{d\lambda_{as}}{dt} \tag{4.1}$$

$$V_{as} = I_{as}R_s + j\omega_{st}\Lambda_{as} \tag{4.2}$$

$$\begin{aligned}\lambda_{as} = {} & L_s i_{as} + M_{as\_bs} i_{bs} + M_{as\_cs} i_{cs} + M_{as\_ar} i_{ar} \\ & + M_{as\_br} i_{br} + M_{as\_cr} i_{cr} + \phi_{max\_s} \cos\left(\theta_{st\_pm}\right)\end{aligned} \tag{4.3}$$

In order to frame these flux linkage equations, winding inductances of various motor parts needs to be defined. Thus, the voltage equation and hence the EEC of DRM is developed using a set of steps, starting with defining the various motor inductances as described successively.

Step V1: The stator coils and inner rotor bars can be represented as three-phase systems having self and mutual inductances. The outer rotor is made from permanent magnets and does not have any coils thus, it does not have any inductance associated with it. To facilitate the understanding of winding arrangement in different parts of DRM and their respective mutual inductances Fig. 4.1 shows lumped representation of stator and inner rotor windings.

It is a conventional practice in machine analysis to assume electrical linearity, i.e. no saturation

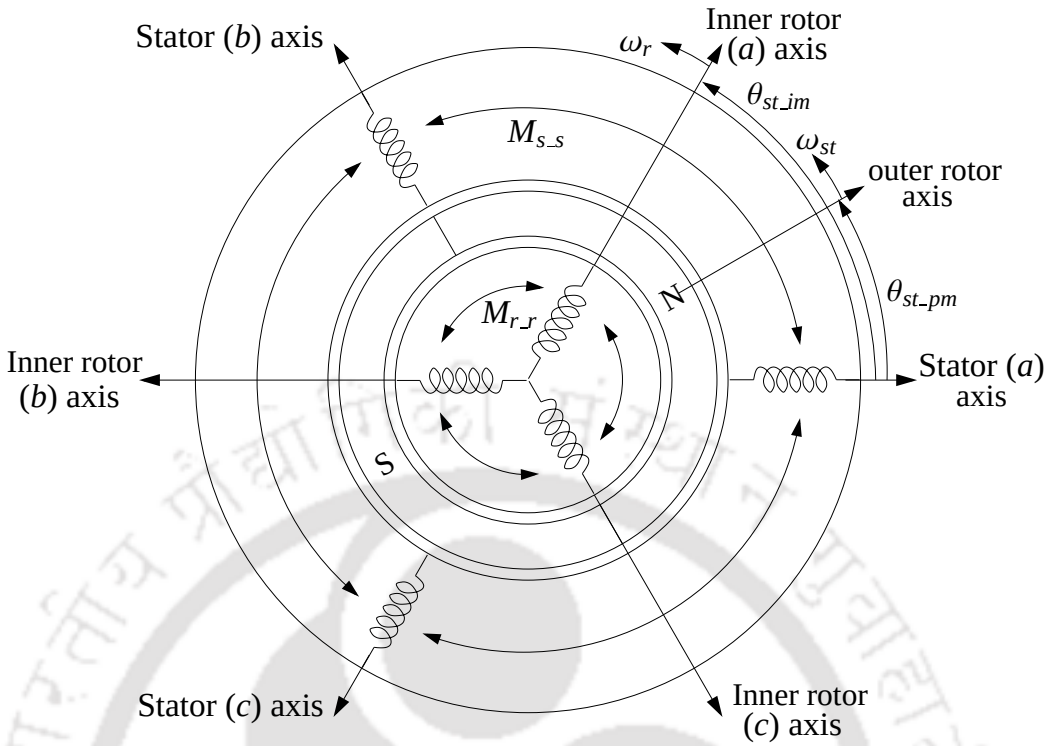

Figure 4.1: Lumped representation of stator and inner rotor windings with outer and inner rotor positions w.r.t. stator.

in stator or rotor magnetic material. Since, DRM considered is having smooth air-gaps as a result the field produced by each DRM part is unaffected by rotor position. Therefore, all the self-inductances, mutual inductances between the stator phases, and the mutual inductances between the inner rotor phases remain independent of rotor position. Whereas, mutual inductances between stator and inner rotor phases are function of inner rotor position (θ_{st_im}). Mutual inductance of a stator phase w.r.t. inner rotor phase is maximum (M_{max_sr}) when they are aligned with each other. Mutual inductances of stator phase-*a* w.r.t. three phases of inner rotor or vice versa is given by (4.4).

$$\begin{aligned} M_{as\_ar} &= M_{ar\_as} = M_{max\_sr}\cos\left(\theta_{st\_im}\right) \\ M_{as\_br} &= M_{br\_as} = M_{max\_sr}\cos\left(\theta_{st\_im} + \tfrac{2\pi}{3}\right) \\ M_{as\_cr} &= M_{cr\_as} = M_{max\_sr}\cos\left(\theta_{st\_im} - \tfrac{2\pi}{3}\right) \end{aligned} \tag{4.4}$$

In a similar manner the mutual inductances of stator phase-*b* and phase-*c* w.r.t. three phases of inner rotor can also be framed with proper consideration of angles existing between them as shown in Fig. 4.1. Mutual inductances between the stator phase windings that are independent of rotor position are

given by (4.5).

$$M_{as\_bs} = M_{as\_cs} = M_{bs\_as} = M_{bs\_cs} = M_{cs\_bs} = M_{cs\_as} = M_{s\_s} \tag{4.5}$$

Similarly, mutual inductance between the inner rotor phases is given by (4.6).

$$M_{ar\_br} = M_{ar\_cr} = M_{br\_ar} = M_{br\_cr} = M_{cr\_ar} = M_{cr\_br} = M_{r\_r} \tag{4.6}$$

Step V2: The DRM has three motor parts out of which two are the rotating members. Based on the operating speeds of these rotors, the relations defining the position of three motor parts w.r.t. each other are given in (4.7)-(4.9). Fig. 4.2 explains the angles associated with different fields present in the motor. The fields of the stator (φ_s) and outer rotor (φ_{pm}) are at an initial angle of δ_{st_pm}. The inner rotor mainly sees the field of the outer rotor and therefore its induced emf (E_r) lags the field inducing it by $\frac{\pi}{2}$ radians. The inner rotor current and field (φ_{im}) produced by it lags E_r by its power factor angle (β). All these angles are in electrical radians. Physical representations of these rotor positions are shown in Fig. 4.1.

$$\theta_{st\_im} = \omega_r t + \delta_{st\_im} \tag{4.7}$$

$$\theta_{pm\_im} = (\omega_{st} - \omega_r)\, t + \delta_{pm\_im} \tag{4.8}$$

$$\theta_{st\_pm} = \omega_{st} t + \delta_{st\_pm} \tag{4.9}$$

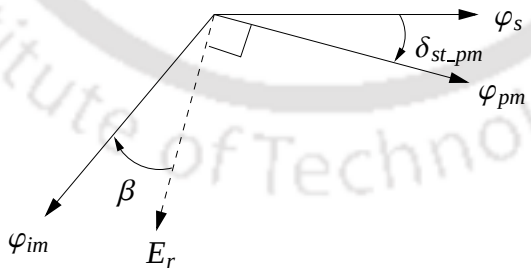

Figure 4.2: Relationship amongst the different initial shift angles in DRM.

Step V3: Having defined the various inductances appearing in (4.3), the other quantities that remains to be defined are stator and inner rotor currents. The stator is energized with three-phase

balanced supply, therefore the resulting currents in the stator phases are defined by (4.10).

$$\begin{aligned} i_{as} &= I_{max\_s}\cos(\omega_{st}t) \\ i_{bs} &= I_{max\_s}\cos\left(\omega_{st}t - \tfrac{2\pi}{3}\right) \\ i_{cs} &= I_{max\_s}\cos\left(\omega_{st}t - \tfrac{4\pi}{3}\right) \end{aligned} \tag{4.10}$$

Step V4: In (4.3) the inner rotor currents also appear which needs to be determined in terms of stator currents given in (4.10). For this, using the fact that inner rotor terminals are short circuited in an IM type rotor, the voltage equation for phase-*a* of inner rotor is given by (4.11). Since, the induced voltages and currents in inner rotor are at slip frequency as in case of an IM, the steady state form of the voltage equation is given by (4.12).

$$v_{ar} = i_{ar}R_r + \frac{d\lambda_{ar}}{dt} = 0 \tag{4.11}$$

$$V_{ar} = I_{ar}R_r + j(\omega_{st} - \omega_r)\Lambda_{ar} = 0 \tag{4.12}$$

The flux linkage for each phase of inner rotor in (4.12) can be determined in the same way as done for the stator phase in (4.3) and is given in (4.13).

$$\begin{aligned} \lambda_{ar} = {} & L_r i_{ar} + M_{ar\_br}i_{br} + M_{ar\_cr}i_{cr} + M_{ar\_as}i_{as} \\ & + M_{ar\_bs}i_{bs} + M_{ar\_cs}i_{cs} + \phi_{max\_r}\cos\left(\theta_{pm\_im}\right) \end{aligned} \tag{4.13}$$

Similarly, voltage equations can be written for the other two phases of inner rotor. Solving this set of voltage equations for inner rotor currents gives us the result for an inner rotor phase current in terms of stator current as given in (4.14) for phase-*a*. In (4.14) self and mutual inductances of inner rotor phases are written in terms of leakage inductances and are related by (4.15).

$$i_{ar} = \frac{\frac{3}{2}(\omega_{st} - \omega_r)\left[\begin{array}{l} \frac{2}{3}\phi_{max\_r}\cos\left(\xi + \delta_{pm\_im}\right) \\ \\ + M_{max\_sr}I_{max\_s}\cos(\xi + \delta_{st\_im}) \end{array}\right]}{\sqrt{R_r^2 + L_{rr}^2(\omega_{st} - \omega_r)^2}} \tag{4.14}$$

where,

$$\xi = (\omega_{st} - \omega_r)t - \frac{\pi}{2} + \tan^{-1}\left(\frac{(\omega_{st} - \omega_r)L_{rr}}{R_r}\right)$$

$$L_{rr} = L_r - M_{r\_r} \tag{4.15}$$

Step V5: Substituting the quantities obtained in (4.3)-(4.14) in (4.2) and its subsequent mathematical simplification results in the per-phase stator voltage equation for phase-*a*. Using the mutual inductance relationship between three-phase and single-phase system defined as (4.16), phase-*a* voltage equation is given by (4.17).

$$M_{max\_sr\_ph} = \frac{3}{2} M_{max\_sr} \tag{4.16}$$

$$\begin{aligned} v_{as} &= R_s I_{max\_s} \cos(\omega_{st} t) + \omega_{st} L_{ss} I_{max\_s} \cos\left(\omega_{st} t + \tfrac{\pi}{2}\right) \\ &\quad + \omega_{st} \phi_{max\_s} \cos\left(\omega_{st} t + \delta_{st\_pm} + \frac{\pi}{2}\right) \\ &\quad + \frac{\left(\begin{array}{c} \omega_{st} \cos\left(\omega_{st} t + \delta_{pm\_im} + \delta_{st\_im} - \varepsilon\right) \\ \cdot M_{max\_sr\_ph} \left(-\omega_{st} t + \omega_r\right) \phi_{max\_r} \end{array}\right)}{\sqrt{R_r^2 + (\omega_{st} - \omega_r)^2 L_{rr}^2}} \\ &\quad + \frac{\omega_{st} M_{max\_sr\_ph}^2 I_{max\_s} \cos(\omega_{st} t - \varepsilon)(-\omega_{st} t + \omega_r)}{\sqrt{R_r^2 + (\omega_{st} - \omega_r)^2 L_{rr}^2}} \end{aligned} \tag{4.17}$$

Stator voltage equation (4.17) is simplified and converted to the phasor form as given in (4.18). All the excitation terms (v_{as}, I_{max_s}, ϕ_{max_s}, ϕ_{max_r}) have been replaced with their rms equivalents (V_s, I_s, ϕ_s, ϕ_r).

$$V_s = I_s R_s + j I_s \omega_{st} L_{ss} + \frac{I_s e^{-j\varepsilon} s \omega_{st}^2 M_{max\_sr\_ph}^2}{\sqrt{R_r^2 + s^2 \omega_{st}^2 L_{rr}^2}} + V_1 + V_2 \tag{4.18}$$

where,

$$V_1 = V_{1max} \angle \left(\delta_{st\_pm} + \frac{\pi}{2}\right), \quad V_{1max} = \omega_{st} \phi_s \sqrt{2}$$

$$\varepsilon = \tan^{-1}\left[\frac{(\omega_{st} - \omega_r) L_{rr}}{R_r}\right], V_2 = V_{2max} \angle \left(\delta_{pm\_im} + \delta_{st\_im} - \varepsilon\right)$$

$$V_{2max} = \frac{\omega_{st}^2 s M_{max\_sr\_ph} \phi_r \sqrt{2}}{\sqrt{R_r^2 + s^2 \omega_{st}^2 L_{rr}^2}}, \quad s = \frac{(\omega_{st} - \omega_r)}{\omega_{st}}$$

Step V6: The first three terms in the voltage equation (4.18) appears as voltage drop across passive elements as they contain stator current (I_s). Whereas, the last two terms do not contain I_s and can be treated as voltage sources in the EEC for DRM. The terms with I_s in (4.18) are similar to that of an IM voltage equation and the remaining two terms (V_1 & V_2) appear as the back emf in stator and

inner rotor due to permanent magnets in outer rotor. The first two terms of this equation represent the voltage drop in the stator and the last term represents the voltage drop across parallel combination of inner rotor and magnetizing branch similar to that of an IM. The expanded form of voltage equation in (4.18) is given in (4.19). Based on the discussion and the expanded form of voltage expression, the circuit representation of stator voltage equation (4.18) is shown in Fig. 4.3.

$$V_s = I_s R_s + jI_s\omega_{st}\left(L_{ss} - M_{max\_sr\_ph}\right) + V_1 + V_2$$
$$+I_s \cdot \frac{\left(j\omega_{st}\left(L_{rr} - M_{max\_sr\_ph}\right) + \frac{R_r}{s}\right)\cdot\left(j\omega_{st} M_{max\_sr\_ph}\right)}{\left(j\omega_{st}\left(L_{rr} - M_{max\_sr\_ph}\right) + \frac{R_r}{s}\right) + \left(j\omega_{st} M_{max\_sr\_ph}\right)} \quad (4.19)$$

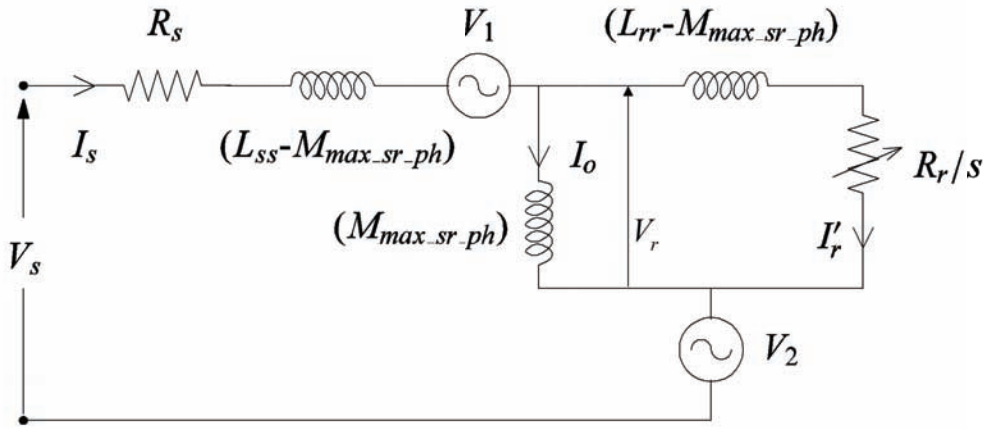

Figure 4.3: Electrical equivalent circuit of hybrid IM-PM DRM.

The EEC formed gives a quick and easy understanding of the DRM operation. Since the DRM considered in this work is a hybrid IM-PM DRM, the EEC formed for DRM resembles with that of an IM. The addition of outer permanent magnet rotor brings the change in the motor operation and its performance as compared to a normal IM. The magnets in outer rotor interact with both the stator and the inner rotor, which is represented by V_1 and V_2 in EEC. Having derived the per-phase stator voltage equation the phasor diagram of the DRM is drawn and is shown in Fig. 4.4.

In order to realize the derived voltage equation for practical cases, the relationship amongst the various angles appearing in (4.17) can be understood with the help of Fig. 4.2 and relations (4.7)-(4.9). In reference with Fig. 4.2, following relations can be obtained.

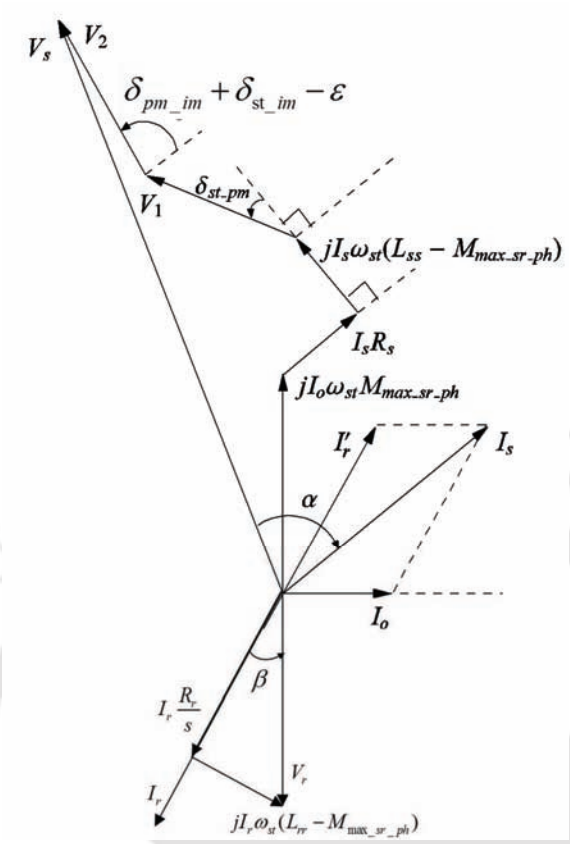

Figure 4.4: On load phasor diagram of hybrid IM-PM DRM.

$$\beta = \tan^{-1}\left(\frac{\omega_{st}\left(L_{rr} - M_{max\_sr\_ph}\right)}{\frac{R_r}{s}}\right) \tag{4.20}$$

$$\delta_{st\_im} = \delta_{st\_pm} - \delta_{pm\_im} \tag{4.21}$$

The complex form of the stator voltage equation (4.18) is used to get the stator current in complex form. The amplitude of thus obtained stator current is the maximum value (I_{max_s}) and its argument is the lag angle (α).

The voltage equation and hence EEC has been developed in this section. The next part of the work describes the development of the most important performance equation of DRM i.e. its torque equation. The stator voltage equation developed is solved for the stator current to be used in determining the torque expression for DRM.

4.2.2 Derivation of Torque Equation for DRM

Electromagnetic torque is developed in a rotating system if its magnetic field is affected by a differential rotation of the rotating part, with the other part remaining stationary. The torque expression of DRM is developed using the electromechanical energy conversion principles, specifically using the co-energy. The hybrid IM-PM DRM considered in this work is conceptualized as two concentric motors having two torque producing ports. As discussed earlier, a common working flux links all the three parts of DRM and is responsible for producing torque in both the air-gaps. Therefore, the torque in these two air-gaps are not independent of each other. The torque expression developed in this section represents the overall torque of DRM i.e. the torque expression gives a combined torque of both outer and inner rotor. The torque for any rotating system is obtained using co-energy as given in (4.22), where θ_{rotor} represents the rotational displacement of the rotating part of the considered rotating system.

The co-energy in (4.22) is determined using (4.23), where λ_{xs} & λ_{xr} are the flux linkages in stator and inner rotor and i_{xs} & i_{xr} are the currents in each winding of stator and inner rotor respectively.

$$T = \frac{d}{d\theta_{rotor}}\left(W_{co\_fld}\right) \tag{4.22}$$

$$W_{co\_fld} = \sum \lambda_{xs} i_{xs} + \sum \lambda_{xr} i_{xr} - W_{fld} \tag{4.23}$$

For the analyzed DRM, the three phases of both stator and inner rotor, result in sets of six flux linkages and six currents equations. Considering this the co-energy for DRM is given by (4.24).

$$\begin{aligned} W_{co\_fld} = {} & \lambda_{as} i_{as} + \lambda_{bs} i_{bs} + \lambda_{cs} i_{cs} + \lambda_{ar} i_{ar} \\ & + \lambda_{br} i_{br} + \lambda_{cr} i_{cr} - W_{fld} \end{aligned} \tag{4.24}$$

Thus, in order to obtain torque expression for DRM, flux linkages, stator currents, inner rotor currents and W_{fld} need to be determined in terms of known motor parameters. The development of the torque expression is carried out following a sequence of steps as explained.

Step T1: The stator and inner rotor flux linkages required in (4.24) are same as defined in (4.3) and (4.13) in Section 4.2.1 respectively. Similarly the flux linkage equations for the other phases of stator and inner rotor can also be framed.

Step T2: The flux linkages defined in the previous step are in terms of various self and mutual inductances associated with stator and inner rotor. Definition of these inductances are same as described in ***Step V1*** of Section 4.2.1.

Step T3: The magnetic field energy stored in an electromagnetic system having current (i) and flux linkage (λ) is given by (4.25).

$$W_{fld} = \int_0^{\lambda_f} i d\lambda \tag{4.25}$$

The magnetic field energy stored in DRM is obtained as the integration of motor phase current w.r.t. corresponding flux linkage, with proper path of integration as given in (4.26).

$$\begin{aligned} W_{fld} = &\left[\int_0^{\lambda_{asf}} i_{as} d\lambda_{as}\right]_{x_1} + \left[\int_0^{\lambda_{bsf}} i_{bs} d\lambda_{bs}\right]_{x_2} \\ &+ \left[\int_0^{\lambda_{csf}} i_{cs} d\lambda_{cs}\right]_{x_3} + \left[\int_0^{\lambda_{arf}} i_{ar} d\lambda_{ar}\right]_{x_4} \\ &+ \left[\int_0^{\lambda_{brf}} i_{br} d\lambda_{br}\right]_{x_5} + \left[\int_0^{\lambda_{crf}} i_{cr} d\lambda_{cr}\right]_{x_6} \end{aligned} \tag{4.26}$$

where,

$$x_1 \equiv (\lambda_{cr} = \lambda_{br} = \lambda_{ar} = \lambda_{cs} = \lambda_{bs} = 0)$$

$$x_2 \equiv (\lambda_{cr} = \lambda_{br} = \lambda_{ar} = \lambda_{cs} = 0, \lambda_{as} = \lambda_{asf})$$

$$x_3 \equiv (\lambda_{cr} = \lambda_{br} = \lambda_{ar} = 0, \lambda_{as} = \lambda_{asf}, \lambda_{bs} = \lambda_{bsf})$$

$$x_4 \equiv (\lambda_{cr} = \lambda_{br} = 0, \lambda_{as} = \lambda_{asf}, \lambda_{bs} = \lambda_{bsf}, \lambda_{cs} = \lambda_{csf})$$

$$x_5 \equiv (\lambda_{cr} = 0, \lambda_{ar} = \lambda_{arf}, \lambda_{as} = \lambda_{asf}, \lambda_{bs} = \lambda_{bsf}, \lambda_{cs} = \lambda_{csf})$$

$$x_6 \equiv (\lambda_{br} = \lambda_{brf}, \lambda_{ar} = \lambda_{arf}, \lambda_{as} = \lambda_{asf}, \lambda_{bs} = \lambda_{bsf}, \lambda_{cs} = \lambda_{csf})$$

With proper inductance relations defined in the previous step, we get a set of six flux linkage equations. To determine the magnetic field energy stored in the motor, the set of flux linkage equations are solved for stator and inner rotor currents in terms of flux linkages to be used in (4.26). The proper path of integration used in (4.26) is explained in Appendix 9 with an example of system having three windings.

Step T4: Co-energy expression developed following the previous three steps in sequence is further

used to obtain the torque expression as given in (4.22). However, in case of the DRM considered in this work there are three relations governing the rotor positions as explained in ***step V2*** of Section 4.2.1. In such systems having multiple moving parts, the co-energy needs to be differentiated partially w.r.t. position of each moving part [48]. Thus, in order to derive torque expression for the considered DRM, co-energy obtained is differentiated w.r.t. θ_{st_im} and θ_{st_pm} as given in (4.27). This gives torque produced by outer as well as inner rotor and thus represents the overall torque of DRM as presented in (3.66).

$$T = \frac{\partial}{\partial \theta_{st\_im}}\left(W_{co\_fld}\right) + \frac{\partial}{\partial \theta_{st\_pm}}\left(W_{co\_fld}\right) \tag{4.27}$$

Step T5: The torque equation obtained using (4.27) is in terms of stator and inner rotor currents, both these currents needs to be determined. The stator currents are defined as given in (4.28). Here, I_{max_s} and α are determined from the voltage equation developed in the Section 4.2.1.

$$\begin{aligned} i_{as} &= I_{max\_s}\cos\left(\omega_{st}t + \alpha\right) \\ i_{bs} &= I_{max\_s}\cos\left(\omega_{st}t - \tfrac{2\pi}{3} + \alpha\right) \\ i_{cs} &= I_{max\_s}\cos\left(\omega_{st}t - \tfrac{4\pi}{3} + \alpha\right) \end{aligned} \tag{4.28}$$

Step T6: Following the above steps, we get the torque expression having inner rotor current terms also, which are not available to us in practical case and needs to be converted in terms of stator current. In order to represent these inner rotor currents in terms of stator current quantities ***Step V4*** of Section 4.2.1 is followed. Using these converted inner rotor currents the final torque expression of DRM in the desired form is given by (4.29).

$$T = \frac{P}{2}\cdot 3\cdot\left[\left(\frac{I_{max\_s}}{\sqrt{2}}\right)\left(\frac{\phi_{max\_s}}{\sqrt{2}}\right)\sin\left(\alpha - \delta_{st\_pm}\right) + \frac{\omega_{st}R_r s M^2_{max\_sr\_ph}}{\left(R_r^2 + s^2L_{rr}^2\omega_{st}^2\right)}\left(\frac{I_{max\_s}}{\sqrt{2}}\right)^2 + \left(\frac{I_{max\_s}}{\sqrt{2}}\right)\left(\frac{\phi_{max\_r}}{\sqrt{2}}\right)\right.$$
$$\left.\cdot\frac{M_{max\_sr\_ph}s\omega_{st}\cos(\delta_{pm\_im} + \delta_{st\_im} - \alpha - \varepsilon)}{\sqrt{R_r^2 + s^2L_{rr}^2\omega_{st}^2}}\right] \tag{4.29}$$

where,

$$\varepsilon = \tan^{-1}\left[\frac{(\omega_{st} - \omega_r)L_{rr}}{R_r}\right]$$

$$s = \frac{\omega_{st} - \omega_r}{\omega_{st}}\ \text{, and}\quad M_{max\_sr\_ph} = \frac{3}{2}M_{max\_sr}$$

The torque expression in (4.29) represents the overall torque of DRM. It is clearly seen from the

expression that the torque developed has contribution from each motor part. It can be deduced that the first term is due to interaction of stator and outer rotor fields, the second term is due to interaction of stator and inner rotor fields and the third term is due to interaction between inner rotor and outer rotor fields. Thus, the torque represented by the first term is delivered by outer rotor and that by the second term is delivered by inner rotor, whereas the torque given by the third term is shared by both the rotors.

Torque developed in outer rotor has contribution from both stator and inner rotor and represented in (4.29) by first and third terms respectively. Similarly, torque developed in inner rotor is due to stator and outer rotor represented by second and third terms respectively. The torque developed in DRM depends upon the number of pole pairs ($P/2$). Since, throughout the development of the torque expression a single pole pair was considered, as a result for a motor with P number of poles, the developed torque expression is multiplied with pole pairs ($P/2$).

4.2.3 Verification of the Developed Torque Expression

The torque expression in the previous section has been obtained with energy method. The torque can also be obtained from the equivalent circuit developed in Section 4.2.1. In this section torque obtained from EEC has been obtained and is verified with that given by (4.29).

In order to obtain electromagnetic torque from EEC, air-gap power needs to be calculated first. Then, air-gap power divided by the mechanical synchronous speed will provide us the torque expression. It can be seen from Fig. 4.3, there are three sources for air-gap power V_1, R_r/s and V_2. Total air-gap power (P_g) contributed by these three in symbolic form is given by (4.30) and complete expression are given in (4.31).

$$P_g = V_1 I_s + (I_r')^2 \frac{R_r}{s} + V_2 I_s \tag{4.30}$$

$$\begin{aligned} P_g = {} & \omega_{st} I_s \phi_s \cos(\delta_{st\_pm} + \frac{\pi}{2} - \alpha) + \frac{\omega_{st}^2 R_r s M_{max\_sr\_ph}^2 I_s^2}{R_r^2 + s^2 L_{rr}^2 \omega_{st}^2} \\ & + \frac{\omega_{st} I_s \phi_r M_{max\_sr\_ph} s \cos(\delta_{pm\_im} + \delta_{st\_im} - \alpha - \varepsilon)}{\sqrt{R_r^2 + s^2 L_{rr}^2 \omega_{st}^2}} \end{aligned} \tag{4.31}$$

Air-gap power presented in (4.31) is single phase power as the equivalent circuit is per-phase. Thus, for three phase air-gap power it needs to be multiplied by 3. In order to obtain electromagnetic torque from three phase air-gap power, it is divided by mechanical synchronous speed ($(2/P)\omega_{st}$).

The torque obtained from the EEC is presented in (4.32).

$$T_g = \frac{P}{2} \cdot 3 \cdot \left[\underbrace{I_s \phi_s \cos(\delta_{st\_pm} + \frac{\pi}{2} - \alpha)}_{T1} + \underbrace{\frac{\omega_{st} R_r s M_{max\_sr\_ph}^2 I_s^2}{R_r^2 + s^2 L_{rr}^2 \omega_{st}^2}}_{T2} \right.$$
$$\left. + \underbrace{\frac{I_s \phi_r M_{max\_sr\_ph} s \cos(\delta_{pm\_im} + \delta_{st\_im} - \alpha - \varepsilon)}{\sqrt{R_r^2 + s^2 L_{rr}^2 \omega_{st}^2}}}_{T3} \right] \tag{4.32}$$

Torque equation in 4.32 has three terms named as $T1, T2$ and $T3$. Out of these terms $T1$ and $T3$ have terms corresponding to magnet flux and are also sensitive to initial angle of PM rotor. Whereas, the term $T2$ only has terms corresponding to cage rotor. Thus, terms $T1$ and $T3$ can be considered as torque of outer rotor (PM rotor) and $T3$ as torque of inner rotor (cage rotor).

It can be easily observed that torque obtained from EEC and by energy method in (4.32) and (4.29) respectively matches and thus validates the torque expression for the considered DRM.

4.3 FEA Validation

In Section 4.2 SSM of DRM comprising the EEC and torque equation are developed. In order to validate the model developed, the results are compared with those obtained from the FEA model analyzed using ANSYS Maxwell 14.0.0. The remaining setting for the FEA analysis are same as explained in Section 2.5. Internal algorithms of Maxwell has been used for meshing and torque calculation. Torque in both outer and inner air-gaps have been computed in FEA and their sum is compared with the overall torque obtained using SSM. All the torque values are average values after the motor has achieved steady state.

4.3.1 Determination of parameters of EEC

The parameters for EEC were determined mainly from FEA model. The FEA model for the DRM was created in two steps:

- Firstly, an induction motor model with Ansys RMxprt is created with an leaving the space for outer PM rotor as air-gap. This model is analyzed and Maxwell 2D design is created from RMxprt.

- A separate geometry is created for outer rotor and is inserted in the 2D model created in the previous step.

The induction motor model created in the first step gives all the parameters related to induction motor model i.e.R_s, R_r, L_{rr}, L_{ss}, $M_{max\_sr\_ph}$ and the same are used in EEC calculations.

The parameter ϕ_{max_s} is calculated analytically using flux per pole as presented in (4.33).

$$\phi_{\max\_s} = B_{av} \cdot \frac{2\pi R_{OR}}{P} \cdot L \cdot N_{ph} \tag{4.33}$$

where, B_{av} is the average outer air-gap flux density, R_{OR} is the outer radius of outer rotor, L is the length of the machine and N_ph is the series turns per phase. With DRM is was observed that, B_av of 0.25 T is obtained with FEA. For the present DRM model R_{OR}=318.6 mm, L=834 mm, P=12 and N_{ph}=288. The parameter $\phi_{\max\_r}$ has been calculated in the similar way as $\phi_{\max\_s}$. First equivalent number of turns for three phase winding for the cage rotor is found and then using the turns ratio of stator and rotor, stator referred value of $\phi_{\max\_r}$ is calculated. The procedure of determining equivalent turns for cage rotor is presented in Appendix 9. The equation for $\phi_{\max\_r}$ calculation is given by (9.12).

$$\phi_{\max\_r} = B_{av} \cdot \frac{2\pi R_{IR}}{P} \cdot L \cdot \frac{3N_{ph}}{N_b} \tag{4.34}$$

The various motor parameters appearing in the voltage and torque equations are given in Table 4.1. Other specification required to make the FEA model of DRM are given in Table 4.2. The slot dimensions for stator and rotor are presented in Fig. 4.5.

Table 4.1: DRM Parameters

Symbol	Value	Unit	Symbol	Value	Unit
R_r	0.59	Ω	R_s	0.23	Ω
f	50	Hz	P	12	
ϕ_{max_s}	9.82	Wb	ϕ_{max_r}	0.37	Wb
L_{rr}	0.09	H	L_{ss}	0.09	H
N_r	495	rpm	$M_{max\_sr\_ph}$	0.07	H
V_L	6000	V	α_m	1	

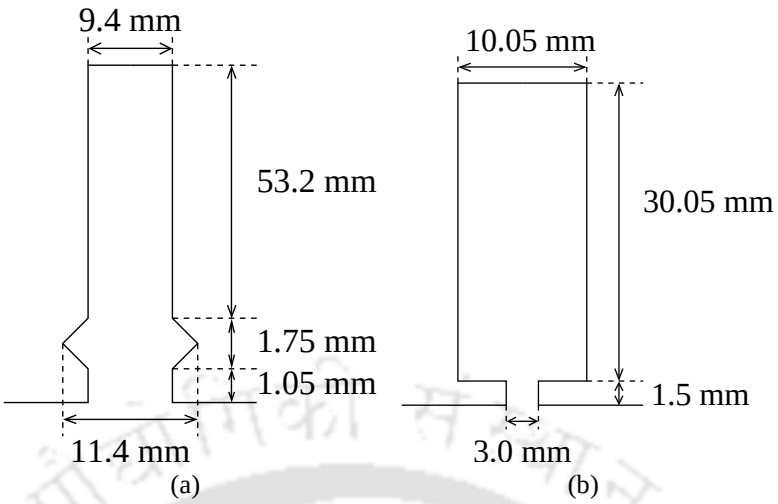

Figure 4.5: Slot dimensions (a) Stator (b) Inner rotor.

Table 4.2: Specifications of DRM.

Symbol	Value	Unit
Stator outer diameter	850.0	mm
Stator inner diameter	640.6	mm
Outer rotor outer diameter	637.2	mm
Outer rotor inner diameter	607.2	mm
Inner rotor outer diameter	603.2	mm
Inner rotor inner diameter	450.0	mm
Outer air-gap length	1.7	mm
Inner air-gap length	2.0	mm
Length of motor	834.0	mm
Number of stator slots	108	
Number of inner rotor slots	78	
Coil pitch for stator winding	10	slots
μ_r for permanent magnets	1.05	
B_r for permanent magnets	0.5	T

The cut-out section of the DRM in FEA at standstill is as shown in Fig. 4.6 and under rotation is shown in Fig. 4.7. As explained in the previous section, the outer rotor rotates at synchronous speed and inner rotor rotates at slip speed. It can be seen from Fig. 4.7 that the two rotors under rotating condition have different positions at a particular instant of time.

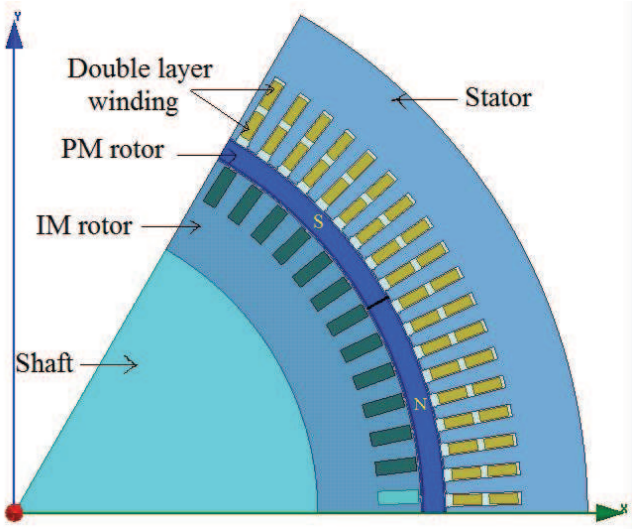

Figure 4.6: FEA model cut-out section of hybrid IM-PM DRM at standstill.

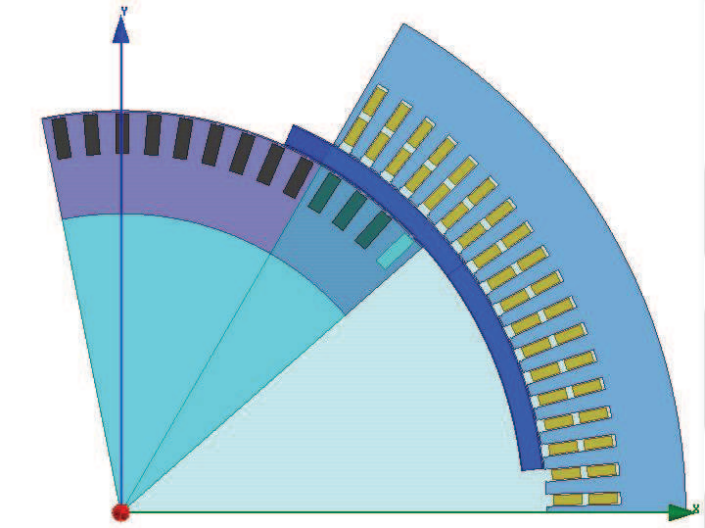

Figure 4.7: FEA model cut-out section of hybrid IM-PM DRM under rotation.

As discussed in the previous section, the torque in DRM depends on slip (s) of inner rotor and initial angle of outer rotor (δ_{st_pm}). The torque developed in DRM can be analyzed by keeping either s or δ_{st_pm} constant and varying the other. It is known that the stable operation of an IM lies within a very small range of slip (0-3%). Firstly, to analyze the operation of DRM, s is kept constant and δ_{st_pm} is varied from 0 – 360 electrical degrees.

The torque and maximum current variation in DRM against the initial shift angle of outer rotor δ_{st_pm} are as shown in Fig. 4.8 and Fig. 4.9 respectively.

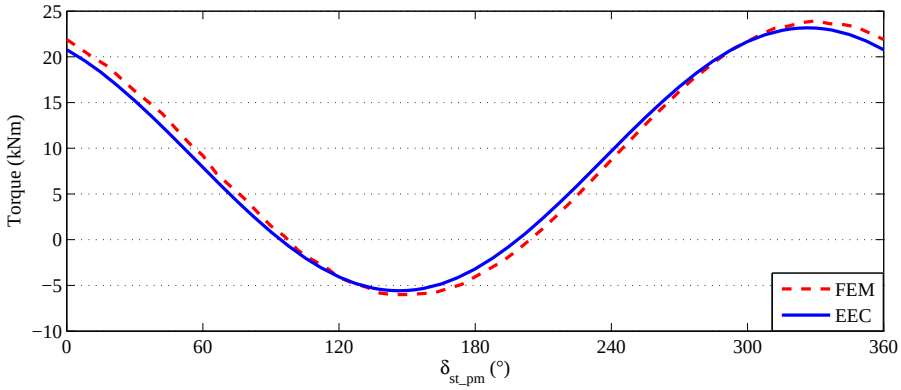

Figure 4.8: Comparison of total torque obtained from EEC and FEA w.r.t. δ_{st_pm} at $s = 0.022$.

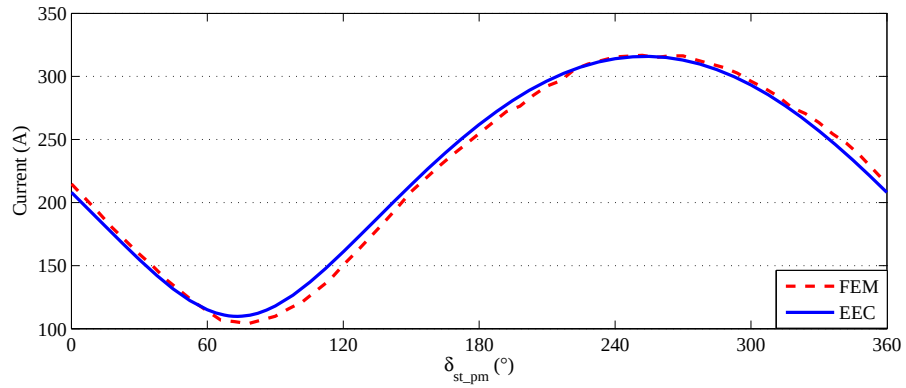

Figure 4.9: Comparison of maximum input current obtained from EEC and FEA w.r.t. δ_{st_pm} at $s = 0.022$.

Second set of validation has been performed by varying slip (s) of inner rotor for specific δ_{st_pm}. The torque and stator current results for this variation are presented in Figs. 4.10 and 4.11 respectively.

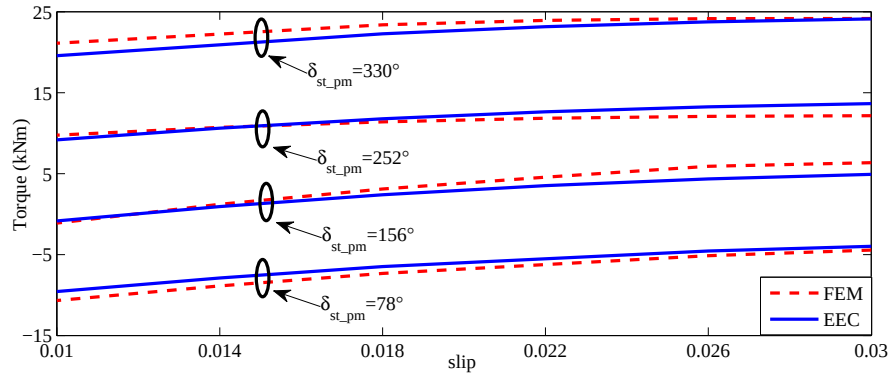

Figure 4.10: Comparison of total torque obtained from EEC and FEA w.r.t. slip (s) for various δ_{st_pm}.

The first and third terms of torque expression (4.29) have sine and cosine function of δ_{st_pm} and hence alternate between positive and negative values. Whereas, the second term is independent of δ_{st_pm} and hence is always positive. Observing the torque plot in Fig. 4.8 and 4.10, the negative torque

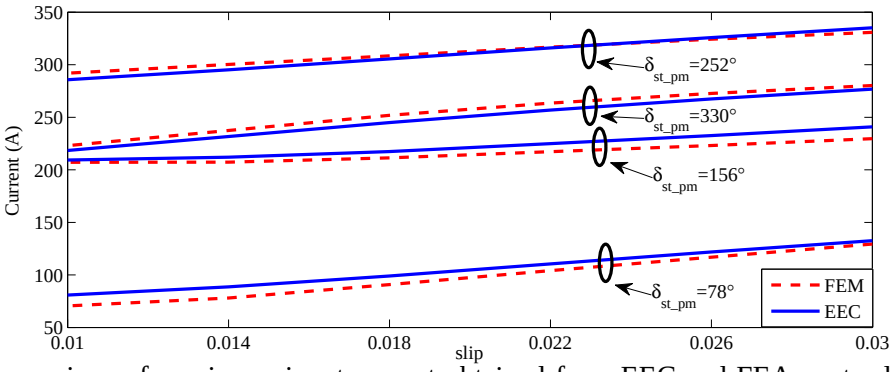

Figure 4.11: Comparison of maximum input current obtained from EEC and FEA w.r.t. slip (s) for various δ_{st_pm}.

represents that torque contributed by first and third terms are opposing the torque contributed by the second term (which is always positive). Therefore, to avoid opposition of torques DRM should be operated over a range of δ_{st_pm} that results in torque near its maximum positive value.

The input current drawn by a motor gives the indication of the electrical power input and hence the mechanical power output also. The plots of maximum input current of DRM in Fig. 4.9 and 4.11 showing the values from EEC and FEA matches very closely, indicating that motor model developed that is an electrical representation of DRM, draws same current as that of the FEA model. Maximum value of input current (I_{max_s}) is selected for comparison as from the voltage equation in (4.17), we can directly obtain I_{max_s}. Results from Figs. 4.8 - 4.11 show that the performance of the DRM predicted by the developed EEC and torque expression closely matches with that of FEA, thus validating the work. Additional results showing performance of DRM over $0° - 360°$ range of δ_{st_pm} for various slip (s) values have been presented in Fig. 4.12-4.13.

Having validated developed EEC with FEA, it can be further used to analyze the DRM torque characteristic for other δ_{st_pm} and s values. Fig. 4.14 and 4.15 shows torque characteristics for DRM for various values of δ_{st_pm} and s obtained from EEC.

In Fig. 4.14 various δ_{st_pm} have been selected including one having maximum torque ($\delta_{st\_pm} = 330°$) in Fig. 4.8 for analysis. It is observed from Fig. 4.14 that the torque characteristic looks similar to that of an IM. Unlike IM the torque at synchronous speed ($s = 0$) is not zero, this is due to the presence of torque due to outer rotor. Fig. 4.15 shows the torque characteristic of DRM w.r.t. δ_{st_pm} for various slip values. It is observed from the figure that with decrease in slip of inner rotor the torque

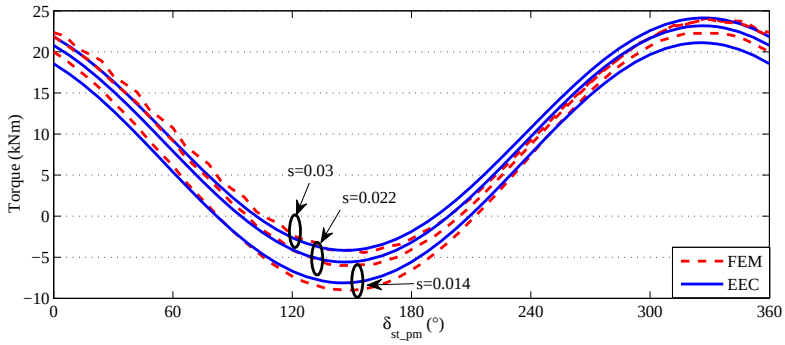

(a)

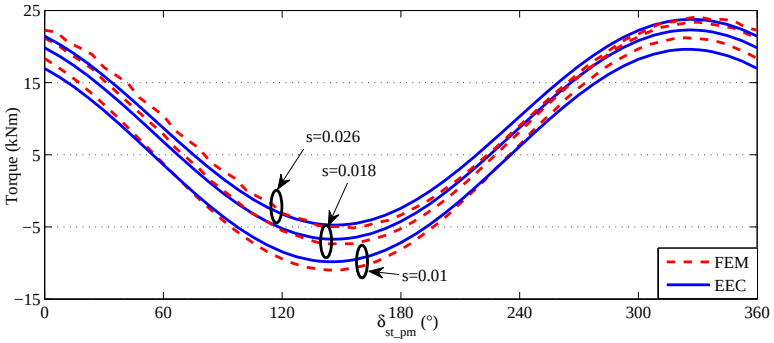

(b)

Figure 4.12: Comparison of total torque obtained from EEC and FEM w.r.t. δ_{st_pm} for various slip (s).

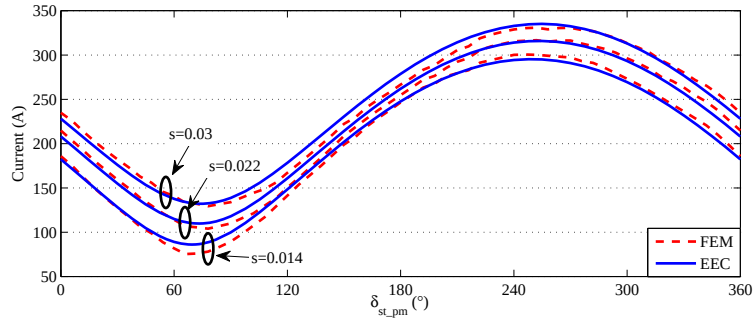

(a)

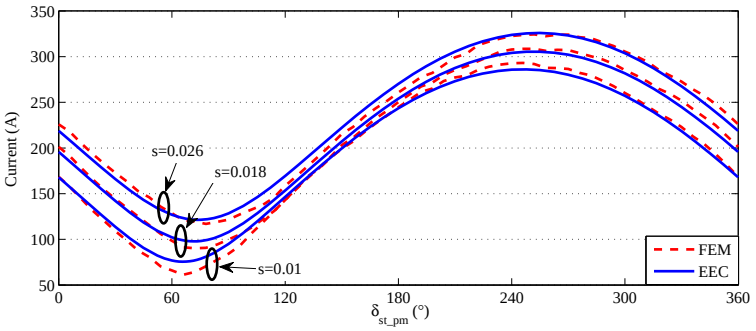

(b)

Figure 4.13: Comparison of maximum current obtained from EEC and FEM w.r.t. δ_{st_pm} for various slip (s).

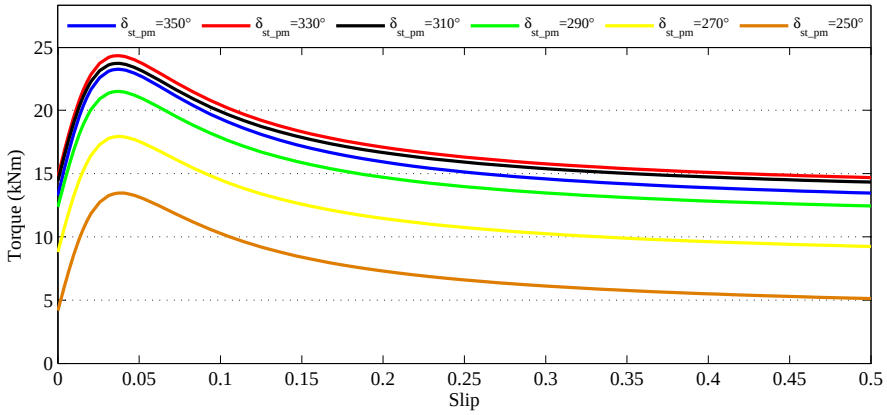

Figure 4.14: Torque characteristic obtained from EEC for DRM w.r.t. slip (s) for various δ_{st_pm}.

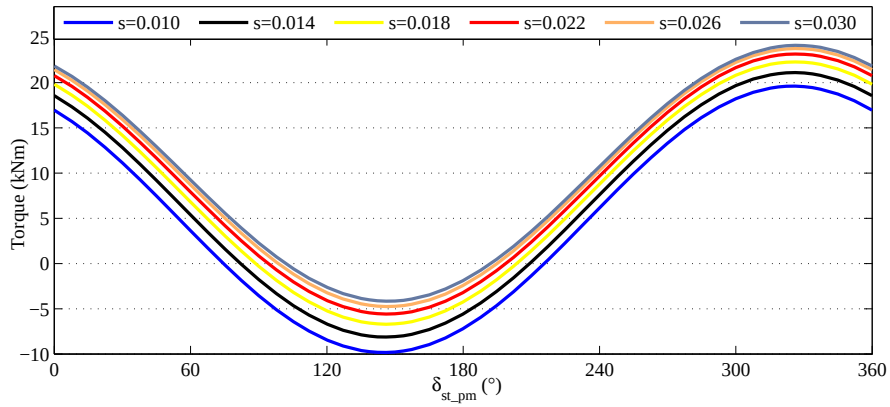

Figure 4.15: Torque characteristic obtained from EEC for DRM w.r.t. δ_{st_pm} for various s.

characteristic shifts downwards i.e. torque decreases for every δ_{st_pm}. It can be deduced that the motor will produce minimum torque at $s = 0$, and that will be torque only due to outer rotor. At this point DRM will behave as permanent magnet synchronous motor (PMSM).

4.4 Conclusion

The SSM comprising a novel EEC and the torque expression for a new type of motor in the form of a hybrid IM-PM DRM is developed in this work. This model developed provides an in-sight to the operation and the characteristics of DRM which are not known precisely till now. The method used in the development of the model is very simple, systematic and general and has thus resulted in a model which is easy to interpret in-spite the fact that the motor construction was complex. The EEC and the torque expression developed for DRM, convey the interaction amongst the three motor parts not just to explain its operation but also brings out the differences in DRM as compared to a normal IM and PM. The model also describes some important issues that should be considered to operate the DRM for

better performances. The SSM parameters determination of DRM is also presented. The input stator current obtained from the EEC closely matches the values obtained from FEA to validate the EEC. Similarly the torque determined from the torque expression developed also closely matches with that of FEA results, to validate the work done. The method is also presented in a simple and systematic manner and can be easily implemented for any new type of motor with different configuration.

5

Design and prototyping of DRM

Contents

5.1 Introduction

In this chapter design and prototyping of DRM has been discussed. The first prototype of the motor has been made keeping the following objectives in mind:

- Practical feasibility of the proposed DRM configuration.
- Practical understanding the working principle of DRM.
- Validation of FEA and EEC models with practical results.
- Finding out the suitable control strategy for DRM.
- Determine the possible mechanical designs for the proposed DRM configuration.

5.2 Design of DRM

The design of DRM has been discussed in two parts i.e. electrical and mechanical design. Following subsections present the electrical design for the selected configuration.

5.2.1 Electrical design of DRM

Since the major objectives of first prototype of DRM are validation of proposed models and understanding of its working, the design has been made such that it can be tested with the available resources in the laboratory. Thus, the motor is designed such that it is compatible with the available platform and can be coupled with other motors and generators available in the laboratory. The electrical design of DRM has been further discussed in detail in the following subsections.

5.2.1.1 Design of stator

Design of any electrical motor or its part starts with the constraints which need to be satisfied. For the stator of DRM, following constraints were given:

- The outer diameter of the stator must not be greater than 150 mm, for the motor to fit into available platform in the laboratory.
- The stator current of the motor must not be greater than 2 ampere.
- Rated line to line voltage for stator must be 380 V.

In view of the above constraints the outer diameter (R_o) of the motor had been chosen to be 150 *mm*. As the inner rotor of the DRM is PM rotor, DRM can be considered an Interior Permanent Magnet (IPM) type motor. As with increased number of poles, the motor volume decreases, for DRM 8 poles are chosen [49]. Since the outer diameter of the stator has a constraint of 150 *mm*, number of slots in the stator should be such that it can accommodate 3-phase winding for 8 poles and also, there should be sufficient tooth width to avoid saturation. Hence, the number of stator slots have been chosen as 36. Fig. 5.1 shows the dimensions for the stator slots. With 36 number of slots, it is feasible to make double layer fractional slot winding (slots/pole/phase≠1) for 8 poles. 36 number of slots also helps to avoid cogging torque also as slots per pole is not an integer (36/8 = 4.5) [14].

The voltage and current specification of the motor are 380 *V* and 2 *A* respectively. Table 5.1 presents the winding details for the stator.

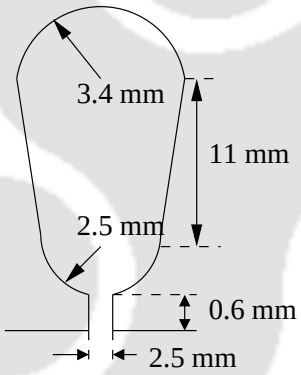

Figure 5.1: Dimensions of slots on Stator.

5.2.1.2 Design of outer rotor

The outer rotor of DRM is IPM type rotor. As discussed in Chapter 2, for proper operation of DRM the complete stator flux has to link both, the inner and outer rotor. Therefore, all the flux must pass to inner rotor via the outer rotor. Thus, the magnets cannot be placed on the surface of the rotor and have to be embedded in the core like in an IPM motor. Many configurations of PMs are reported in literature and are used practically [50]. Some of the configurations are shown in Fig. 5.2.

In all the configurations shown in Fig. 5.2, except for 5.2(a), all makes flux loop with adjacent magnets and thus their flux will not flow to inner rotor. However, for magnet configuration in Fig. 5.2(a), with proper flux guides (or flux barriers), the flux can be made to flow towards inner rotor.

Table 5.1: Winding details for stator of DRM

Parameter	Value	Unit	
Number of slots	36	Number of poles	8
Number of phases	3	Slots/pole/phase	1.5
Winding type	Lap	Winding connection	Delta/star
Parallel paths	1	Current density	3.42 A/mm^2
Coil throw	4	Winding wire	AWG 22
Number of strands	1	Number of turns	55
Slot fill factor	50 %	Mean turn length	216 *mm*
Turns per phase	660	Insulation class	F

Thus, configuration in Fig. 5.2(a) is used for outer rotor of DRM. The final slot shape for outer rotor is shown in Fig. 5.3.

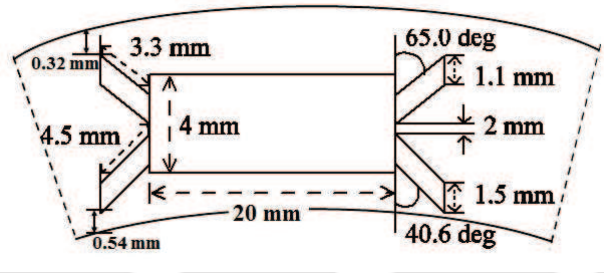

Figure 5.3: Dimensions of slots on outer rotor.

It can be observed from Fig. 5.3 that flux guides have been made on all corners of the bar magnets to guide the flux towards stator and inner rotor and prevent any flux loop with adjacent magnets.

5.2.1.3 Design of inner rotor

The inner rotor of DRM is squirrel cage type rotor like the rotor of an IM. To decide the number of bars and shape of the bar, standard design principles have been followed [51]. Since the cage rotor is placed inside the outer rotor, relatively less space is available for the cage rotor. Therefore, unlike most of the IM, the number of bars for cage rotor have been selected less than number of slots of stator i.e. 34. The dimensions of the slots for the cage rotor are shown in Fig. 5.4.

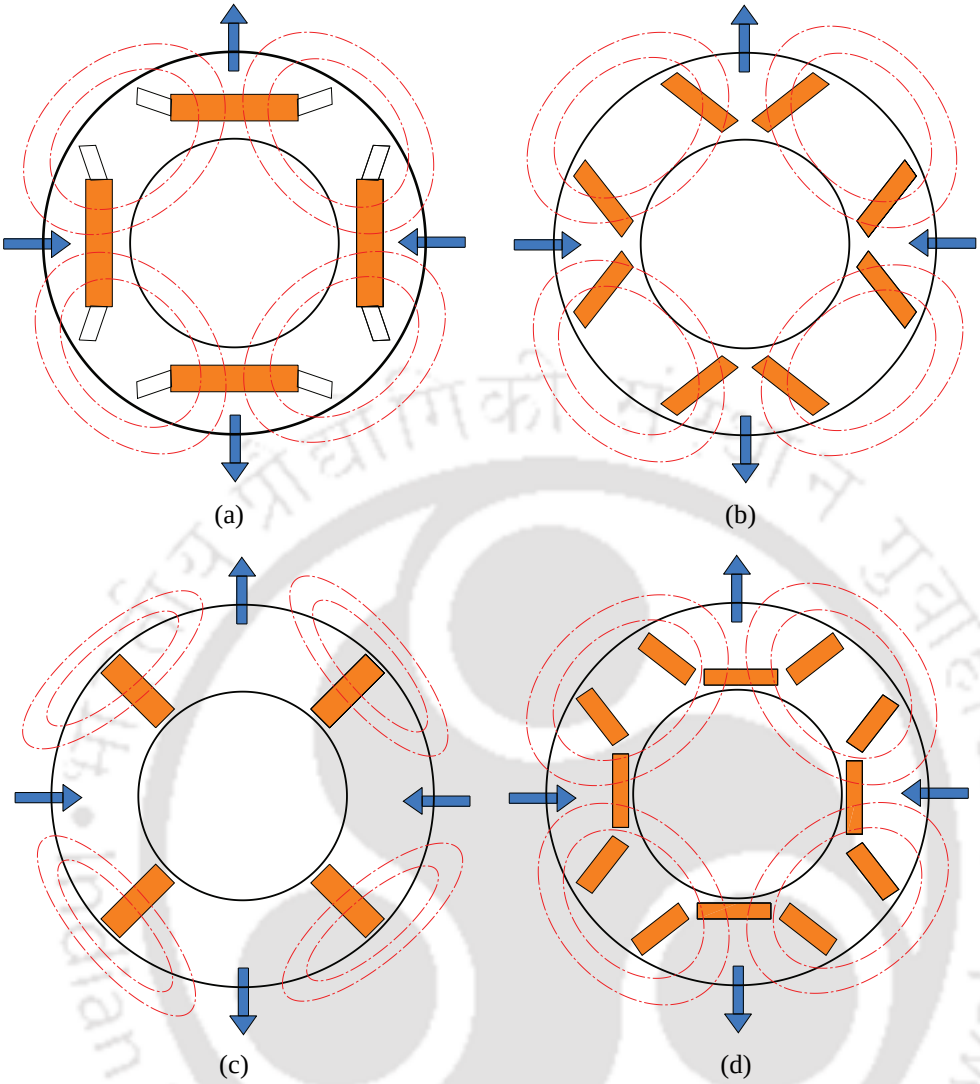

Figure 5.2: Configurations of IPM rotors based on magnet shape (a) Bar type (b) V type (c) Spoke type (d) Tub type.

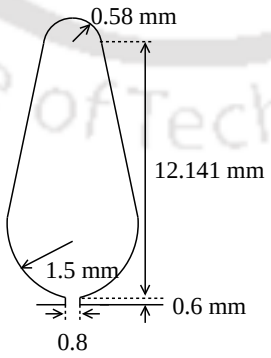

Figure 5.4: Dimensions of slots on squirrel cage type inner rotor.

5.2.1.4 FEA modeling of DRM

The design of DRM discussed in previous sections has been validated with FEA analysis using Ansys Maxwell 14.0. The remaining setting for the FEA analysis are same as explained in Section 2.5. The model was voltage excited and hence the currents were induced in the rotor bars. Holes were created for outer rotor bolts in the FEA model as the bolts were made of non-magnetic steel. The FEA model of the DRM is shown in Fig. 5.5. The flux lines for the model are shown in Fig. 5.6. It can be observed from the figure that the flux lines link all the parts i.e. stator, outer rotor and inner rotor of the motor. With the flux barriers on the outer rotor, all the possible flux loops are prevented and flux is guided towards stator and inner rotor.

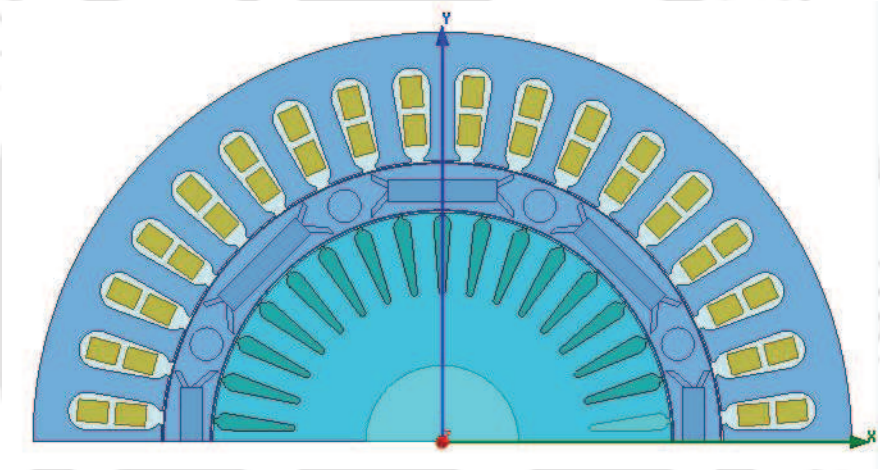

Figure 5.5: FEA model for the finalized design of DRM.

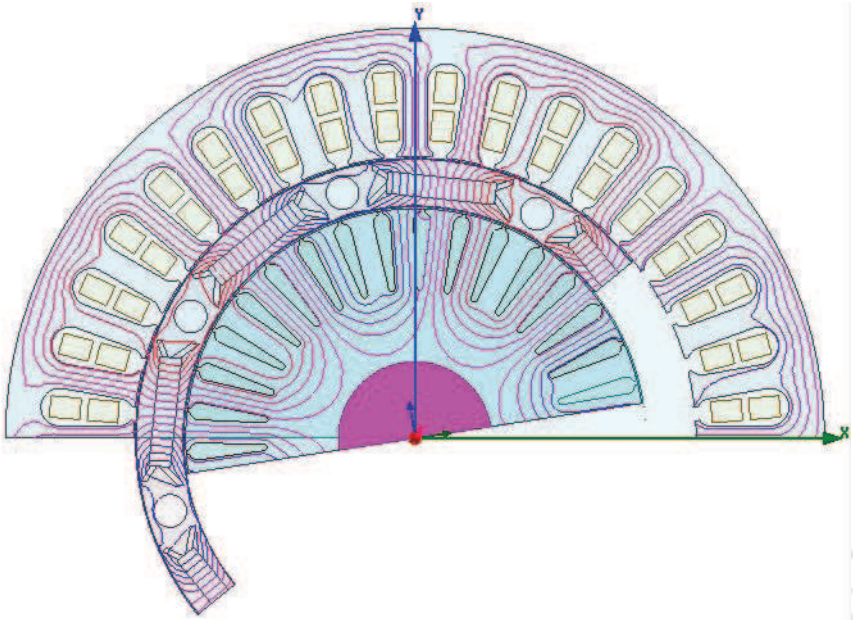

Figure 5.6: Flux distribution for the FEA model of DRM.

5.2.2 Mechanical design of DRM

Electric motors have been around for more than century and its mechanical design has become quite mature considering cooling, mechanical strength and vibration viewpoints. However, being a new configuration, the standard mechanical design with rotor mounted on two bearing cannot be used for DRM. The DRM has two concentric rotors and both the rotors rotate independently. The inner rotor is inside the outer rotor and rotate at different speed. The inner rotor can be mounted on shaft but the outer rotor cannot be connected to this shaft as both rotate at different speed. Therefore, a hollow shaft has been designed for outer rotor and its output is taken through a gear arrangement. Thus, the mechanical design of the motor has been made such that output of both the rotors are available independently. This design will help in performing tests on either of the rotor independently and thus will help to understand the motor. The required CAD drawings for manufacturing have been made using the design platform CATIA. Figs. 5.7-5.11 show final CAD drawing for DRM and its different parts. Fig. 5.7 shows the inner cage rotor with both side bearings mounted. Fig. 5.8 shows the outer rotor with its bearing and gear mounted. The gear on the outer rotor has been made so that its torque can be taken independently as shown in Fig. 5.9. Fig. 5.10 and 5.11 show the complete assembly and cross section view of the DRM.

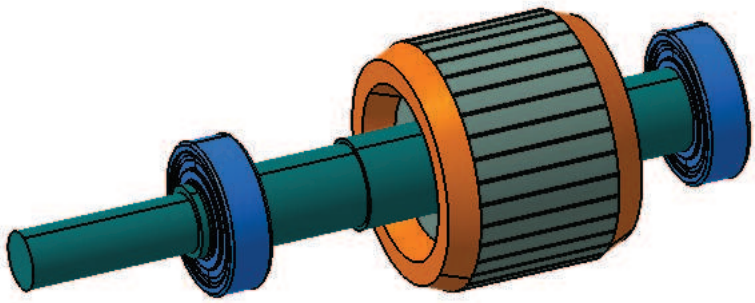

Figure 5.7: CAD drawing for inner cage rotor with both side bearings mounted.

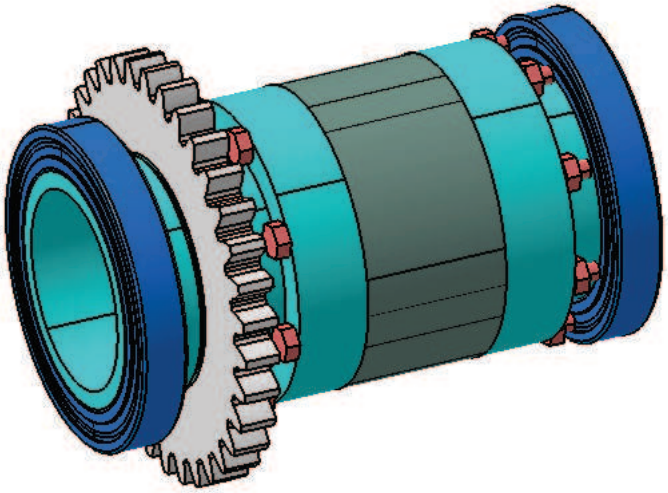

Figure 5.8: CAD drawing for outer PM rotor with both side bearings and gear mounted.

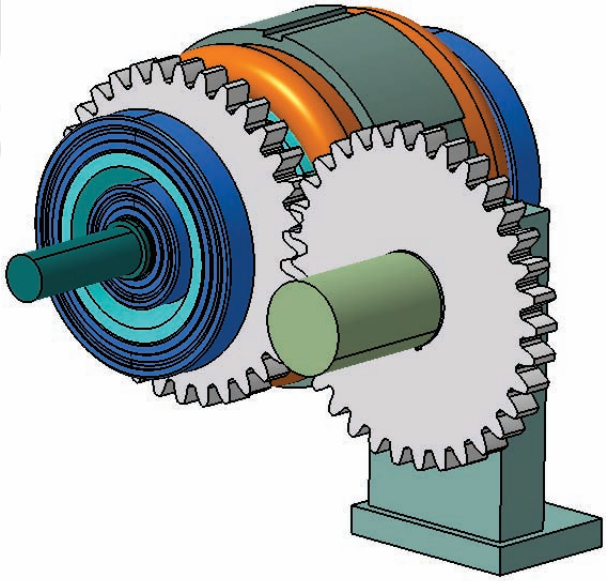

Figure 5.9: CAD drawing for DRM showing two output shaft.

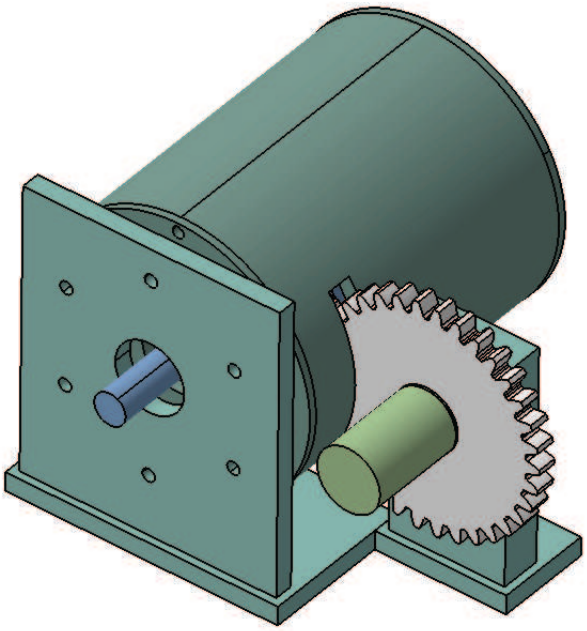

Figure 5.10: CAD drawing for the complete assembly of DRM.

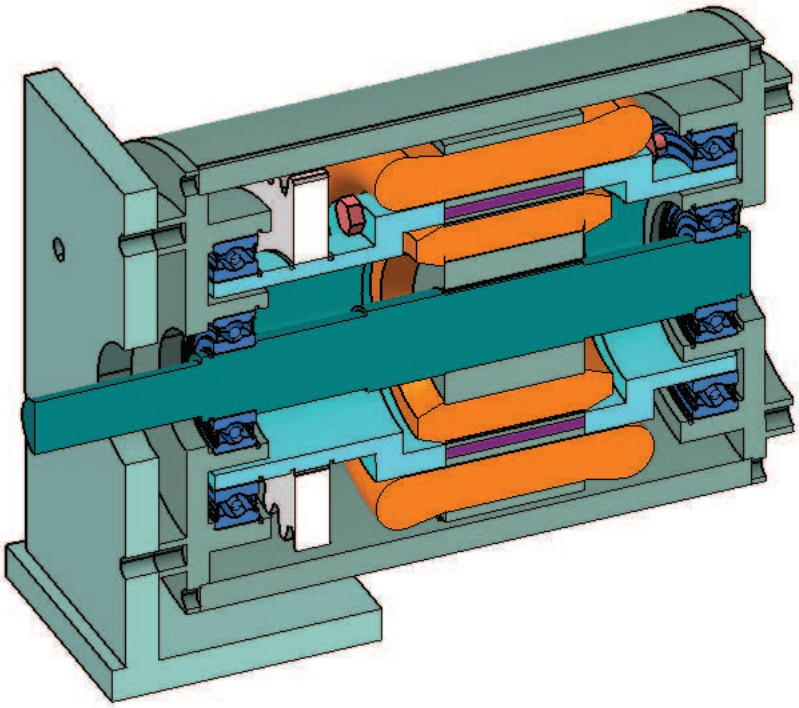

Figure 5.11: CAD drawing showing cross sectional view of the DRM.

5.3 Manufacturing of DRM

The dual rotor motor is manufactured at NFTDC (Non Ferrous Material Technology Development Centre), Hyderabad. The steps involved in prototyping the motor are shown in Fig. 5.12.

Table 5.2: Mechanical specification used for DRM prototyping.

Parameter	Value	Unit
Stator outer radius (R_o)	75.00	mm
Stator inner radius (R_s)	51.50	mm
PM rotor outer radius (R_m)	51.00	mm
PM rotor inner radius (R_a)	42.50	mm
Cage rotor outer radius (R_r)	42.00	mm
Shaft radius	14.00	mm
Motor stack length (L_m)	50.00	mm
Number of stator slots	36	
Number of inner rotor slots	34	
Width of the magnet	20.00	mm
Height of the magnet	4.00	mm
Pole pairs (p)	4	

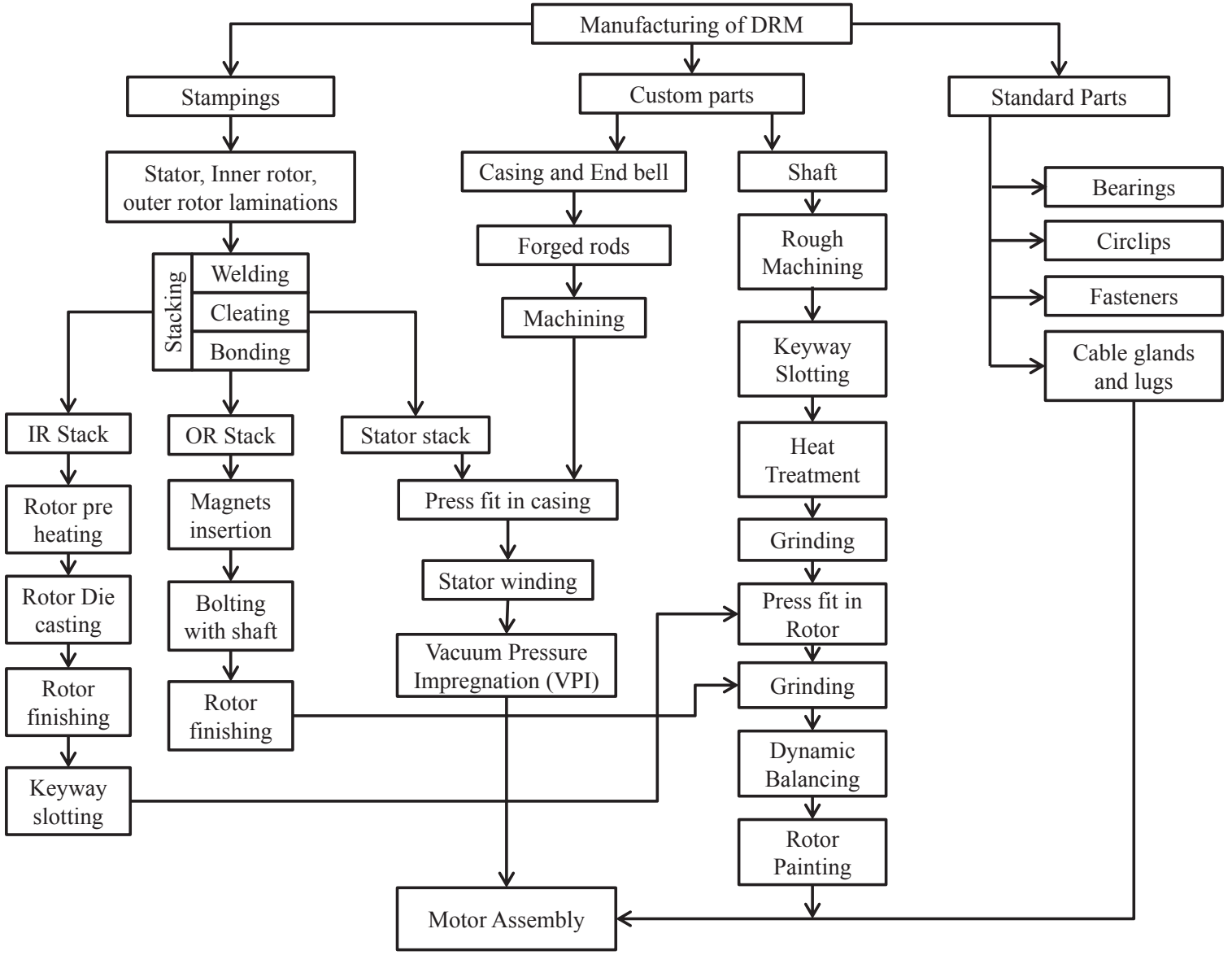

Figure 5.12: Flowchart depicting various processes involved in the manufacturing of DRM.

Table 5.2 gives the mechanical specifications finalized for DRM manufacturing. Fig. 5.13 - 5.16 show the pictures of the lamination cut from the sheet of the material 50C350AP with laser cutting machine. Fig. 5.17 - 5.24 present pictures of various DRM parts during different stages of manufacturing. Fig. 5.26 shows the complete DRM after assembly operation.

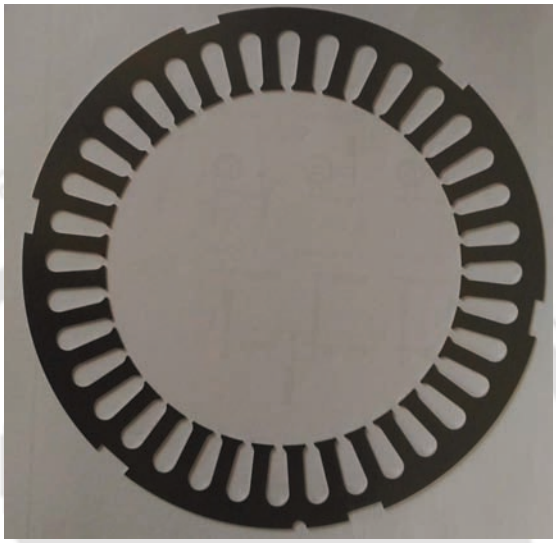

Figure 5.13: Lamination for Stator.

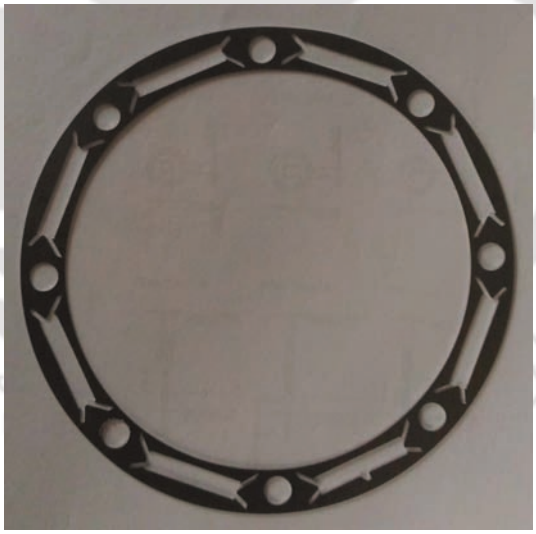

Figure 5.14: Lamination for PM rotor.

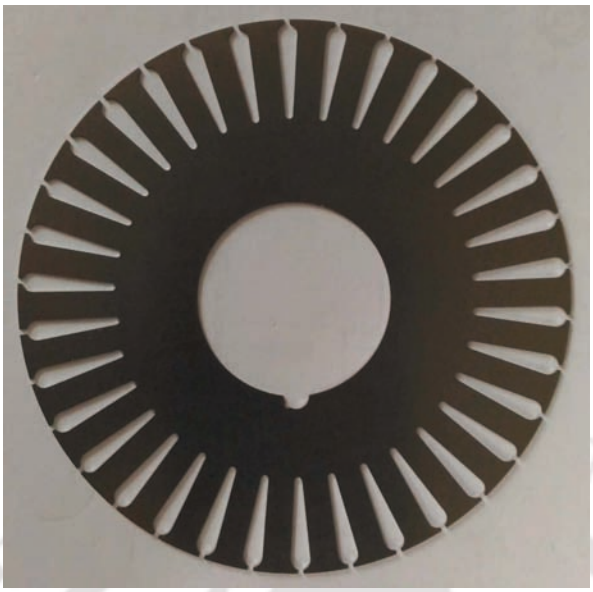

Figure 5.15: Lamination for Rotor.

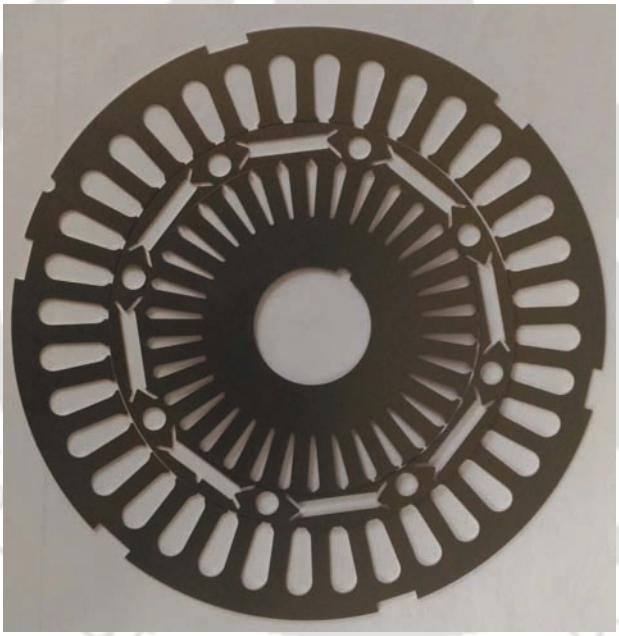

Figure 5.16: Picture of all lamination put together.

(a)

(b)

Figure 5.17: (a) DRM frame (b) frame with stator stack.

(a) (b)

Figure 5.18: DRM stator under winding operation.

(a) (b)

Figure 5.19: Finished DRM stator ready for assembly.

(a)

(b)

(c)

Figure 5.20: (a) Copper caste cage rotor (b) and (c) Finished cage rotor ready for assembly.

(a) (b)

(c)

Figure 5.21: (a) PM rotor lamination stack (b) PM rotor with end supports (c) Permanent magnets.

(a)

(b)

Figure 5.22: (a) and (b) PM rotor with inserted magnets.

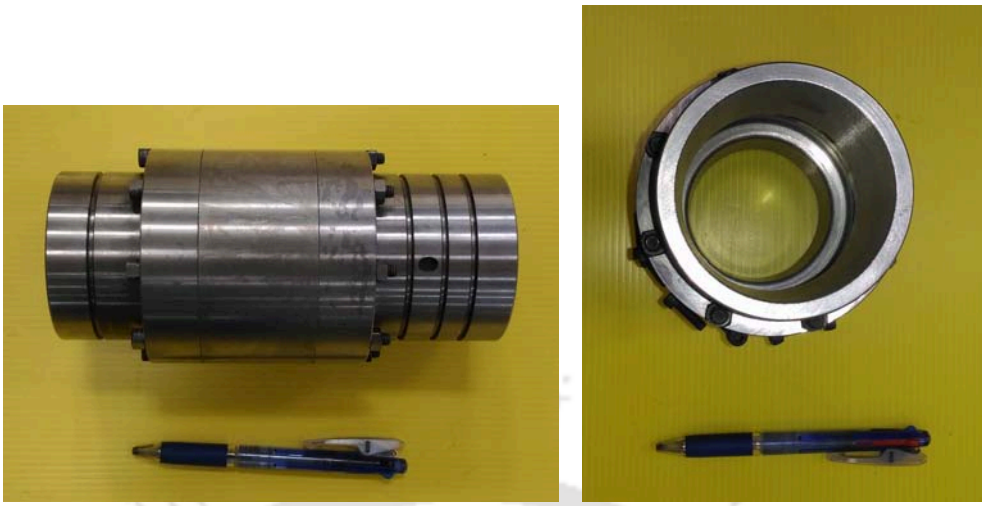

(a) (b)

(c)

Figure 5.23: Finished PM rotor ready for assembly.

(a)

(b)

Figure 5.24: (a) Gear, circlips, bearings required for assembly (b) All DRM components ready for assembly.

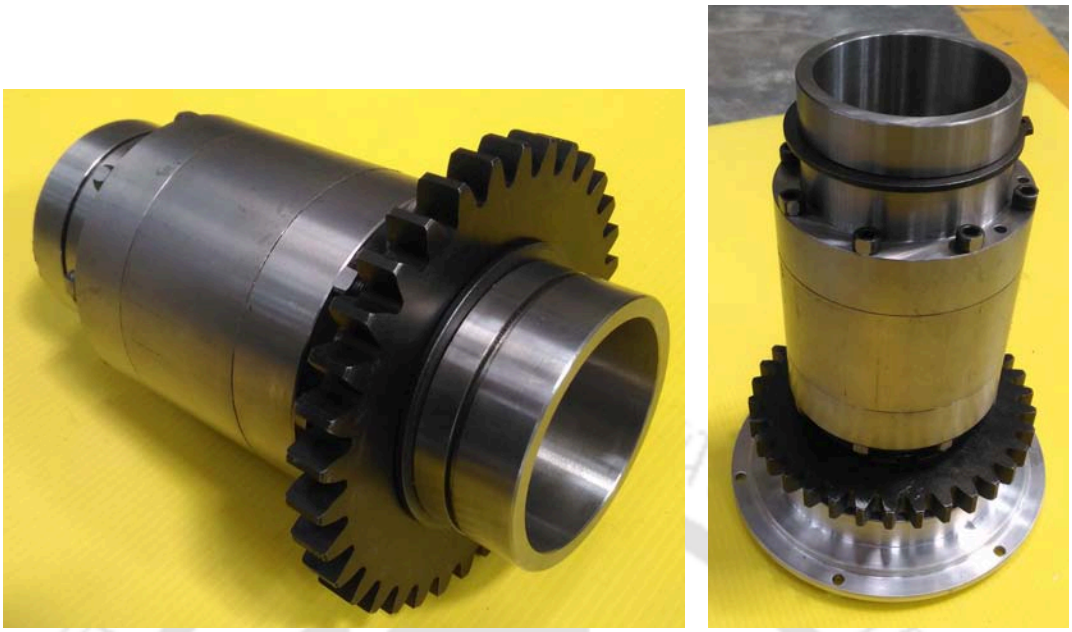

(a) (b)

(c)

Figure 5.25: DRM under assembly operation.

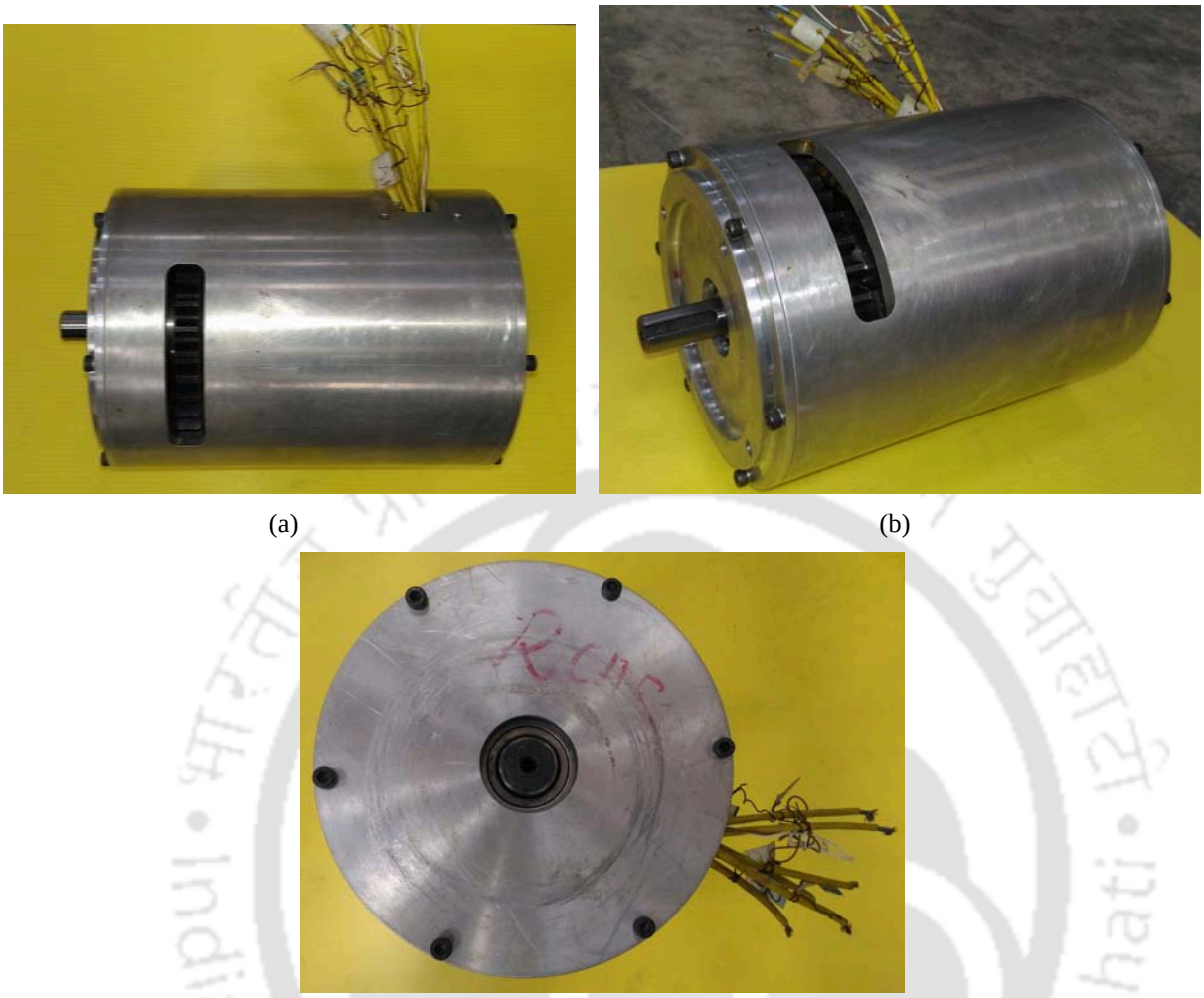

(a) (b)

(c)

Figure 5.26: Final DRM after assembly completion.

5.4 Installation of Hall sensors in DRM

The position of the Hall sensor depends upon the number of poles and number of stator slots of the motor. For proper operation of the motor, the Hall sensors have to be electrically 120° apart from each other. Thus using the number of poles of the motor mechanical position of the Hall sensor is calculated. The calculation for Hall sensor position for DRM is explained below:

No. of stator slots for DRM = 36

Slot pitch in mechanical degrees= 360°/36 = 10°

No. of poles for DRM = 8

Mechanical degrees for 120 electrical degrees for 8 poles = 120°/(8/2) = 30°

$$\text{Number of slot pitches between two Hall sensors} = 30^\circ/10^\circ = 3$$

Thus, Hall sensors have to be placed at a difference of 3 slot pitches between two sensors. Since, the Hall sensor surface cannot be under the core of the stator otherwise it will not get sufficient field intensity to detect the magnets; they could not be inserted inside the slots. Thus, stator teeth were cut and Hall sensors were inserted in the grooves made. Fig. 5.27 shows the three Hall sensors placed in the stator. After the correct placement of Hall sensor its leads were fixed to the stator winding with silicon rubber such that they do not move and reliability in operation is ensured.

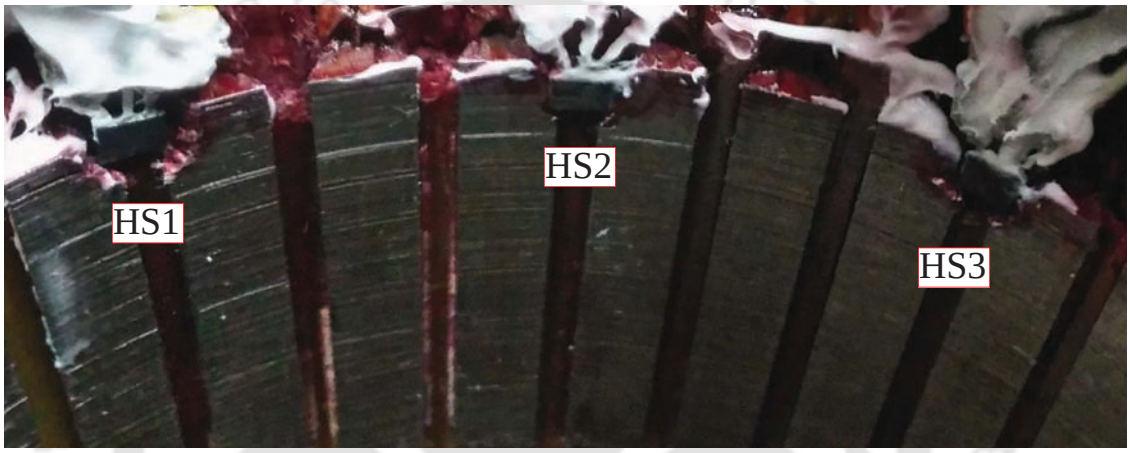

Figure 5.27: Position of Hall sensors in stator.

5.5 Summary and Conclusion

Complete design of DRM including electrical and mechanical design has been discussed in this chapter. The main objective with the first prototype of the motor is to validate the working principle and testing of the motor for better understanding. With the finalized design, output of both the rotors can be obtained independently. For a practical application, the mechanical assembly has to be modified based on the requirement.

The next chapter presents various tests performed on the manufactured DRM. The control strategy used to run the DRM is the same as used for PMBLDC motor and is also discussed briefly in the chapter.

6

Testing of DRM

Contents

6.1 Introduction

In this chapter, testing of DRM is presented. DRM has two torque producing components i.e. inner and outer rotor. In order to properly understand its working principle and effect of loading on both its rotors, different tests are preformed and are discussed in subsequent sections of this chapter. The objectives of testing of DRM are as follows:

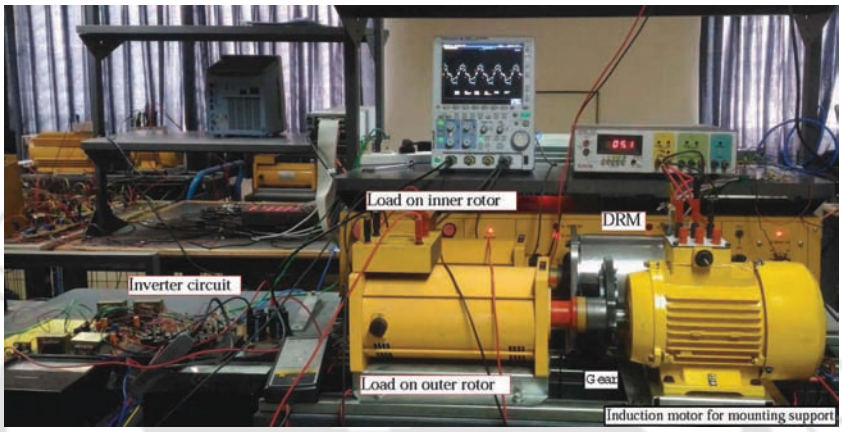

(a)

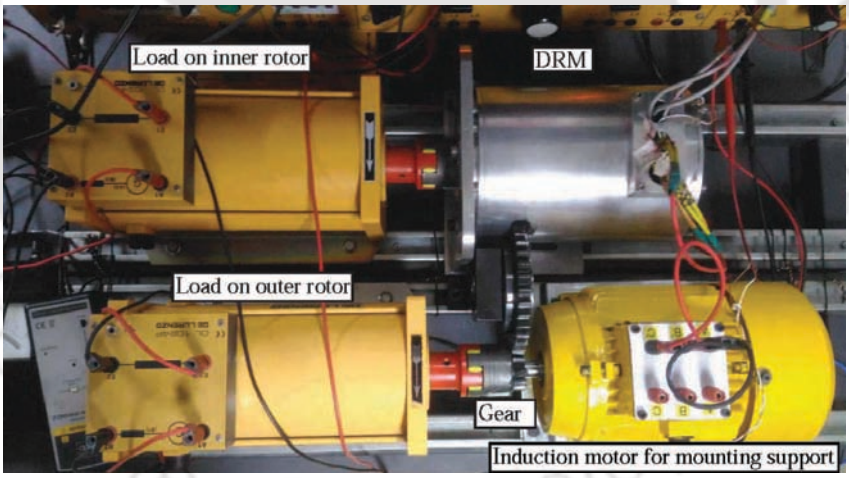

(b)

Figure 6.1: Experimental setup for DRM testing (a) front view (b) top view.

- Check the back emf waveform and Hall sensors outputs.
- Understand the working principle of DRM.
- Effect of loading any of the rotors individually.
- Effect of loading both the rotors.

- Validation of SSM and FEA model with experiments.

Fig. 6.1 shows the mounting of the motor and arrangement made to load both the rotors. For better understanding of the arrangement, front and top view of the setup are shown in Fig. 6.1(a) and 6.1(b) respectively. Flange mounting is used for DRM to fix it to the experimental platform. DC generators with resistances connected to their armature terminals have been used as loads for both the rotors. The inner rotor is coupled directly with the load as in case of any conventional motor whereas, the outer rotor is coupled to load through a gear arrangement as shown in the figures. The torque for both the rotors has been measured from the output power of the DC generators divided by mechanical speed in rad/sec. The output power of the DC generator are obtained as sum of power consumed by load resistance (R_L) as well as copper loss in generator windings as shown in (6.1). Since, due to mechanical constraints DRM was operated with low rpm throughout the experimental testing (maximum 150 rpm), the friction and windage losses were neglected. Considering the error due to friction and windage losses, it can be stated that, the torque measurement was done with an accuracy of 90%.

$$P_G = I_G^2 R_L + I_G^2 R_G \tag{6.1}$$

The electrical excitation to the motor has been provided using an inverter. The switching signals for the inverter switches are being generated using the dSPACE 1103 system. Following section describes the control strategies used to run the motor.

6.2 Control strategy for DRM

The working principle of the DRM has been presented in detail in the previous chapters. It was discussed that, when the stator is excited, the outer rotor rotates similar to a rotor in PM motor. This rotating outer rotor creates a rotating magnetic field in the inner air-gap and thus forces the inner rotor to rotate to minimize the electromagnetic induction. It can be observed from this discussion the rotation of outer rotor is vital for the operation of DRM and since the air-gap field of inner air-gap cannot be directly controlled, the outer air-gap field has to be controlled. Therefore, it is concluded that, DRM has to be operated as PM motor.

6.2.1 120° commutation technique

The simplest and widely used control technique of 120° commutation of stator phases based on Hall sensors output has been employed for DRM. The block diagram for the control technique is presented in Fig. 6.2.

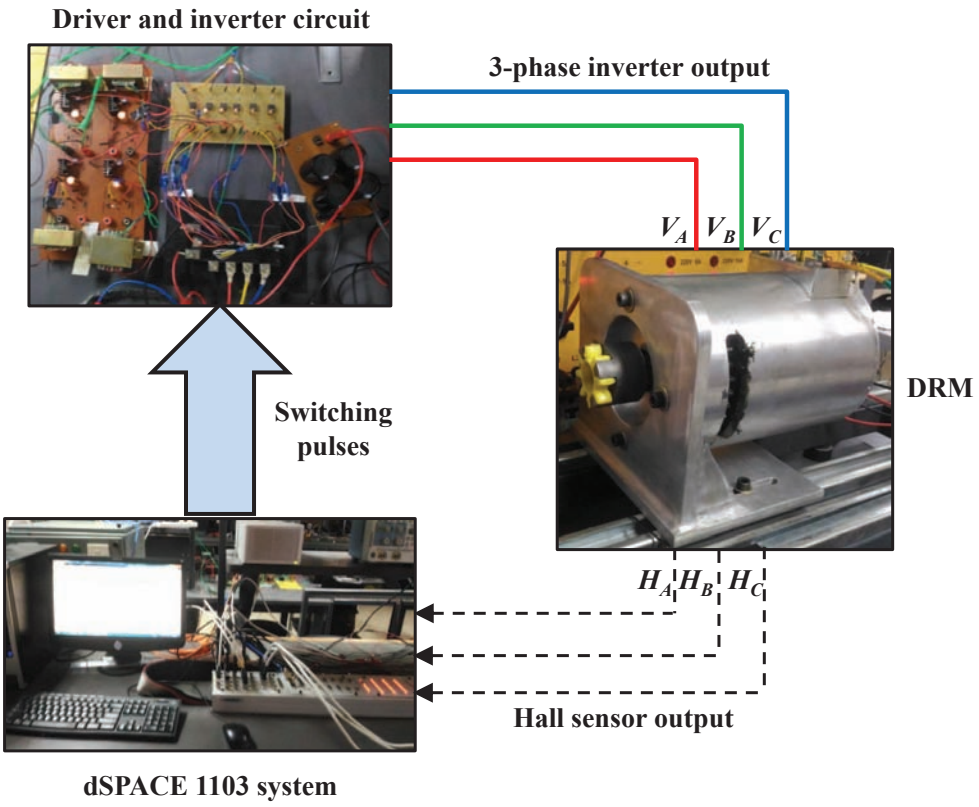

Figure 6.2: Experimental setup for DRM testing.

If the phases of the motor are commuted properly in synchronism with the rotor position then the outer rotor rotates smoothly and the inner rotor also rotates in order to catch up with the rotating field created by outer rotor. Circuit representation of the 3-phase inverter is shown in Fig. 6.3. The switching signals for the six switches in the inverter are produced based on the Hall sensor output of DRM using dSPACE 1103 system as shown in Fig. 6.2. Every switch in the inverter remains on for 120 electrical degrees as shown in Fig. 6.4. The control strategy is such that at a particular time only two switches are in ON state. Thus, at a time, V_{DC} is applied across two phases of motor. These states with their respective motor phases are presented in Table 6.1.

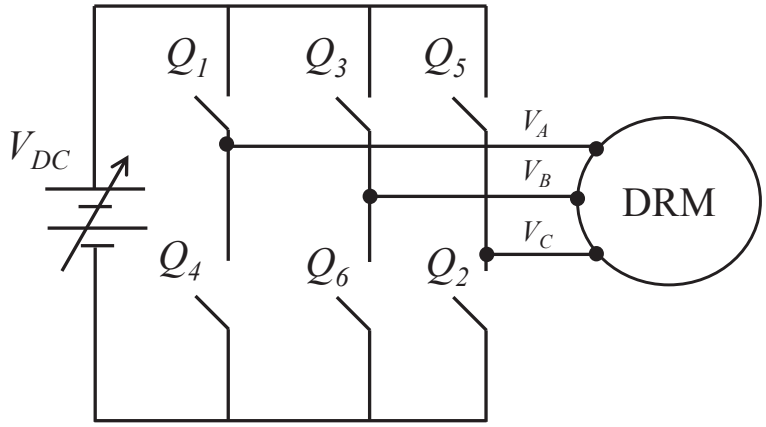

Figure 6.3: Experimental setup for DRM testing.

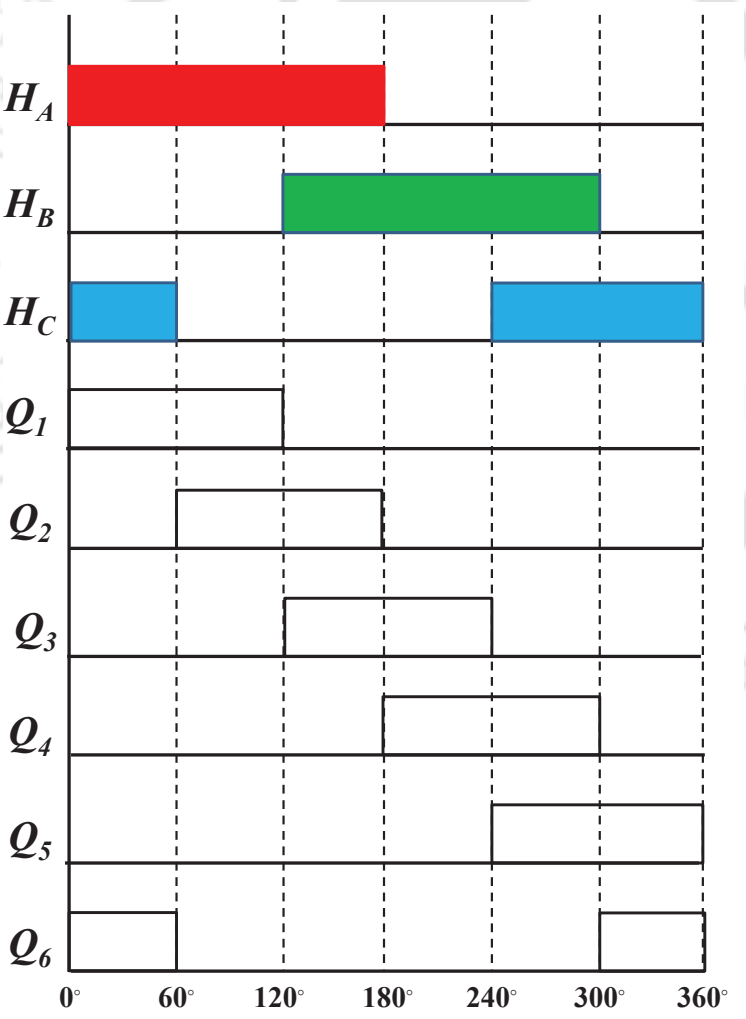

Figure 6.4: Experimental setup for DRM testing.

Table 6.1: Switching states of inverter switches based on Hall sensor outputs.

Hall sensors (H_A, H_B, H_C)	Phases	ON switches
101	$A-B$	Q_1, Q_6
100	$A-C$	Q_1, Q_2
110	$B-C$	Q_3, Q_2
010	$B-A$	Q_3, Q_4
011	$C-A$	Q_5, Q_4
001	$C-B$	Q_5, Q_6

6.2.2 Sine Pulse Width Modulation (SPWM) technique

It is discussed in the previous section that the rotating magnetic field in the inner air-gap is produced by outer rotor. Since outer rotor behaves similar to rotor of PM rotor, it can be operated as synchronous motor. Thus, DRM is also tested as a synchronous motor i.e. it has been given voltage excitation through an inverter using SPWM technique. With this technique, the motor is given very low frequency and is increased slowly once the rotor starts rotating. Fig. 6.5 shows a block diagram for DRM using SPWM technique.

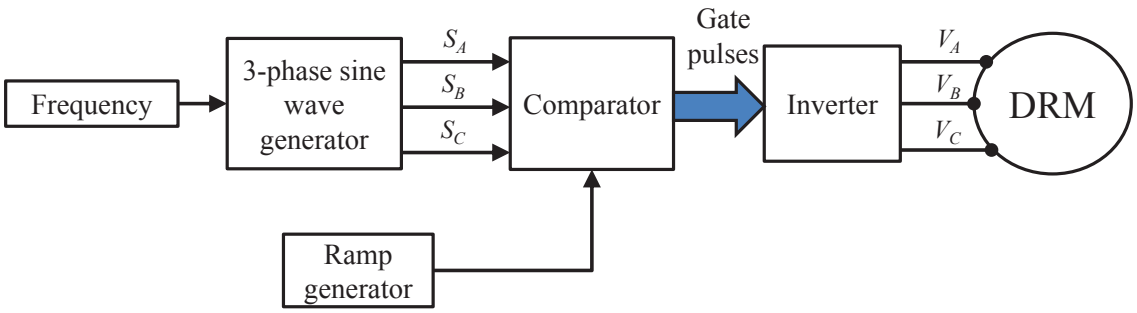

Figure 6.5: Block diagram for sine PWM technique.

6.3 Testing of DRM

In order to understand various possible operating modes of DRM, various tests have been performed. Following subsections present different tests performed on DRM. In order to test DRM, the present test system was modified. Thus, in the absence of dedicated test rig and involvement of gear arrangement, the motor was tested only upto 25 Hz. As the test frequency was low, iron losses in the

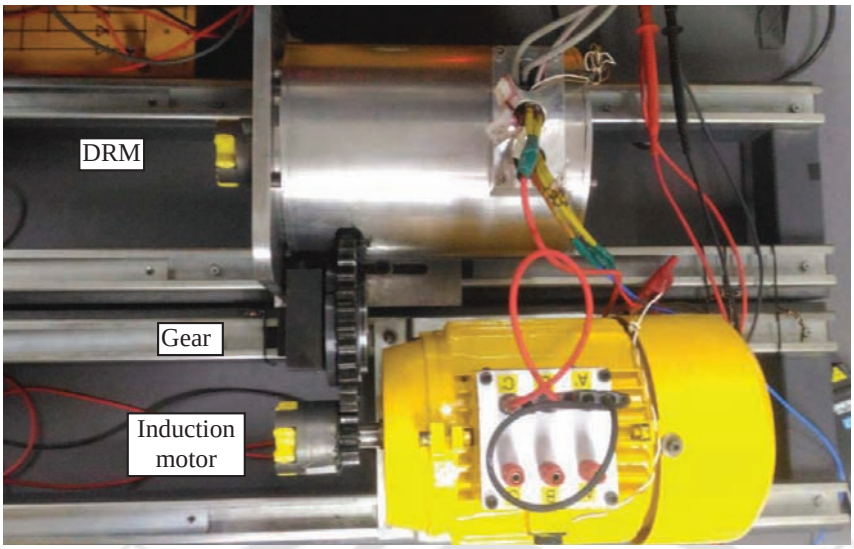

Figure 6.6: Figure showing outer rotor coupled to an IM for open circuit tests.

motor were neglected during the tests.

6.3.1 Open circuit tests

This test is named as open circuit test, as the stator terminals of DRM are kept open during the tests. The outer rotor of DRM is run with an induction motor and its back emf (BEMF) and Hall sensor outputs are recorded. Fig. 6.6 shows the setup for open circuit tests. The IM is excited with sine PWM technique with different fundamental frequency. IM runs the outer rotor of DRM, as the outer rotor has magnets, it produced BEMF in the stator terminals. Also Hall sensor outputs can also be seen during this test. Fig. 6.7 presents the outputs of the Hall sensors. Ideally, output of Hall sensors should have duty ratio of 50% and should be displaced 120° from each other. However, it can be observed that duty ratio of Hall sensors are 53%, 55% and 63% for phases *A*, *B* and *C* respectively. This can be due to the reason that the Hall sensor placed in the motor are unipolar Hall sensors and detects magnetic field due to south pole. And thus, at the edges of the poles due to insufficient flux density, its unable to detect the magnetic pole. Also it can be observed that outputs of Hall sensors are not exactly 120° apart. This can be due to improper physical placement of Hall sensors in the motor.

As the outer rotor is rotated with IM, it produced rotating magnetic field in the inner air-gap and thus the inner rotor rotates due to induction effect. BEMF at the terminals of DRM is affected by the speed of inner rotor. Therefore, BEMF waveforms for DRM during open circuit tests with inner rotor freely moving and blocked inner rotor are presented in Fig. 6.8 and 6.9 respectively. It can be

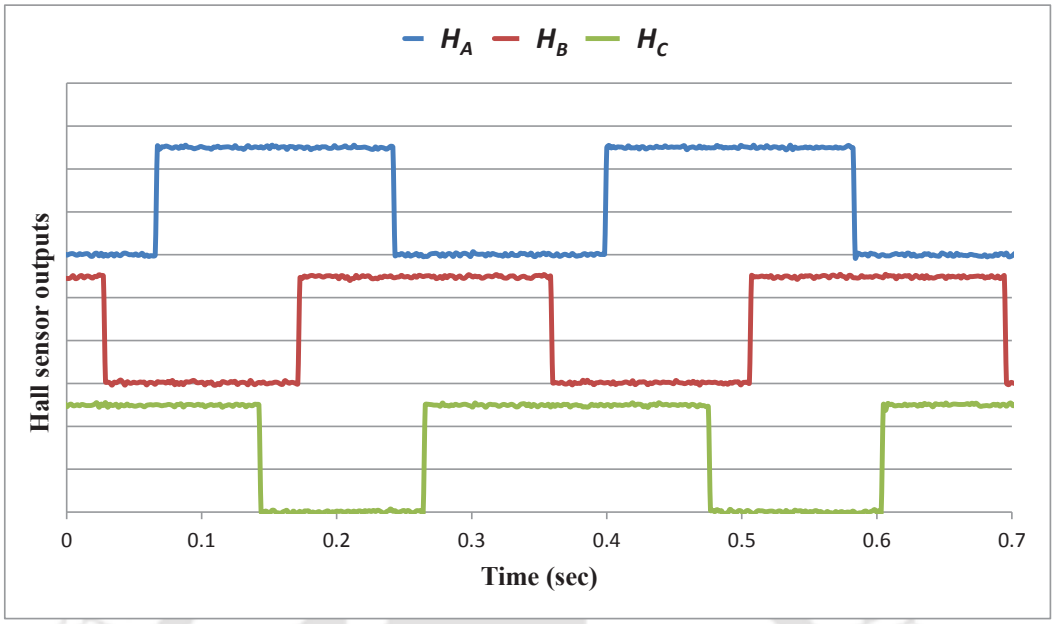

Figure 6.7: Output of Hall sensors.

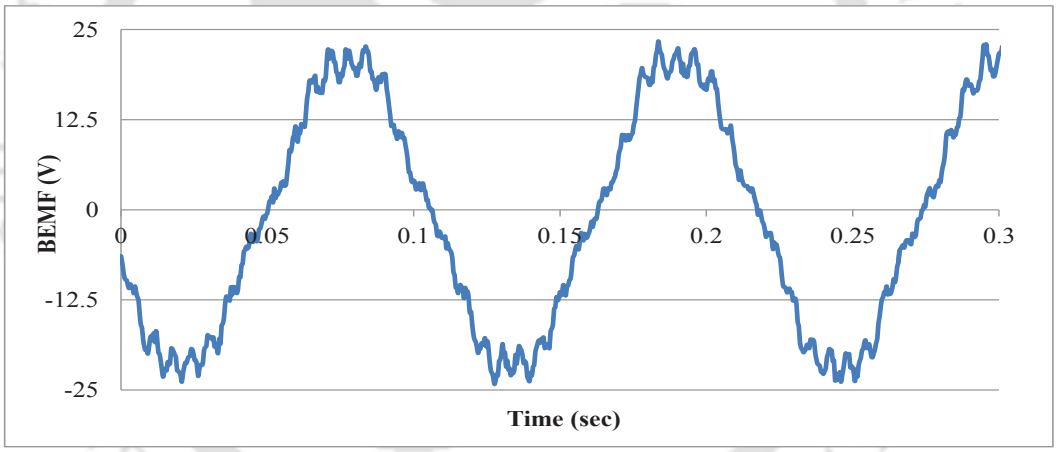

Figure 6.8: BEMF waveform at 9 Hz with cage rotor freely moving.

observed that the shape of the waveform is different gets distorted in Fig. 6.9 due to the opposition field created by blocked inner rotor.

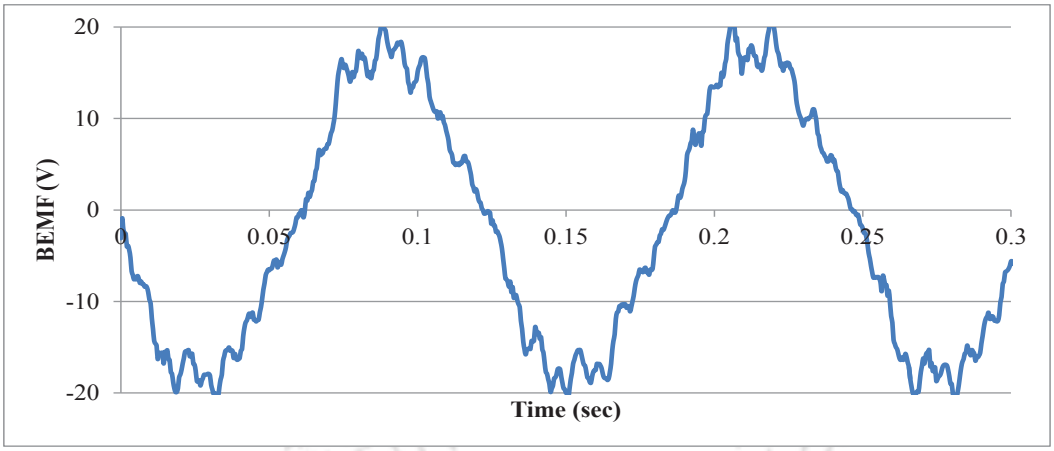

Figure 6.9: BEMF waveform at 8 Hz with cage rotor blocked.

Tables 6.2 and 6.3 present result for open circuit tests for the two cases of inner rotor freely moving and blocked inner rotor respectively. Where N_{OR} and N_{IR} are the speeds of outer rotor and inner rotor respectively and $BEMF$ is the rms value of the phase voltage measured at the terminal of the motor. $Freq$ is the fundamental frequency of electrical excitation given to IM. It can be observed that as the excitation frequency increases, the BEMF also increases. The increase in BEMF is almost linear in nature and can be observed from the ratio of BEMF and N_{OR} in Tables 6.2 and 6.3, which is almost constant.

Table 6.2: Results with inner rotor freely moving.

$Freq$ (Hz)	N_{OR} (rpm)	N_{IR} (rpm)	$BEMF$ (V)	$BEMF/N_{OR}$
1	14.55	14.00	2.30	0.16
3	44.47	44.00	5.40	0.12
5	74.11	73.40	8.80	0.12
7	104.02	102.70	12.00	0.12
9	134.20	134.00	15.70	0.12

Table 6.3: Results with inner rotor blocked.

$Freq$ (Hz)	N_{OR} (rpm)	N_{IR} (rpm)	$BEMF$ (V)	$BEMF/N_{OR}$
1	14.02	0.00	2.40	0.17
3	44.20	0.00	5.50	0.12
5	74.11	0.00	9.00	0.12
7	104.55	0.00	11.60	0.11
9	135.00	0.00	16.00	0.12

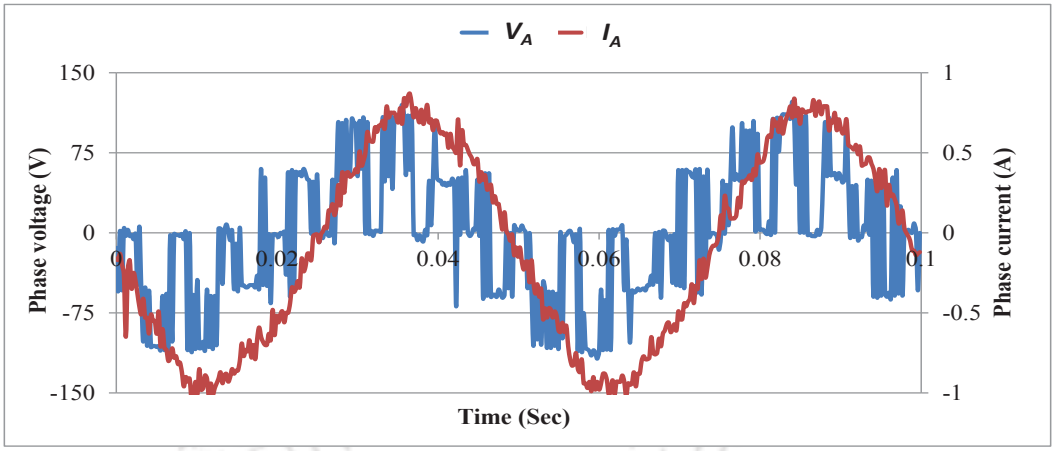

Figure 6.11: Phase current and phase voltage waveforms during load testing of inner rotor.

6.3.2 Inner rotor loading tests

During this test the DRM is given excitation from inverter controlled with SPWM technique and is operated at different frequencies. The inner rotor is loaded with the help of coupled DC generator while the outer rotor is left to rotate. Fig. 6.10 shows the experimental setup for this test. The inner rotor is coupled to a DC generator whereas, the outer rotor coupling gear has been removed and it is kept free. Fig. 6.11 shows the waveform for phase voltage and phase current of DRM during this test at 20 Hz. It can be observed that the phase voltage is a stepped waveform as the SPWM technique has been used for the test.

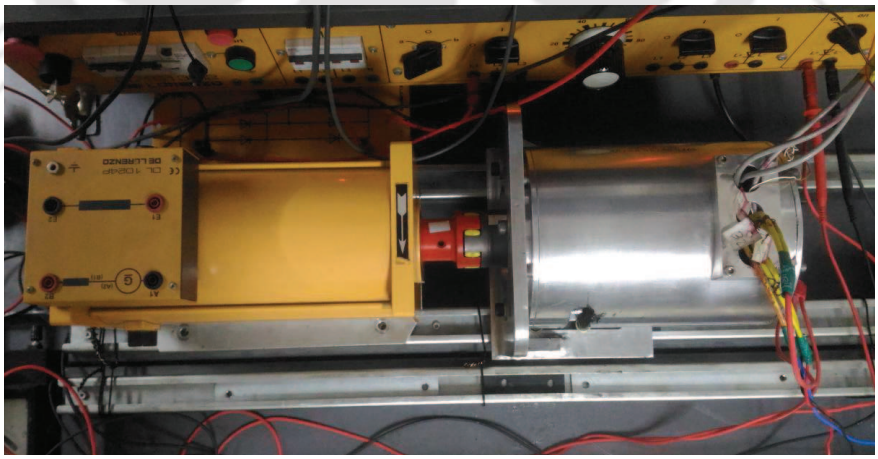

Figure 6.10: Experimental setup for inner rotor loading tests on DRM.

During the test DRM is operated with constant excitation voltage with particular frequency and loading is increased on inner rotor in steps. Tables 6.4 and 6.5 present results for inner rotor loading

with DRM operating at 20 and 25 Hz respectively. V_A and I_A represent the phase voltage and phase current for DRM during the test. It can be observed from the results that with higher operating frequency, higher torque is achieved. This is due to the reason that, at higher speed, even for the same operating slip, the stator voltage is higher and thus it is able to deliver more torque for the same slip. The operating slips (s_{IR}) for inner rotor are shown in Tables 6.4 and 6.5.

Table 6.4: Test results for inner rotor loading test at 20 Hz.

V_A (V)	I_A (A)	N_{IR} (rpm)	N_{OR} (rpm)	$Torque_{IR}$ (Nm)	s_{IR}	P_{in}	P_{IR}	Eff(%)
60.14	0.60	297.60	300.00	0.00	0.01	86.60	0.00	0.00
60.20	0.70	287.00	300.00	0.91	0.04	101.14	27.51	27.20
59.58	0.90	274.70	300.00	1.94	0.08	128.69	56.04	43.55
59.40	1.10	263.60	300.00	2.61	0.12	156.82	72.15	46.00
58.50	1.30	254.00	300.00	3.03	0.15	182.52	80.82	44.28

Table 6.5: Test results for inner rotor loading test at 25 Hz.

V_A (V)	I_A (A)	N_{IR} (rpm)	N_{OR} (rpm)	$Torque_{IR}$ (Nm)	s_{IR}	P_{in}	P_{IR}	Eff(%)
75.20	0.72	372.20	375.00	0.00	0.01	129.40	0.00	0.00
74.47	0.81	364.00	375.00	0.79	0.03	144.77	30.20	20.86
73.90	0.90	356.00	375.00	1.41	0.05	159.62	52.56	32.93
73.00	1.10	344.00	375.00	2.37	0.08	192.72	85.34	44.28
73.27	1.30	331.00	375.00	3.17	0.12	228.60	109.87	48.06
73.50	1.50	313.00	375.00	3.85	0.17	264.60	126.29	47.73

Tables 6.4 and 6.5, also presents the input power (P_{in}) and output power of inner rotor (P_{IR}) and efficiency (Eff) in (%). As the P_{in} was not measured at the time of experiment, an approximation is presented with an assumed power factor of 0.8 from the Fig. 6.11. It can be observed that as the output power increases the efficiency of the motor increases. Since, the motor was operated upto half the rated speed (750 rmp), maximum efficiency of around 48% was achieved.

6.3.3 Outer rotor loading tests

During loading test of outer rotor, the outer rotor is coupled to a DC generator through a gear assembly as shown in Fig. 6.12. The inner rotor is made free to rotate. The DRM is run with 120° conduction mode using the Hall sensor outputs. The load test on outer rotor is performed with its speed and hence the stator frequency is maintained constant. As the load is increased on the outer rotor with the excitation voltage of DC generator, its speed slows down. The speed is maintained by increasing the input voltage. Fig. 6.13 shows the input phase voltage and phase current during load test on outer rotor at 10 Hz. It can be observed from the figure that the waveform phase is carrying current for approximately 120° in each direction as in case of 120° commutation technique. The current conduction is not exactly 120° due to commutation time of switches.

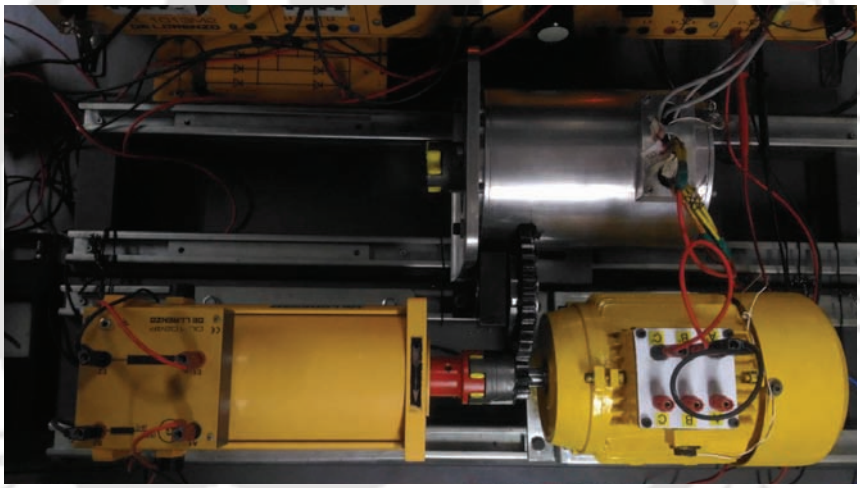

Figure 6.12: Experimental setup for DRM testing.

Tables 6.6 and 6.7 present results for outer rotor loading performed at 10 and 8 Hz respectively.

Table 6.6: Test results for outer rotor loading test at 10 Hz.

V_A (V)	I_A (A)	N_{OR} (rpm)	N_{IR} (rpm)	$Torque_{OR}$ (Nm)	P_{in}	P_{OR}	Eff(%)
29.00	0.76	145.59	145.00	2.33	52.90	35.52	67.16
33.00	0.94	152.47	152.00	2.80	74.37	44.72	60.13
37.00	1.18	150.35	150.00	3.70	104.78	58.19	55.53
42.00	1.50	147.71	146.80	4.96	151.2	76.79	50.79

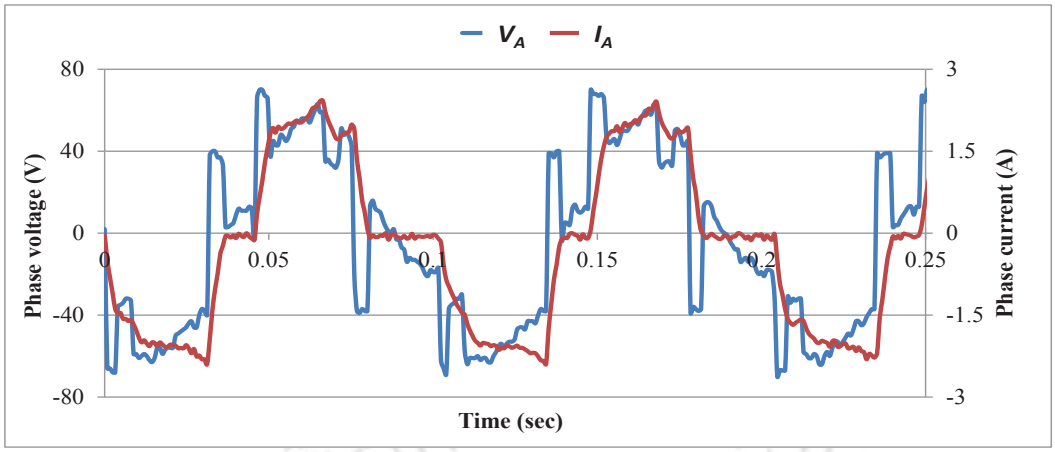

Figure 6.13: Phase current and phase voltage waveforms during load testing of outer rotor.

Table 6.7: Test results for outer rotor loading test at 8 Hz.

V_A (V)	I_A (A)	N_{OR} (rpm)	N_{IR} (rpm)	$Torque_{OR}$ (Nm)	P_{in}	P_{OR}	Eff(%)
24.30	0.70	120.49	119.00	2.11	40.99	26.62	64.94
30.00	1.05	122.56	120.00	3.17	75.60	40.67	53.79
32.47	1.18	120.71	122.10	3.67	91.96	46.47	50.54
35.40	1.39	119.12	119.00	4.47	118.09	55.72	47.18

Tables 6.6 and 6.7, also presents the input power (P_{in}) and output power of outer rotor (P_{OR}) and efficiency (Eff) in (%). As the P_{in} was not measured at the time of experiment, an approximation is presented with an assumed power factor of 0.8 similar to the case of inner rotor loading. It can be observed that as the output power increases the efficiency of the motor decreases.

6.3.4 Both rotors load test

During this test DRM is run with the same control strategy as used for outer rotor testing. The test setup for loading both rotors is show in Fig. 6.14. Both the rotors are loaded with DC generators and the loads are varied by varying the excitation voltages of the generators. Initially the outer rotor is loaded with a fixed load and the inner rotor load is increased in steps. The same loading process is followed for different initial load of outer rotor. Fig. 6.15 shows the waveforms for phase voltage and phase current during the test. It can be observed that the waveforms are similar to the waveforms during outer rotor loading test. This is due to the use of same control strategy in both the tests.

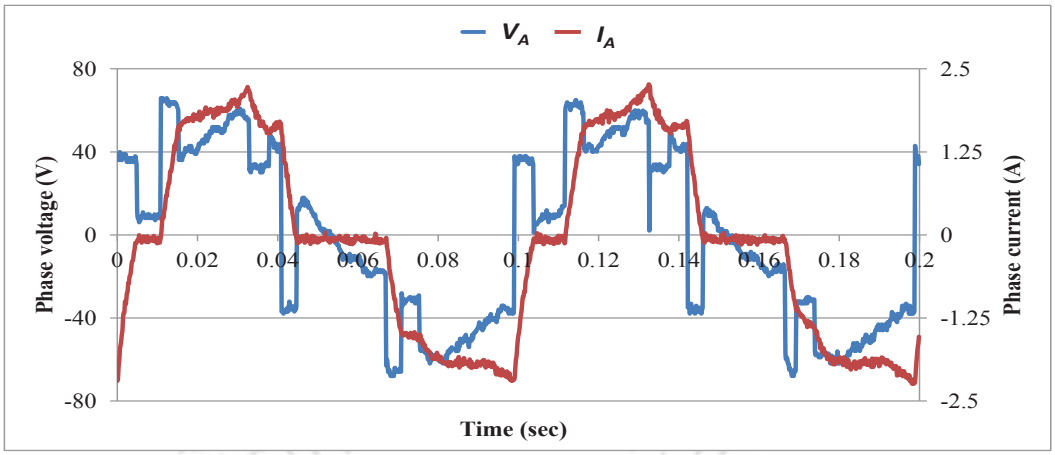

Figure 6.15: Phase current and phase voltage waveform during load testing of both rotors.

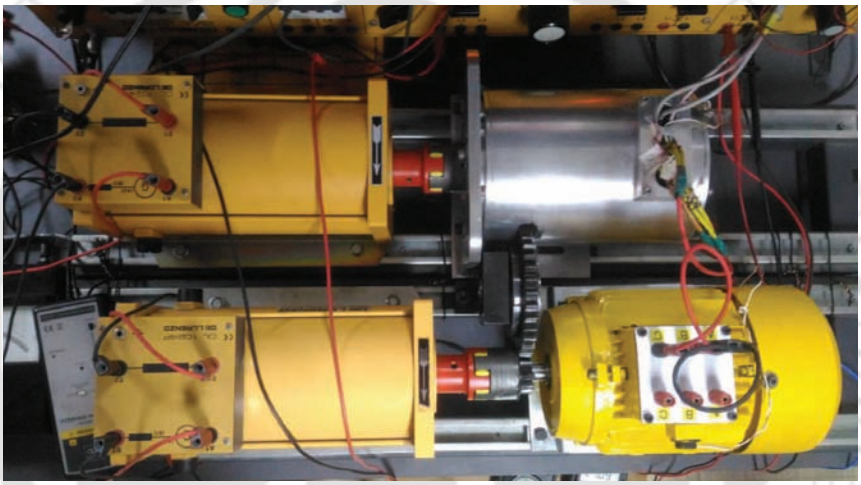

Figure 6.14: Experimental setup for both rotor load testing of DRM.

Table 6.8: Test results for both rotors loading test at 10 Hz.

V_A (V)	I_A (A)	N_{OR} (rpm)	N_{IR} (rpm)	$Torque_{OR}$ (Nm)	$Torque_{IR}$ (Nm)
31.00	0.83	150.09	148.00	2.70	0.00
35.00	1.06	151.94	151.00	3.31	0.00
36.00	1.15	150.88	143.00	3.31	0.60
39.00	1.28	153.00	135.00	3.34	1.28

Table 6.9: Test results for both rotors loading test at 10 Hz.

V_A (V)	I_A (A)	N_{OR} (rpm)	N_{IR} (rpm)	$Torque_{OR}$ (Nm)	$Torque_{IR}$ (Nm)
31.80	0.87	150.88	149.00	2.90	0.00
37.40	1.20	152.47	148.00	3.93	0.00
39.10	1.30	151.68	142.00	3.93	0.61
40.90	1.40	150.88	135.00	3.86	1.27

Table 6.10: Test results for both rotors loading test at 10 Hz.

P_{in}	P_{OR}	P_{IR}	P_{Total}	$Eff(\%)$
61.75	42.44	0.00	42.44	68.72
89.04	52.72	0.00	52.72	59.20
99.36	52.42	9.00	61.42	61.82
199.80	53.60	18.10	71.70	59.85

Table 6.11: Test results for both rotors loading test at 10 Hz.

P_{in}	P_{OR}	P_{IR}	P_{Total}	$Eff(\%)$
66.32	45.82	0.00	45.82	69.08
107.71	62.79	0.00	62.79	58.29
121.99	62.53	9.08	71.60	58.70
137.42	61.00	18.02	79.02	57.50

Tables 6.10 and 6.11 presents the input power (P_{in}) and output power of outer rotor (P_{OR}), inner rotor (P_{IR}), total output power (P_{Total}) and efficiency (Eff) in (%). As the P_{in} was not measured at the time of experiment, an approximation is presented with an assumed power factor of 0.8 similar to the case of inner and outer rotor loading.

6.4 Validation with FEA

FEA model for the DRM is presented in Section 5.2.1.4. In this section, results obtained from FEA are presented in comparison with practical results for validation purpose. Figs. 6.16 and 6.17 present BEMF waveforms obtained during open circuit tests in comparison with those obtained from FEA. It can be observed that the waveforms match in terms of periodicity and magnitude. However,

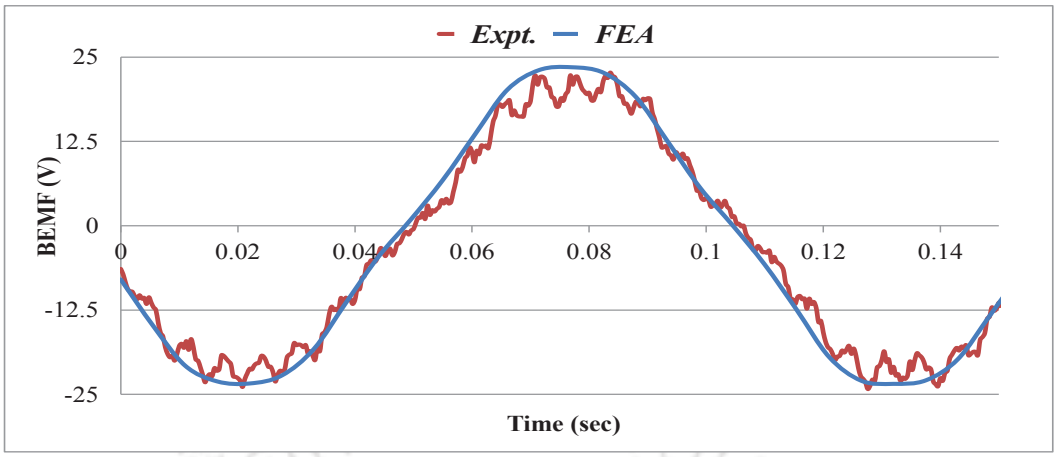

Figure 6.16: Comparison of experimental and FEA BEMF waveforms at 9 Hz with cage rotor freely moving.

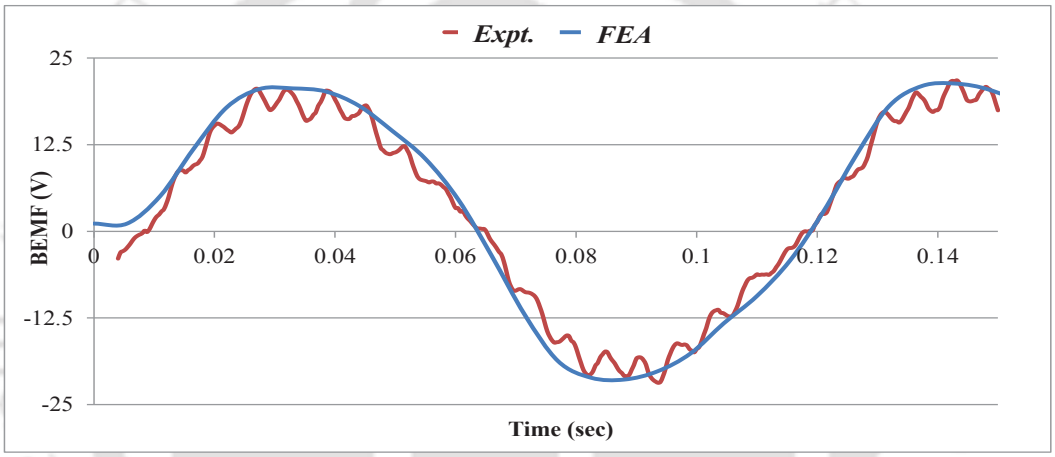

Figure 6.17: Comparison of experimental and FEA BEMF waveforms at 9 Hz with cage rotor blocked.

the practical waveform has many harmonics in it whereas, that from FEA is very smooth. This is due to the reason that, during experiment, the DRM was run with IM through gear assembly. This caused non-uniform speed of DRM thus resulting in non-smooth waveform. Also a deviation from sinusoidal nature can be observed in Fig. 6.17 in both FEA and experimental results. This is due to the effect of magnetic field of inner rotor. As the inner rotor is blocked, it produces huge current in cage rotor and field due to this distorts the field in outer air-gap resulting in deviated BEMF waveform.

Fig.6.18 and 6.19 present comparison of torque obtained from experiment and FEA for inner rotor loading tests at 20 and 25 Hz respectively.

Tables 6.12 and 6.13 present comparison of results for both rotor loading test. Ratio of experimental and FEA torques for both the rotors are presented in 6.14 for comparison of torques. It can be observed from the results that torque values obtained from FEA are very close to those obtained from

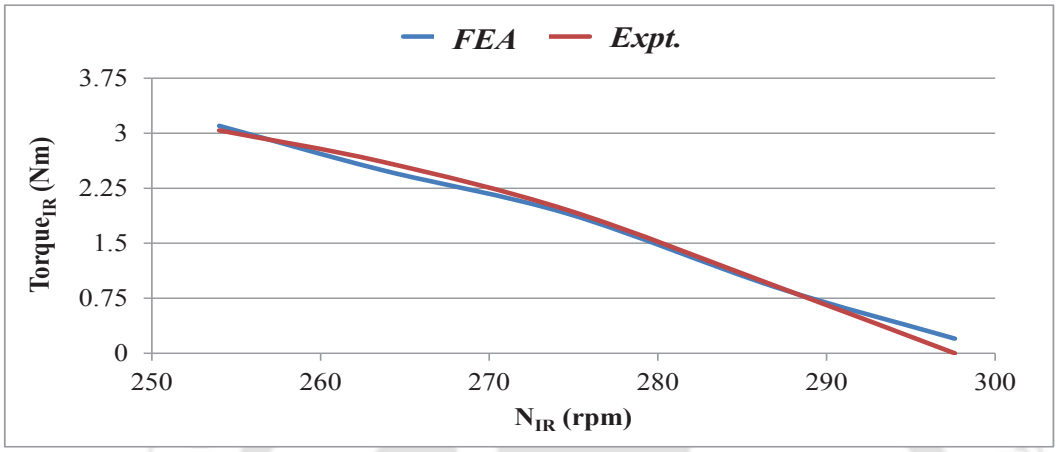

Figure 6.18: Comparison of experimental and FEA torque results during inner rotor loading at 20 Hz.

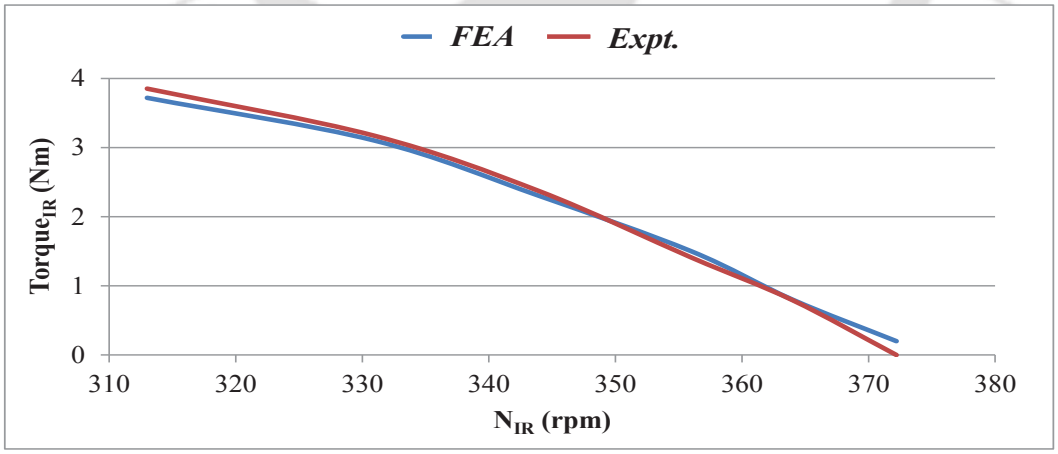

Figure 6.19: Comparison of experimental and FEA torque results during inner rotor loading at 25 Hz.

Table 6.12: Comparison of experimental and FEA torque results during both rotors loading at 10 Hz.

		Experimental		FEA	
N_{OR} (rpm)	N_{IR} (rpm)	$Torque_{OR}$ (Nm)	$Torque_{IR}$ (Nm)	$Torque_{OR}$ (Nm)	$Torque_{IR}$ (Nm)
150.09	148.00	2.70	0.00	2.70	0.14
151.94	149.00	3.31	0.00	3.72	0.00
150.88	143.00	3.31	0.60	3.48	0.50
153.00	135.00	3.34	1.28	3.35	1.00

Table 6.13: Comparison of experimental and FEA torque results during both rotors loading at 10 Hz.

		Experimental		FEA	
N_{OR} (rpm)	N_{IR} (rpm)	$Torque_{OR}$ (Nm)	$Torque_{IR}$ (Nm)	$Torque_{OR}$ (Nm)	$Torque_{IR}$ (Nm)
150.88	149.00	2.90	0.00	2.90	0.00
152.47	148.00	3.93	0.00	4.10	0.00
151.68	142.00	3.93	0.61	3.80	0.50
150.88	135.00	3.86	1.27	3.78	1.09

Table 6.14: Ratios of experimental and FEA results for both rotor loading test.

Ratio Expt./FEA torques for 6.12		Ratio Expt./FEA torques for 6.13	
Outer rotor	Inner rotor	Outer rotor	Inner rotor
1.00	0.00	1	0.00
0.89	0.00	0.96	0.00
0.95	1.20	1.03	1.22
0.99	1.28	1.02	1.16

experiments validating the FEA model.

6.5 Validation with SSM

SSM for DRM was developed in Chapter 4. In this section validation of experimental results with SSM is presented. The parameters for the DRM have been computed in the similar way as presented in Section 4.3.1. Torque equation in 4.32 has three terms named as $T1$, $T2$ and $T3$. Out of these terms $T1$ and $T3$ have terms corresponding to magnet flux and are also sensitive to initial angle of PM

rotor. Whereas, the term $T2$ only has terms corresponding to cage rotor. Thus, for torque calculation from EEC, sum of $T1$ and $T3$ is considered as torque of outer rotor (PM rotor) and $T3$ is considered as torque of inner rotor (cage rotor). Comparison of experimental results and those from SSM for different tests are presented in this section. The parameters for SSM of DRM are given in Table 6.15.

Table 6.15: DRM Parameters for SSM

Symbol	Value	Unit	Symbol	Value	Unit
R_r	4.72	Ω	R_s	10.5	Ω
ϕ_{max_s}	0.36	Wb	ϕ_{max_r}	0.024	Wb
L_{rr}	0.38	H	L_{ss}	0.38	H
P	8		$M_{max\_sr\_ph}$	0.36	H

Fig 6.20 and 6.21 show the comparison of results for inner rotor loading tests. Table 6.16-6.19 present the comparison of experimental and SSM results for outer rotor and both rotor loading tests for different operating conditions.

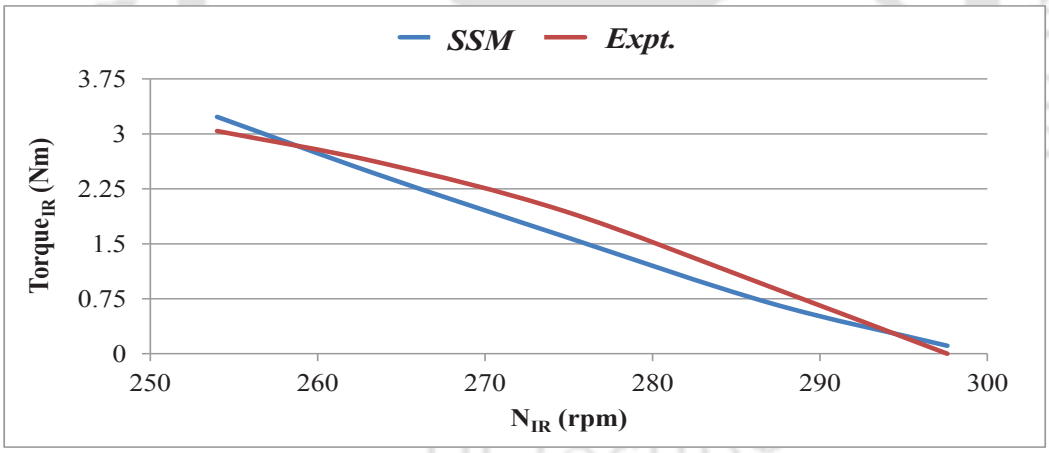

Figure 6.20: Comparison of experimental and SSM torque results during inner rotor loading at 20 Hz.

Table 6.16: Comparison of experimental and SSM torque results during outer rotor loading at 10 Hz.

				Experimental	SSM	Ratio
V_A (V)	I_A (A)	N_{OR} (rpm)	N_{IR} (rpm)	$Torque_{OR}$ (Nm)	$Torque_{OR}$ (Nm)	Expt./SSM
29.00	0.76	145.59	145.00	2.33	2.32	1.00
33.00	0.94	152.47	152.00	2.80	2.87	0.98
37.00	1.18	150.35	150.00	3.70	3.61	1.02
42.00	1.50	147.71	146.80	4.96	4.58	1.08

Table 6.17: Comparison of experimental and SSM torque results during outer rotor loading at 8 Hz.

				Experimental	SSM	Ratio
V_A (V)	I_A (A)	N_{OR} (rpm)	N_{IR} (rpm)	$Torque_{OR}$ (Nm)	$Torque_{OR}$ (Nm)	Expt./SSM
24.30	0.70	120.49	119.00	2.11	2.15	0.98
30.00	1.05	122.56	120.00	3.17	3.20	0.99
32.47	1.18	120.71	122.10	3.68	3.61	1.02
35.40	1.39	119.12	119.00	4.47	4.25	1.05

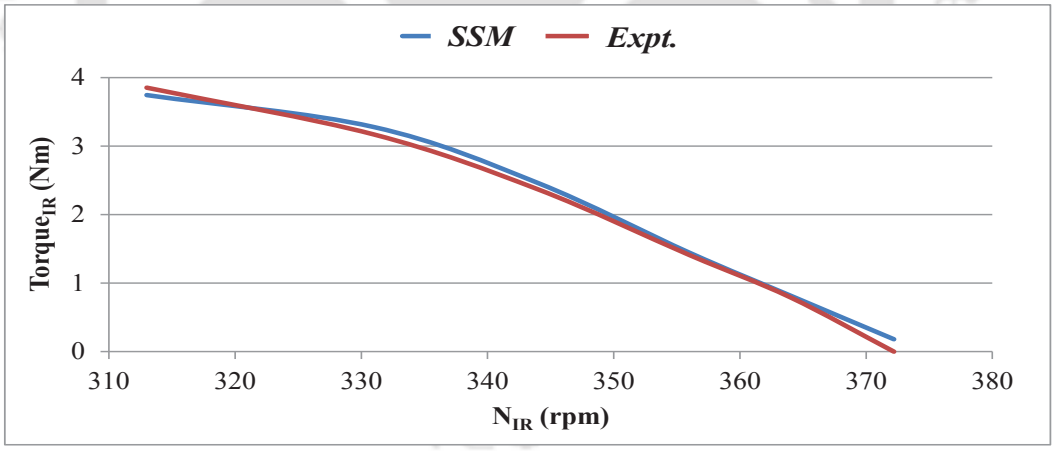

Figure 6.21: Comparison of experimental and SSM torque results during inner rotor loading at 25 Hz.

It can be observed from the presented torque ratios that, results from SSM are very close to the experimental results. Thus, SSM can be used effectively for performance calculation of DRM. In some higher deviation in the results can be observed. This can be due to variation in the equivalent circuit parameters at different operating points in practical, whereas, they are assumed constant in SSM calculations.

Table 6.18: Comparison of experimental and SSM torque results during both rotors loading at 10 Hz.

		Experimental		SSM	
N_{OR} (rpm)	N_{IR} (rpm)	$Torque_{OR}$ (Nm)	$Torque_{IR}$ (Nm)	$Torque_{OR}$ (Nm)	$Torque_{IR}$ (Nm)
150.09	148.00	2.70	0.00	2.54	0.04
151.94	149.00	3.31	0.00	3.24	0.08
150.88	143.00	3.31	0.60	3.38	0.60
153.00	135.00	3.34	1.28	3.35	1.35

Table 6.19: Comparison of experimental and SSM torque results during both rotors loading at 10 Hz.

		Experimental		SSM	
N_{OR} (rpm)	N_{IR} (rpm)	$Torque_{OR}$ (Nm)	$Torque_{IR}$ (Nm)	$Torque_{OR}$ (Nm)	$Torque_{IR}$ (Nm)
150.88	149.00	2.90	0.00	2.66	0.05
152.47	148.00	3.93	0.00	3.67	0.10
151.68	142.00	3.93	0.61	3.84	0.87
150.88	135.00	3.86	1.27	3.66	1.61

Table 6.20: Ratios of experimental and SSM results for both rotor loading test.

Ratio Expt./SSM torques for 6.18		Ratio Expt./SSM torques for 6.19	
Outer rotor	Inner rotor	Outer rotor	Inner rotor
1.06	0.00	1.09	0.00
1.02	0.00	0.97	0.00
0.98	0.99	1.03	0.70
0.99	0.95	1.05	1.79

6.6 Comparison with conventional SPM motor

A comparison of the DRM and conventional SPM motor is presented in this section. The PM motor has been considered with surface mounted full arc magnets. The stator of the PM motor has been kept same as that of DRM. Magnet thickness of the PM motor has been chosen such that the magnets have same volume as that of original DRM. The FEA model of the PM motor is shown in 6.22.

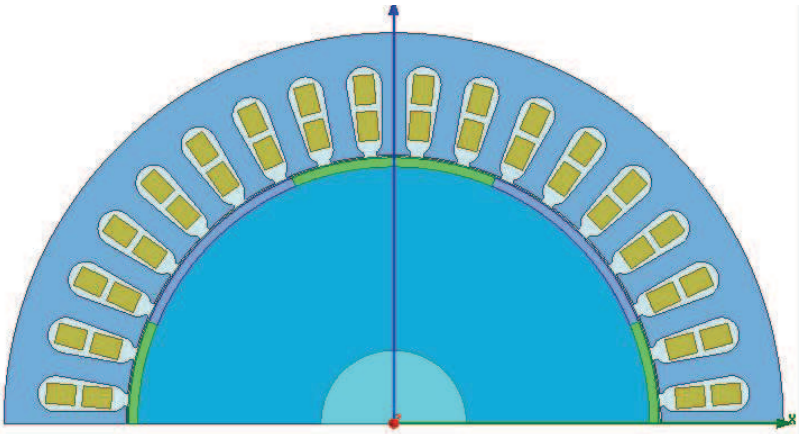

Figure 6.22: FEA model of the PM motor for comparison.

Comparison of the motors have been performed for the both rotor loading condition at 10 Hz. Same current excitation has been used for both the motors and speed of the inner rotor has been taken as 145 rpm for DRM. The resulting torque and power are presented in tables 6.21 and 6.22. It can be observed from the results that the power produced by the DRM is significantly less than the power produced by the PM motor. This is mainly due to the reason that the PM motor has full arc magnets which increases the active surface area of the magnet in comparison of DRM. In order to validate this, a modified DRM model has been made where the outer rotor has been assumed to be same as that of PM motor with full arc magnet. The modified DRM is analyzed for the same operating condition and the results are presented in tables 6.21 and 6.22.

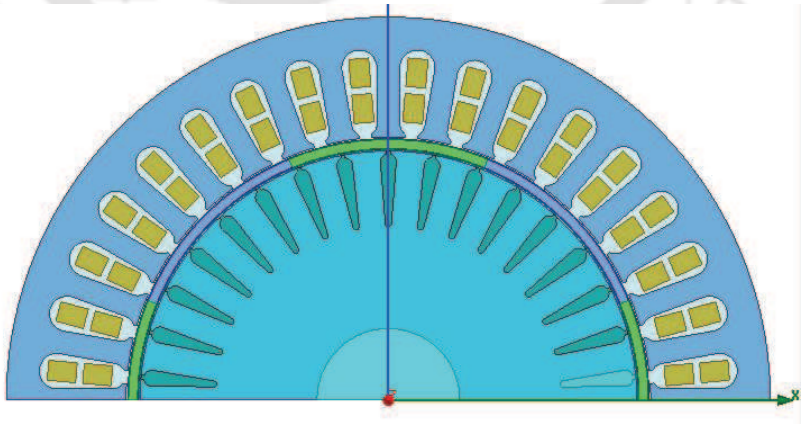

Figure 6.23: FEA model of the modified DRM for comparison.

It can be observed that the total output power with modified DRM is almost same as that of PM

Table 6.21: Torque results for comparison of DRM with PM.

	Actual DRM		Modified DRM	
T_{PM} (Nm)	T_{OR} (Nm)	T_{IR} (Nm)	T_{OR} (Nm)	T_{IR} (Nm)
4.47	3.5	0.03	3.18	1.24

Table 6.22: Power results for comparison of DRM with PM.

	Actual DRM			Modified DRM		
P_{PM} (W)	P_{OR} (W)	P_{IR} (W)	P_T (W)	P_{OR} (W)	P_{IR} (W)	P_T (W)
70.20	54.98	0.45	50.95	49.98	18.76	68.74

motor. Thus in this configuration the power density is same as that of PM motor. As the manufactured DRM is the first prototype, during its design and development, validation of the concept of DRM had been made as the major focus and a design of DRM had been chosen such that it is easy to manufacture and thus performance of the motor was not much focused on. Having validated the concept of the DRM and solved the mechanical complexities, further prototype will consider the issues of optimally utilizing the volume of the motor and other performance parameters.

6.7 Summary and Conclusion

In this chapter testing of DRM in laboratory is discussed. As DRM has two torque producing components, various different tests have been performed to understand the behavior of the motor. It has been observed that both the rotors can be loaded individually as well as simultaneously. The control strategy employed to run the motor is also discussed briefly. Validation of FEA model with experimental results is also presented towards the end of the chapter. A comparison study has also been carried out with surface mounted full arc PM motor. It has been concluded from this study that the present DRM does not has the power density as that of conventional PM motor. However a modified DRM design is presented to highlight the reason for reduced power density and motivation for further development of the DRM. Next chapter presents thesis conclusions and directions for future work for further development of DRM.

7

Conclusion and Future Work

Contents

7.1 Conclusion

Electric motor is the main component of any EV powertrain. Thus, it is desirous to have a motor with high power density and high efficiency to be used for EV powertrain. Various types of motor used for EV application and their limitations have been discussed in this thesis. The thesis has mainly focused on design and development of Dual Rotor Motor. Various possible configurations and different analysis models have been discussed in detail. Finally, a prototype of the finalized configuration and its test results have been presented. The specific contributions made are listed below.

7.2 Summary of Contributions

Keeping in view the requirement of EV for future and the status of electric motors used for EV application, this thesis has proposed a new type of motor named as Dual Rotor Motor. All the works presented in the thesis are towards design, analysis, prototyping and testing of this motor.

- The concept of a motor having two mechanical ports has been discussed. Its various possible configurations are presented and based on the conventional motors used for EV applications, selection of IM and PM based DRM has been described in detail.

- An analytical model is presented to understand the concept of torque production in DRM. The analytical model has been developed using the individual analytical models of IM and PM motor. The presented model not only gives a great insight to the operation of motor, it also provides air-gap magnetic fields in both the air-gaps, which is very important from magnetic viewpoint of any motor.

- An electrical equivalent circuit is also presented for the DRM. The approach that has been used for the development of EEC has been discussed in great detail. Thus, in case the configuration of the motor is changed, using the same approach EEC for motor with any configuration can also be developed. EEC helps in quick performance calculation of DRM.

- A prototype of the DRM has been made and tested in laboratory. The design and manufacturing process of DRM is presented in detail with pictures at every stage of its development. The

difficulties faced during the mechanical design due to the complexity of the motor and devised solutions are also discussed.

7.3 Future work

Based on the work presented in this thesis, the following directions are suggested as possible extensions for further development of DRM technology.

- The performance of DRM can be tested in comparison to and IM or PM motor with the same power and volume to ascertain the actual gain in terms of torque or power density as well as from cost and operation viewpoints.
- During the development of analytical model presented for DRM, many assumptions such as radial geometry of cage rotor slots, ring type permanent magnets, infinite permeability of stator and rotor core, have been made. The analytical model can be improved by including the actual geometry of motor parts and actual property of the material into the model.
- Various parameters for EEC developed for DRM are found using FEA method. However, for practical purpose, it is preferred that the parameters for equivalent circuit for any type of motor is found with some basic tests on motor. Thus, some tests needs to be devised such that all the parameters in the EEC of DRM can be determined with practical results.
- Presently the output of the two rotors of DRM have been measured individually. However, for some practical application where only one output is required, these two outputs have to be combined. This can be done using the planetary gear arrangement which has three moving parts and out of three parts two can be input and one can be output. Fig. 7.1 shows a schematic representation of planetary gear arrangement with two of its moving part connected to two rotors of DRM [52]. A practical prototype of such system can be made in future and the combined output of DRM can be compared with the output of conventional motors of the same size.

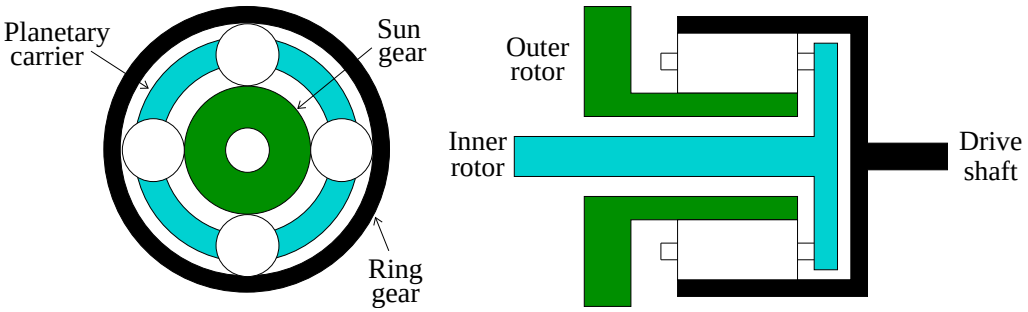

(a) H (b) H

Figure 7.1: Schematic of planetary set gear arrangement (a) Front view (b) Cut section view

- Present experimentation of DRM has been performed with 120° commutation technique observing that outer rotor is the main driving rotor and hence control of PMCLDC must be employed. However, it is worth exploring that how the presence of cage rotor affect the performance of this control strategy and what modifications are required to make it more suitable for DRM application.

- In the present configuration of DRM rectangular magnets have been used in the outer rotor. The magnet shape should be optimized such that a larger surface area is achieved with minimum flux leakage and space for required mechanical support.

8

Development of Boundary Conditions and Final Equations

Integrals frequently encountered in this section can be denoted as [43]:

$$f_1(n,h,q) = \int_{\theta_q}^{\theta_q+\eta} \cos(n\theta)\cos\left(\frac{h\pi}{\eta}\left(\theta-\theta_q\right)\right)d\theta \tag{8.1}$$

$$f_2(n,h,q) = \int_{\theta_q}^{\theta_q+\eta} \sin(n\theta)\cos\left(\frac{h\pi}{\eta}\left(\theta-\theta_q\right)\right)d\theta \tag{8.2}$$

$$f_3(n,q) = \int_{\theta_q}^{\theta_q+\eta} \cos\left(n\theta_q\right)d\theta \tag{8.3}$$

$$f_4(n,q) = \int_{\theta_q}^{\theta_q+\eta} \sin\left(n\theta_q\right)d\theta \tag{8.4}$$

for $h\pi = n\eta$

$$f_1 = \frac{\eta}{2}\left(\cos\left(n\theta_q\right) + \frac{1}{2h\pi}\left(\sin\left(n\left(\theta_q+2\eta\right)\right) - \sin\left(n\theta_q\right)\right)\right) \tag{8.5}$$

$$f_2 = \frac{\eta}{2}\left(\sin\left(n\theta_q\right) - \frac{1}{2h\pi}\left(\cos\left(n\left(\theta_q+2\eta\right)\right) - \cos\left(n\theta_q\right)\right)\right) \tag{8.6}$$

for $h\pi \neq n\eta$

$$f_1 = \frac{-n\eta^2\left((-1)^h\sin\left(n\left(\eta+\theta_q\right)\right) - \sin\left(n\theta_q\right)\right)}{h^2\pi^2 - n^2\eta^2} \tag{8.7}$$

$$f_2 = \frac{n\eta^2\left((-1)^h\cos\left(n\left(\eta+\theta_q\right)\right) - \cos\left(n\theta_q\right)\right)}{h^2\pi^2 - n^2\eta^2} \tag{8.8}$$

$$f_3 = \frac{1}{n}\left(\sin\left(n\left(\eta+\theta_q\right)\right) - \sin\left(n\theta_q\right)\right) \quad \forall \quad h \tag{8.9}$$

$$f_4 = \frac{1}{n}\left(-\cos\left(n\left(\eta+\theta_q\right)\right) + \cos\left(n\theta_q\right)\right) \quad \forall \quad h \tag{8.10}$$

Equations (8.11) and (8.12) are derived by equating the coefficients of $\cos(n\theta)$ and $\sin(n\theta)$ respectively of both sides of (3.48) [43].

$$\frac{n}{R_r}\left(A_n^{ia}R_r^n - B_n^{ia}R_r^{-n}\right) - K1\times f_3 - K2\times f_1 = 0 \tag{8.11}$$

$$\frac{n}{R_r}\left(C_n^{ia}R_r^n - D_n^{ia}R_r^{-n}\right) - K1\times f_4 - K2\times f_2 = 0 \tag{8.12}$$

where,

$$K1 = \frac{1}{\pi}\sum_{q=1}^{Q} C_0^q \frac{-\alpha J_1(\alpha R_r) + G_1 \alpha Y_1(\alpha R_r)}{J_0(\alpha R_r) - G_1 Y_0(\alpha R_r)}$$

$$K2 = \frac{1}{\pi}\sum_{q=1}^{Q}\sum_{h=1}^{\infty} C_h^q \frac{J'_{h\pi/\eta}(\alpha R_r) - G_h Y'_{h\pi/\eta}(\alpha R_r)}{J_{h\pi/\eta}(\alpha R_r) - G_h Y_{h\pi/\eta}(\alpha R_r)}$$

Equations (8.13) and (8.14) are written using (3.49), where at $r = R_r$, this continuity equation becomes Fourier series expansion of $A_{ia}(r,\theta)$ over an interval of $\left[\theta_q, \theta_q + \eta\right]$.

$$C_0^q = \frac{1}{\eta}\int_{\theta_q}^{\theta_q+\eta} A_{ia}(R_r,\theta)\, d\theta \tag{8.13}$$

$$C_h^q = \frac{2}{\eta}\int_{\theta_q}^{\theta_q+\eta} A_{ia}(R_r,\theta)\cos\left(\frac{h\pi}{\eta}\left(\theta-\theta_q\right)\right) d\theta \tag{8.14}$$

Further development of (8.13) and (8.14) leads to (8.15) and (8.16) respectively.

$$C_0^q - A_0^{ia} - K3 \times f_3 - K4 \times f_4 = 0 \tag{8.15}$$

$$C_h^q - 2 \cdot K3 \times f_1 - 2 \cdot K4 \times f_2 = 0 \tag{8.16}$$

where,

$$K3 = \sum_{n=1}^{\infty}\left(A_n^{ia} R_r^n + B_n^{ia} R_r^{-n}\right)$$

$$K4 = \sum_{n=1}^{\infty}\left(C_n^{ia} R_r^n + D_n^{ia} R_r^{-n}\right)$$

Equations (8.17) and (8.18) are derived by equating the coefficients of $\cos(n\theta)$ and $\sin(n\theta)$ respectively of both sides of (3.50).

$$\frac{n}{R_a}\left(A_n^{ia} R_a^n - B_n^{ia} R_a^{-n}\right) - \frac{1}{\mu_m}\frac{n}{R_a}\left(A_n^m R_a^n - B_n^m R_a^{-n}\right)$$

$$= \frac{1}{\mu_m}\gamma'_n R_a\left(\cos(n\delta) + j\sin(n\delta)\right) \tag{8.17}$$

$$\frac{n}{R_a}\left(C_n^{ia} R_a^n - D_n^{ia} R_a^{-n}\right) - \frac{1}{\mu_m}\frac{n}{R_a}\left(C_n^m R_a^n - D_n^m R_a^{-n}\right)$$

$$= \frac{1}{\mu_m}\gamma'_n R_a\left(\sin(n\delta) - j\cos(n\delta)\right) \tag{8.18}$$

Equations (8.19) and (8.20) are derived by equating the coefficients of $\cos(n\theta)$ and $\sin(n\theta)$ respectively of both sides of (3.51).

$$A_n^{ia} R_a^n + B_n^{ia} R_a^{-n} - A_n^m R_a^n - B_n^m R_a^{-n}$$

$$= \gamma_n R_a (\cos(n\delta) + j \sin(n\delta)) \tag{8.19}$$

$$C_n^{ia} R_a^n + D_n^{ia} R_a^{-n} - C_n^m R_a^n - D_n^m R_a^{-n}$$

$$= \gamma_n R_a (\sin(n\delta) - j \cos(n\delta)) \tag{8.20}$$

Equations (8.21) and (8.22) are derived by equating the coefficients of $\cos(n\theta)$ and $\sin(n\theta)$ respectively of both sides of (3.52).

$$\frac{n}{R_m} (A_n^{oa} R_m^n - B_n^{oa} R_m^{-n}) - \frac{1}{\mu_m} \frac{n}{R_m} (A_n^m R_m^n - B_n^m R_m^{-n})$$

$$= \frac{1}{\mu_m} \gamma'_n R_m (\cos(n\delta) + j \sin(n\delta)) \tag{8.21}$$

$$\frac{n}{R_m} (C_n^{oa} R_m^n - D_n^{oa} R_m^{-n}) - \frac{1}{\mu_m} \frac{n}{R_m} (C_n^m R_m^n - D_n^m R_m^{-n})$$

$$= \frac{1}{\mu_m} \gamma'_n R_m (\sin(n\delta) - j \cos(n\delta)) \tag{8.22}$$

Equations (8.23) and (8.24) are derived by equating the coefficients of $\cos(n\theta)$ and $\sin(n\theta)$ respectively of both sides of (3.53).

$$A_n^{oa} R_m^n + B_n^{oa} R_m^{-n} - A_n^m R_m^n - B_n^m R_m^{-n}$$

$$= \gamma_n R_m (\cos(n\delta) + j \sin(n\delta)) \tag{8.23}$$

$$C_n^{oa} R_m^n + D_n^{oa} R_m^{-n} - C_n^m R_m^n - D_n^m R_m^{-n}$$

$$= \gamma_n R_m (\sin(n\delta) - j \cos(n\delta)) \tag{8.24}$$

By expanding (3.54), we get equation (8.25) and (8.26).

$$\frac{n}{R_s} (A_n^{oa} R_s^n - B_n^{oa} R_s^{-n}) = \begin{cases} \mu_0 J_\nu & \text{if} \quad n = \nu \cdot p \\ 0 & \text{if} \quad n \neq \nu \cdot p \end{cases} \tag{8.25}$$

$$\frac{n}{R_s}\left(C_n^{oa}R_s^n - D_n^{oa}R_s^{-n}\right) = \begin{cases} -j\mu_0 J_\nu & \text{if} \quad n = \nu \cdot p \\ 0 & \text{if} \quad n \neq \nu \cdot p \end{cases} \tag{8.26}$$

Solving equation (3.55) with (3.48) and (3.50) results in the following equation:

$$\sum_{q=1}^{Q} C_0^q = 0 \tag{8.27}$$

The resultant equations (8.11-8.27) are written in a matrix form (8.28) to find the unknown constants. Table 8.1 describes the equations corresponding to particular rows of (8.28).

$$[A]_{(12N+Q(H+1)+1)\times(12N+Q(H+1)+1)} \times [X]_{(12N+Q(H+1)+1)\times 1} = [B]_{(12N+Q(H+1)+1)\times 1} \tag{8.28}$$

Table 8.1: Equations corresponding to the rows of (8.28)

	$[A]$	$[X]$	$[B]$
Row1	LHS(8.11)	C_0^q	RHS(8.11)
Row2	LHS(8.12)	C_h^q	RHS(8.12)
Row3	LHS(8.15)	A_0^{ia}	RHS(8.15)
Row4	LHS(8.16)	A_n^{ia}	RHS(8.16)
Row5	LHS(8.17)	B_n^{ia}	RHS(8.17)
Row6	LHS(8.18)	C_n^{ia}	RHS(8.18)
Row7	LHS(8.19)	D_n^{ia}	RHS(8.19)
Row8	LHS(8.20)	A_n^m	RHS(8.20)
Row9	LHS(8.21)	B_n^m	RHS(8.21)
Row10	LHS(8.22)	C_n^m	RHS(8.22)
Row11	LHS(8.23)	D_n^m	RHS(8.23)
Row12	LHS(8.24)	A_n^{oa}	RHS(8.24)
Row13	LHS(8.25)	B_n^{oa}	RHS(8.25)
Row14	LHS(8.26)	C_n^{oa}	RHS(8.26)
Row15	LHS(8.27)	D_n^{oa}	RHS(8.27)

9

Additional details for steady state model of DRM

Illustration for path of integration in calculating the field energy in *Step T3* of torque calculation.

For a magnetic system having three windings, stored magnetic energy calculation is illustrated here. The general expression for stored magnetic energy is given by (9.1).

$$W_{fld} = \int_0^{\lambda_f} id\lambda \tag{9.1}$$

As lossless magnetic energy storage system is a conservative system, the value of W_{fld} is uniquely determined by the final values of flux linkages which are its state variables $(\lambda_{af}, \lambda_{bf}, \lambda_{cf})$. Magnetic system being a conservative system, W_{fld} in (9.1) is the same regardless of how the state variables $(\lambda_a, \lambda_b, \lambda_c)$ are brought to their final values [53].

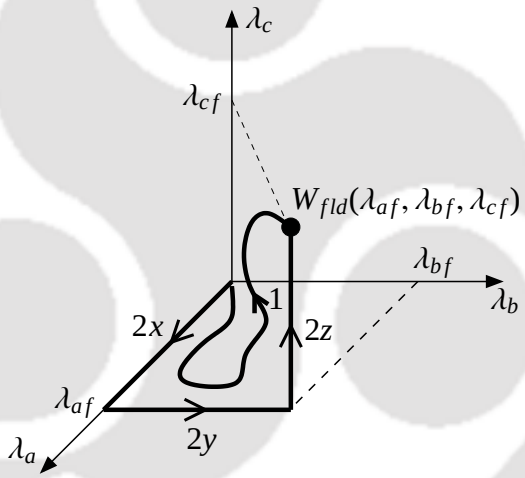

Figure 9.1: Integration path to obtain W_{fld}.

Considering Fig. 9.1, in which two separate paths are shown over which (9.1) can be integrated to find W_{fld} at point $(\lambda_{af}, \lambda_{bf}, \lambda_{cf})$. Path 1 is difficult to integrate unless all the currents are known explicitly as function of flux linkages. However, as the integration in (9.1) is path independent, path 2 gives the same result and is much easier to integrate. Thus, choosing the path 2 for integrating, (9.1) can be presented as (9.2) and can be further evaluated as given in (9.3).

$$W_{fld} = \int_{\text{path } 2x} id\lambda + \int_{\text{path } 2y} id\lambda + \int_{\text{path } 2z} id\lambda \tag{9.2}$$

$$W_{fld} = \left[\int_0^{\lambda_{af}} i_a d\lambda_a\right]_{x_1} + \left[\int_0^{\lambda_{bf}} i_b d\lambda_b\right]_{x_2} + \left[\int_0^{\lambda_{cf}} i_c d\lambda_c\right]_{x_3} \tag{9.3}$$

where,

$$x_1 \equiv (\lambda_c = \lambda_b = 0)$$

$$x_2 \equiv (\lambda_c = 0, \lambda_a = \lambda_{af})$$

$$x_3 \equiv (\lambda_a = \lambda_{af}, \lambda_b = \lambda_{bf})$$

In a similar manner, stored magnetic field energy can also be obtained for systems having more than three windings.

Determination of $\phi_{\max\_r}$ by finding equivalent number of turns for cage rotor. Flux linked by two adjacent bars is found in the same way as that for stator using the concept of flux per pole and is given by (9.4).

$$\phi_{bar} = B_{av} \cdot \frac{2\pi R_{IR}}{P} \cdot L \tag{9.4}$$

In order to find $\phi_{\max\_r}$, ϕ_{bar} needs to be referred to stator side. Thus, the cage rotor needs to be transformed to and equivalent 3-phase winding to find turns ratio. The procedure adopted for transformation of cage rotor to equivalent 3-phase winding is described below.

Each bar of the cage rotor is considered as phase having (1/2) turn [54]. Thus, a cage rotor having N_b bars will have N_b phases of half turn each.

These N_b phase system is transformed to 2 phase system in the similar way as 3 phase is transformed to 2 phase. In the transformation, the current magnitude is kept same hence the number of turns in the transformed windings will change to keep the mmf constant [55]. Fig. 9.2 shows schematic representation the transformation.

Assuming sinusoidal distribution of current in all the bars, the current in n^{th} bar can be represented as:

$$i_n = i_{bm} \sin\left(\omega_{cg} t - \left(\frac{n-1}{N_b}\right) 2\pi\right) \tag{9.5}$$

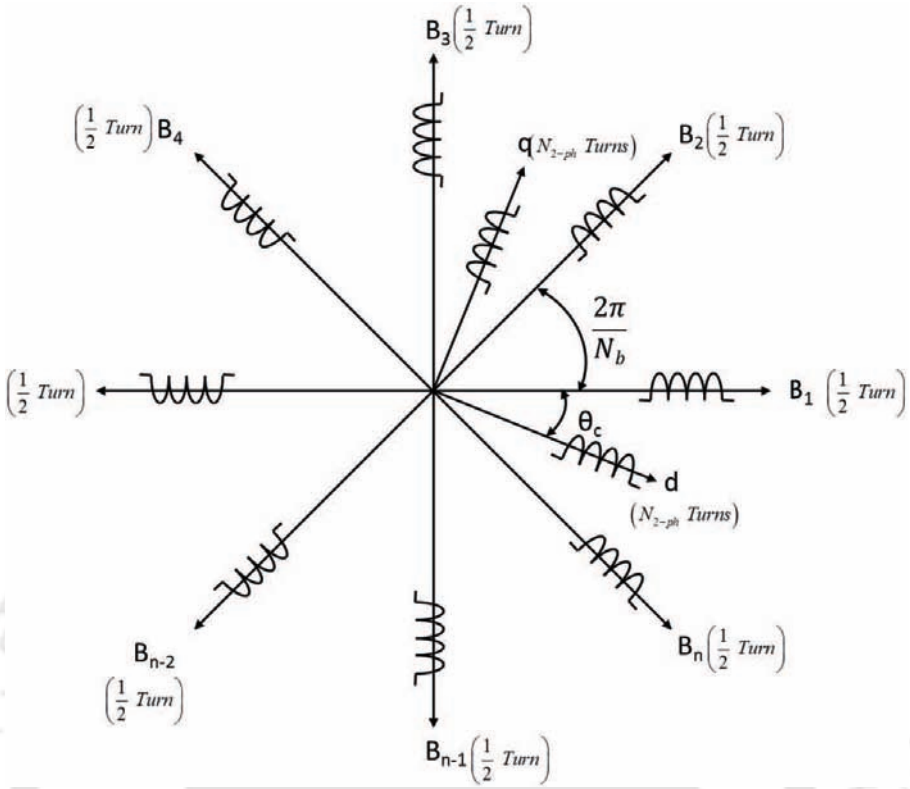

Figure 9.2: Transformation of cage rotor to equivalent 2 phase system.

From Fig. 9.2, equating the components of all the bar mmf to the mmf along *d* axis:

$$T_{2-ph} i_d = \sum_{n=1}^{N_b} \frac{1}{2} i_n \cos\left(\theta_c + \frac{(n-1)\,2\pi}{N_b}\right) \tag{9.6}$$

Considering $i_d = i_{bm} sin(\omega_{cg} t)$ and bar currents from (9.5), (9.6) is simplified to:

$$N_{2-ph} i_{bm} \sin\left(\omega_{cg} t\right) = N_b \frac{1}{2} i_{bm} \sin\left(\omega_{cg} t\right) \tag{9.7}$$

which upon further simplification results into:

$$N_{2-ph} = \frac{N_b}{2} \tag{9.8}$$

Similar result can be obtained by considering *q* axis current. Thus, from (9.8), it is concluded that, if a cage rotor having N_b bars are transformed into a 2-phase winding, each winding will have $\frac{N_b}{2}$ turns carrying the same current as that of one bar. The relation between the number of turns of 3-phase and

2-phase system for constant mmf and same phase current is [55]:

$$N_{3-phase} = \frac{2}{3} N_{2-phase} \tag{9.9}$$

Thus, considering, (9.8) and (9.10), for cage rotor, the equivalent number of turns for three phase system is given by:

$$N_{3-phase} = \frac{N_b}{3} \tag{9.10}$$

Thus, the turns ratio between stator and equivalent 3-phase winding of rotor is:

$$T_{ratio} = \frac{N_{ph}}{3 - phase} = \frac{3N_{ph}}{N_b} \tag{9.11}$$

Therefore, $\phi_{\max\_r}$ is obtained by multiplying ϕ_{bar} with T_{ratio} and the final equation is given by:

$$\phi_{\max\_r} = B_{av} \cdot \frac{2\pi R_{IR}}{P} \cdot L \cdot \frac{3N_{ph}}{N_b} \tag{9.12}$$

Bibliography

[1] A. Rahideh and T. Korakianitis, "Analytical magnetic field distribution of slotless brushless pm motors. part 2: Open-circuit field and torque calculations," *IET Elec. Pow. Appl.*, vol. 6, no. 9, pp. 639–651, November 2012.

[2] C. C. Chan, "The rise and fall of electric vehicles in 1828-1930: Lessons learned [scanning our past]," *Proceedings of the IEEE*, vol. 101, no. 1, pp. 206–212, Jan 2013.

[3] E. H. Wakefield, "History of the electric automobile," *Society of Automotive Engineers*, pp. 2–3, 1994.

[4] C. Sulzberger, "An early road warrior: electric vehicles in the early years of the automobile," *IEEE Power and Energy Magazine*, vol. 2, no. 3, pp. 66–71, May 2004.

[5] C. C. Chan, "The state of the art of electric, hybrid, and fuel cell vehicles," *Proceedings of the IEEE*, vol. 95, no. 4, pp. 704–718, April 2007.

[6] L. Situ, "Electric vehicle development: The past, present and future," in *Power Electronics Systems and Applications, 2009. PESA 2009. 3rd International Conference on*, May 2009, pp. 1–3.

[7] I. Boldea, L. Tutelea, L. Parsa, and D. Dorrell, "Automotive electric propulsion systems with reduced or no permanent magnets: An overview," *IEEE Trans. Ind. Appl.*, vol. 61, no. 10, pp. 5696–5711, Oct 2014.

[8] J.-R. Riba, C. Lpez-Torres, L. Romeral, and A. Garcia, "Rare-earth-free propulsion motors for electric vehicles: A technology review," *Renewable and Sustainable Energy Reviews*, vol. 57, pp. 367 – 379, 2016.

[9] A. Nagasaka, M. Nada, H. Hamada, S. Hiramatsu, Y. Kikuchi, and H. Kato, "Development of the hybrid/battery ecu for the toyota hybrid system," in *SAE Technical Paper*. SAE International, 02 1998.

[10] X. D. Xue, K. W. E. Cheng, and N. C. Cheung, "Selection of electric motor drives for electric vehicles," in *Power Engineering Conference, 2008. AUPEC '08. Australasian Universities*, Dec 2008, pp. 1–6.

[11] G. Dancygier and J. C. Dolhagaray, "Motor control law and comfort law in the peugeot and citroen electric vehicles driven by a dc commutator motor," in *Power Electronics and Variable Speed Drives, 1998. Seventh International Conference on (Conf. Publ. No. 456)*, Sep 1998, pp. 370–374.

[12] J. F. Gieras and M. Wing, *Permanent Magnet Motor Technology Revised*, 2nd ed., B. Raton, Ed. CRC, Jan 2015.

[13] N. A. Demerdash and T. W. Nehl, "Dynamic modeling of brushless dc motors for aerospace actuation," *IEEE Transactions on Aerospace and Electronic Systems*, vol. AES-16, no. 6, pp. 811–821, Nov 1980.

[14] W. Tong, *Mechanical Design of Electric Motors*. CRC Press, 2014.

[15] M. A. Rahman and M. A. Masrur, "Advances on ipm technology for hybrid electric vehicles," in *2009 IEEE Vehicle Power and Propulsion Conference*, Sept 2009, pp. 92–97.

[16] J. D. Widmer, R. Martin, and M. Kimiabeigi, "Electric vehicle traction motors without rare earth magnets," *Sustainable Materials and Technologies*, vol. 3, pp. 7 – 13, 2015. [Online]. Available: http://www.sciencedirect.com/science/article/pii/S2214993715000032

[17] C. Lewis, "The advanced induction motor," in *Power Engineering Society Summer Meeting, 2002 IEEE*, vol. 1, July 2002, pp. 250–253 vol.1.

[18] K. Rahman and M. Ehsani, "Performance analysis of electric motor drives for electric and hybrid electric vehicle applications," in *IEEE Pow. Electron. in Transport.*, 1996, pp. 49–56.

[19] Z. Rahman, M. Ehsani, and K. L. Butler, "An investigation of electric motor drive characteristics for ev and hev propulsion systems," in *SAE Technical Paper*. SAE International, 08 2000. [Online]. Available: http://dx.doi.org/10.4271/2000-01-3062

[20] H. Chen and J. J. Gu, "Implementation of the three-phase switched reluctance machine system for motors and generators," *IEEE/ASME Transactions on Mechatronics*, vol. 15, no. 3, pp. 421–432, June 2010.

[21] J. Malan and M. J. Kamper, "Performance of hybrid electric vehicle using reluctance synchronous machine technology," in *Industry Applications Conference, 2000. Conference Record of the 2000 IEEE*, vol. 3, 2000, pp. 1881–1887 vol.3.

[22] K. M. Rahman, B. Fahimi, G. Suresh, A. V. Rajarathnam, and M. Ehsani, "Advantages of switched reluctance motor applications to ev and hev: design and control issues," *IEEE Transactions on Industry Applications*, vol. 36, no. 1, pp. 111–121, Jan 2000.

[23] J. d. Santiago, H. Bernhoff, B. Ekergrd, S. Eriksson, S. Ferhatovic, R. Waters, and M. Leijon, "Electrical motor drivelines in commercial all-electric vehicles: A review," *IEEE Transactions on Vehicular Technology*, vol. 61, no. 2, pp. 475–484, Feb 2012.

[24] C. Chan and Y. S. Wong, "Electric vehicles charge forward," *IEEE Pow. and Ener. Mag.*, vol. 2, no. 6, pp. 24–33, 2004.

[25] C. Yunyun, Q. Li, Z. Xiaoyong, W. Hua, and Z. Wang, "Electromagnetic performance analysis of double-rotor stator permanent magnet motor for hybrid electric vehicle," *IEEE Trans. on Magn.*, vol. 48, no. 11, pp. 4204–4207, 2012.

[26] J. Larmine and J. Lowry, *Electric Vehicle Technology Explained*. Wiley, 2003.

[27] C. Shu-mei, H. Wen-xiang, and Z. Qian-fan, "Research on power density improvement design of an HEV using induction machine based electrical variable transmission," in *IEEE Veh. Pow. and Prop. Conf.*, 2008, pp. 1–4.

[28] Y. Cheng, S. Cui, L. Song, and C. Chan, "The study of the operation modes and control strategies of an advanced electromechanical converter for automobiles," *IEEE Trans. on Magn.*, vol. 43, no. 1, pp. 430–433, 2007.

[29] L. Xu, Y. Zhang, and X. Wen, "Multioperational modes and control strategies of dual-mechanical-port machine for hybrid electrical vehicles," *IEEE Trans. on Ind. Appl.*, vol. 45, no. 2, pp. 747–755, 2009.

[30] Y. YANG, "Double-rotor switched reluctance machine for integrated electromechanical transmission in hybrid electrical vehicles," Ph.D. dissertation, School of Graduate Studies of McMaster University, Dec. 2013.

[31] P. Pisek, B. Stumberger, T. Marcic, and P. Virtic, "Design analysis and experimental validation of a double rotor synchronous PM machine used for HEV," *IEEE Trans. on Magn.*, vol. 49, no. 1, pp. 152–155, 2013.

[32] Y. H. Yeh, M. F. Hsieh, and D. G. Dorrell, "Different arrangements for dual-rotor dual-output radial-flux motors," *IEEE Trans. on Ind. Appl.*, vol. 48, pp. 611–622, March-April 2012.

[33] M. N. Ansari, A. K. Singh, and P. Kumar, "Performance analysis of a hybrid dual rotor motor for electric vehicle application," *XXth International Conference on Electrical Machines, Marseille*, pp. 2002–2007, 2012.

[34] M. Yilmaz and P. Krein, "Capabilities of finite element analysis and magnetic equivalent circuits for electrical machine analysis and design," in *IEEE Pow. Electr. Spec. Conf.*, June 2008, pp. 4027–4033.

[35] K. Sawa, H. Yamamoto, and K. Miyachi, "Analysis of armature circuit inductance of dc machines by fem," *IEE Proce. Electr. Pow. Appln.*, vol. 132, no. 6, pp. 307–314, Nov. 1985.

[36] Z. Zhu and D. Howe, "Winding inductances of brushless machines with surface-mounted magnets," in *IEEE Inter. Conf. Elec. Mach. and Driv.*, May 1997, pp. WB2/2.1–WB2/2.3.

[37] T. M. Jahns, "Torque production in permanent-magnet synchronous motor drives with rectangular current excitation," *IEEE Trans. Ind. Appl.*, vol. IA-20, no. 4, pp. 803–813, July 1984.

[38] T. J. E. Miller and R. Rabinovici, "Back-emf waveforms and core losses in brushless dc motors," *Proce. Inst. Elect. Eng.*, vol. 141, no. 3, pp. 144–154, May 1994.

[39] E. Levi, M. Jones, S. Vukosavic, and H. Toliyat, "Steady-state modeling of series-connected five-phase and six-phase two-motor drives," *IEEE Trans. on Ind. Appl.*, vol. 44, no. 5, pp. 1559–1568, 2008.

[40] S. Alyaqout, P. Papalambros, and A. Ulsoy, "Combined robust design and robust control of an electric dc motor," *IEEE/ASME Trans. on Mechatron.*, vol. 16, no. 3, pp. 574–582, 2011.

[41] R. H. Staunton, C. W. Ayers, L. D. Marlino, J. N. Chiasson, and T. A. Burress, "Evaluation of 2004 toyota prius hybrid electric drive system," U.S. Dept. Energy, Special Rep., Tech. Rep., May 2006.

[42] E. Devillers, J. L. Besnerais, T. Lubin, M. Hecquet, and J. P. Lecointe, "A review of subdomain modeling techniques in electrical machines: Performances and applications," in *2016 XXII International Conference on Electrical Machines (ICEM)*, Sept 2016, pp. 86–92.

[43] T. Lubin, S. Mezani, and A. Rezzoug, "Analytic calculation of eddy currents in the slots of electrical machines: Application to cage rotor induction motors," *IEEE Tran. on Magn.*, vol. 47, no. 11, pp. 4650–4659, Nov 2011.

[44] D. C. Hanselmann, *Brushless Permanent Magnet Motor Design*. New York: McGraw Hill, 2004.

[45] F. Dubas and C. Espanet, "Analytical solution of the magnetic field in permanent-magnet motors taking into account slotting effect: No-load vector potential and flux density calculation," *IEEE Trans. Magn.*, vol. 45, no. 5, pp. 2097–2109, May 2009.

[46] S. J. Farlow, *Partial Differential Equations for Scientists and Engineers*. New York: Dover, 1993.

[47] T. Lubin, S. Mezani, and A. Rezzoug, "Analytical computation of the magnetic field distribution in a magnetic gear," *IEEE Transactions on Magnetics*, vol. 46, no. 7, pp. 2611–2621, July 2010.

[48] H. H. Woodson and J. R. Melcher, "Electromechanical dynamics: MIT opencourseware," Massachusetts Institute of Technology, Tech. Rep.

[49] M. J. Melfi, "Optimum pole configuration of ac induction motors used on adjustable frequency power supplies," in *Industry Applications Society 42nd Annual Petroleum and Chemical Industry Conference*, Sep 1995, pp. 237–242.

[50] R. Krishnan, *Permanent Magnet Synchronous and Brushless DC Motor Drives*. CRC Press, 2010.

[51] I. Boldea and S. A. Nasar, *The Induction Machine Handbook*. CRC Press, 2002.

[52] L. Guzzella and A. Sciarretta, *Vehicle Propulsion Systems: Introduction to Modeling and Optimization*. Springer, 2007.

[53] A. E. Fitzgerald, C. Kingsley Jr., and S. Umans, *Electric Machinery*, 6th ed. Tata McGraw - Hill Education, 2003.

[54] M. G. Say, *The Performance and Design of Alternating Current Machines*, 3rd ed. CBS Publishers and Distributors, 2002.

[55] R. Krishnan, *Electric Motor Drives : Modeling, Analysis and Control*. PHI Learning Private Limited, 2010.

List of Publications

Journal Publications

1. **Ankit Dalal**, S. Nekkalapu and Praveen Kumar, "2-D Analytical Subdomain Model for Hybrid Dual-Rotor Motor" *IEEE Transactions on Magnetics*, vol.52, no.6, pp.1-9, June 2016.

2. **Ankit Dalal** and Praveen Kumar, "Analytical Model for Permanent Magnet Motor with Slotting Effect, Armature Reaction and Ferromagnetic Material Property" *IEEE Transactions on Magnetics*, vol.51, no.12, pp.1-10, Dec. 2015.

3. **Ankit Dalal**, Mohammed Nasir Ansari, and Praveen Kumar, "A Novel Steady State Model of a Hybrid Dual Rotor Motor Comprising Electrical Equivalent Circuit and Performance Equations". *IEEE Transactions on Magnetics*, vol.50, no.12, pp.1-11, Dec. 2014.

4. Ezhil Reena Joy T.P., **Ankit Dalal** and Praveen Kumar, "The Accurate Computation of Mutual Inductance of Two Air Core Square Coils with Lateral and Angular Misalignments in a Flat Planar Surface," *IEEE Transactions on Magnetics*, vol. 50, no. 1, pp. 1-9, Jan. 2014.

5. Rakesh Roy, **Ankit Dalal**, Praveen Kumar, "Prediction of high frequency core loss for electrical steel using the data provided by manufacturer", *Journal of Magnetism and Magnetic Materials*, Vol. 410, 15 July 2016, Pp 248-256.

Conference Publications

1. M. N. Ansari, **Ankit Dalal**, P. Kumar, M. Kikuchi, K. Yamaguchi and H. Iwanaga, "Analytical method for accurate determination of nonlinear magnetization curve of induction motor," *2015 Annual IEEE India Conference (INDICON)*, New Delhi, 17th -20th December 2015.

2. Arindam Das, Anirban Konwar, **Ankit Dalal** and Praveen Kumar, "Investigation of PMSM Motor Performance with Different Magnet Configurations and Rotor Surface Profiling", *ITEC-India 2015*, Chennai, India, 27th -29th August, 2015.

3. **Ankit Dalal**, T.P. Ezhil Reena Joy and Praveen Kumar, ”Mutual Inductance Computation Method for Coils of Different Geometries and Misalignments”, *PES General Meeting Conference and Exposition, 2014 IEEE*, Denver, USA, 26th-30th July, 2015.

4. Prashanth S A, Sameer Nekkalapu, **Ankit Dalal**, Praveen Kumar, ”Analytical Determination of Slot Harmonics content of Air-Gap Magnetic Field for an Induction Machine”, *PES General Meeting Conference and Exposition, 2014 IEEE*, Denver, USA, 26th-30th July, 2015.

5. **Ankit Dalal** and Praveen Kumar, ”Analytical Model of a Permanent Magnet Brushless DC Motor with non-linear ferromagnetic material”, *ICEM 2014*, Berlin, Germany, 2nd-5th Sept. 2014.

6. Praveen Kumar, **Ankit Dalal** and Amit Kumar Singh, ”Identification of Three Phase Induction Machines Equivalent Circuits Parameters Using Multi-Objective Genetic Algorithms”, *ICEM 2014*, Berlin, Germany, 2nd-5th Sept. 2014.

7. Amit Kumar Singh, **Ankit Dalal**, Rokesh Roy and Praveen Kumar, ”Improved Dynamic Model of Induction Motor Including the Effects of Saturation.” *IEEE PEDES*, IIT Bombay, Mumbai, India, 16th - 19th Dec. 2014.

8. Rakesh Roy, Anannya Gogoi, Suparna Kar, **Ankit Dalal**, and Praveen Kumar, ”Steady State Model of Dual Rotor Motor for Electric Vehicle Application.” *IEEE PEDES*, IIT Bombay, Mumbai, India, 16th - 19th Dec. 2014.

9. Sameer Nekkalapu, Prashanth S. A., **Ankit Dalal**, and Praveen Kumar, ”Design and Optimization of Dual Rotor Motor for Electric Vehicle Applicaiton.” *IEEE PEDES*, IIT Bombay, Mumbai, India, 16th - 19th Dec. 2014.

10. Amit Kumar Singh, **Ankit Dalal** and Praveen Kumar, ”Analysis of Induction Motor for Electric Vehicle Application Based on Drive Cycle Analysis.” *IEEE PEDES*, IIT Bombay, Mumbai, India, 16th - 19th Dec. 2014.

11. Mohammed Nasir Ansari, **Ankit Dalal**, and Praveen Kumar, ”A Generalized Methof for Developing Steady State Models for Different Electric Motors.” *IEEE PEDES*, IIT Bombay, Mumbai, India, 16th - 19th Dec. 2014.

12. **Ankit Dalal**, Mohammed Nasir Ansari, Praveen Kumar, ”Analytical Model of Induction Motor for Performance Calculation,” *IEEE COMPUMAG Int. conf.*, Budapest, Hungary, 30 June - 4 July, 2013.

13. **Ankit Dalal**, Amit Kumar Singh, Praveen Kumar, ”Effect of saturation on equivalent circuit analysis of induction motor in practical scenario”, *Xth IEEE INDICON 2013*, I.I.T. Bombay, Mumbai, Dec 2013.

14. Mohammed Nasir Ansari, **Ankit Dalal**, Praveen Kumar, ”Analysis of stray loss and its determination with equivalent circuit for double cage rotor induction motor”, *Xth IEEE INDICON 2013*, I.I.T. Bombay, Mumbai, Dec 2013.